Biomedical Solid State NMR: An ADRF Cross Polarization Study of Calcium Phosphates and Bone Mineral

by

Chandrasekhar Ramanathan

B. Tech., Electrical Engineering
Indian Institute of Technology, Bombay (1988)

M.S., Biomedical Engineering and Mathematics
University of North Carolina at Chapel Hill (1990)

SUBMITTED TO THE HARVARD-MIT DIVISION OF HEALTH SCIENCES AND TECHNOLOGY
AND THE DEPARTMENT OF NUCLEAR ENGINEERING
IN PARTIAL FULFILLMENT OF THE REQUIREMENTS FOR THE DEGREE OF

Doctor of Science
in
Radiological Sciences

at the
Massachusetts Institute of Technology
May 1996

Signature of Author . .....
Harvard-MIT Division of Health Sciences and Technology, and
Department of Nuclear Engineering, May 1996

Certified by ....
Professor Jerome L. Ackerman
Thesis Supervisor

Approved by .....
Professor David Cory
Reader

....
Professor Sidney Yip
Reader

Accepted by ....
Professor Jeffrey P. Friedberg
Chairman, Departmental Committee on Graduate Students

Biomedical Solid State NMR: An ADRF Cross Polarization Study of Calcium Phosphates and Bone Mineral

by

Chandrasekhar Ramanathan

Submitted to the Harvard-MIT Division of Health Sciences and Technology and the Department of Nuclear Engineering on May 14, 1996 in Partial Fulfillment of the Requirements for the Degree of Doctor of Science in Radiological Sciences

Abstract

This thesis investigates the application of a low power solid state NMR technique, using proton to phosphorus-31 cross polarization via adiabatic demagnetization in the rotating frame (ADRF-CP), to study samples of synthetic calcium phosphate and bone mineral.

The first section describes the use of ADRF-CP, with a surface coil, to detect monohydrogen phosphate ions in the presence of a large background of non-protonated phosphate ions in porcine bone and a mixture of synthetic calcium phosphates. Transient oscillations were observed in the transfer of polarization between the proton dipolar and phosphorus Zeeman nuclear spin reservoirs after the initiation of thermal contact. Suppression of the non-protonated phosphate was achieved by detecting the signal when the oscillation was passing through zero, and adjusting the phosphorus rf field to achieve optimal cross polarization with the proton local fields of the monohydrogen phosphate ions. An adiabatic remagnetization of the phosphorus eliminated the oscillations, while increasing the strength of the observed total phosphorus signal.

The second section describes the investigation of three variants of the ADRF process as well as a Jeener-Broekaert pulse sequence to create proton dipolar order in the calcium phosphates. The relative efficiencies of the different techniques were sample dependent, with the ADRF techniques performing well in hydroxyapatite and poorly in brushite. The reason for this poor performance in brushite is not well understood.

The third section describes experiments demonstrating an ADRF-CP variant of the differential cross polarization technique. The inversion of the phosphorus Zeeman temperature is performed by changing the phase of the phosphorus rf by 180 degrees during the cross polarization. Transient oscillations were observed on inverting the phosphorus temperature.

The final section of the thesis describes the design and construction of a two-port double resonance probe with interchangeable coils for a 4.7 T magnet. The plug-in design for the coils facilitates the use of coils of different circuits and geometries with the same set of variable tuning and matching capacitors. Two double resonance coils were constructed, a surface coil using a novel circuit design, and a previously described cylindrical resonator.

Thesis Supervisor: Jerome L. Ackerman
Associate Professor of Radiology
Harvard Medical School

Acknowledgments

There have been so many people who have taught me so much and enriched my life over the last six years here at MIT that I don't really know where to begin. None of this work would have been possible without the support and guidance of Jerry Ackerman. He has been both a friend and a mentor over the last two years. Working with him has helped me rediscover my fascination with science.

Eric McFarland, Jacqueline Yanch, David Cory and Sidney Yip have provided invaluable advice through the years. Bettina Pfleiderer and Yaotang Wu helped me get my research up and running in the lab. The researchers and staff at the MGH-NMR center have created a friendly and truly stimulating research environment in which I have enjoyed working. The staff in the Nuclear Engineering Department and HST have definitely made my life easier with all their help.

Dick Eckaus and Henry Jacobi gave me a job when I needed it badly, helping me continue my studies. A special thank you to Bruce Rosen whose counselling prevented me from dropping out when things were at their worst. Lauren Johnston, Paul Whitworth, Jane Song, Lindsay Haugland, Peter Madden, Rene Smith and Helen Turner have taught me the true meaning of friendship. Thank you for the memories. My parents first set me on this path to discovery and gave me the focus to reach my goals. My brother Kumar has stood by me through everything. My debt to him can never be repaid.

What a long, strange trip it been ....

"To follow knowledge like a sinking star,
Beyond the utmost bound of human thought."

—*Ulysses*, Alfred, Lord Tennyson

Like the sharp edge of a razor, the sages say, is the path.
Narrow it is, and difficult to tread.

—*Katha Upanishad*

"Toutes les transformations sont possibles."

—*L'Invention*, Paul Éluard

Contents

List of Figures

List of Tables

Chapter 1

Introduction

Bone mineral research has grown in recent years, spurred by public health concerns over osteoporosis [1, 2, 3]. While the mineral is often considered to be the inert, inorganic component of bone whose sole function is to provide mechanical support, it has long been known that there is continual remodeling of bone throughout life, with resorption of older bone mineral and synthesis of new mineral. This process allows the bone to grow, to play its role as a reservoir of calcium and phosphorus, and to maintain its structural integrity by repair of defects and trauma. Many aspects of this remodeling process are poorly understood, and additional knowledge of bone mineral dynamics will be central to our understanding of fracture healing, the determinants of bone strength, and the treatment of metabolic bone diseases such as osteoporosis [4, 5, 6, 7].

Various physical and chemical techniques have been brought to bear in the study of bone mineral chemistry. These include x-ray diffraction [8, 9, 10, 11], neutron diffraction, back-scattered electron beam imaging [12, 13, 14], wet chemical analyses [15], FT-IR spectroscopy [16, 17, 18, 19, 20] and solid state NMR spectroscopy. The NMR studies are discussed later in this chapter. While each of these techniques has contributed to our current understanding of the chemistry of bone mineral, none of them has been able to provide a detailed, comprehensive description of the process of mineral deposition and resorption. In particular, most of these techniques are destructive, requiring extensive sample preparation that could significantly change

the local micro-environment of the mineral, as well as its surface chemistry.

An understanding of the chemical dynamics of bone mineral may provide insights into bone growth and metabolic bone disease processes, as well as enable the design of superior antiresorptive pharmaceuticals and bone mineral markers for nuclear medicine scans. Among the established methods, only nuclear medicine techniques, by virtue of the chemical selectivity of a radionuclide-bearing ligand that binds to the surface of bone mineral, have potential for yielding chemical information on the mineral *in vivo*. However, this information is strictly limited to the surface of bone crystallites, and in practice is used merely to detect regions of high or low remodelling activity [21].

The goal of this work is to exploit the superior ability of NMR spectroscopy to discriminate subtle chemical differences (as between PO_4^{3-} and HPO_4^{2-} ions) in the *in vivo* study of bone mineral. Conventional solid state NMR techniques are generally incompatible with *in vivo* application due to the high levels of rf power deposition and the use of magic angle sample spinning. NMR diagnostic techniques, both spectroscopy and imaging, have thus generally been limited to liquid state studies of soft tissues. It has so far not been possible to use the chemical sensitivity of the NMR methodology to obtain chemical information *in vivo* from solid tissues such as bone. We require a method which maintains chemical contrast under conditions of low spectral resolution, and minimizes the application of rf power. Cross polarization by means of adiabatic demagnetization in the rotating frame (ADRF-CP) satisfies these requirements. The development of *in vivo* solid-state NMR techniques would allow the study of bone mineral chemistry in live subjects, and thus overcome the problems due to sample preparation, and the questionable validity of extrapolating the results of studies conducted *ex vivo* to the *in vivo* case. The clinical utility of such techniques could possibly extend to monitoring the healing of fractures, the resorption and remodelling of bone cements or implants and the treatment of metabolic bone diseases such as osteoporosis and osteomalacia.

1.1 Introduction to bone tissue

Bone is a composite tissue whose properties closely depend on its structure and composition. The tissue consists of a network of connective tissue fibers interspersed with bone cells lying in an extracellular ground substance that is impregnated with calcium salts to produce rigidity. The orientation of the collagen fibers, which account for about 95% of the organic matter in the tissue, in the extracellular matrix usually determines the spatial arrangement of the mineral crystals deposited in the matrix, and hence the load bearing axes of the the bone. The fibers are randomly arranged in woven bone while showing preferential orientations in lamellar bone. The matrix also contains non-collageneous proteins such as osteonectin and osteocalcin.

1.1.1 Bone cells

The cellular constituents of bone are osteoblasts, osteocytes, lining cells and osteoclasts [22].

Osteoblasts are responsible for the synthesis and secretion of the organic constituents of the bone matrix and, to some extent, their calcification. The osteoblasts are cuboidal or low columnar cells that form a continuous layer on the growing osseous surface, and are usually found with part of their peripheral membrane in contact with the calcification front.

Osteocytes are the least known of the bone cells due to their localization within enclosed lacunae in the calcified matrix. They are formed from osteoblasts that are gradually buried in a calcified matrix, and are thought to undergo three phases. During the formative phase the newly formed ostecyte still shows osteoblastic activity. In the resorptive phase the osteocyte is capable of resorbing the bone matrix which forms the border of its lacuna, while in the degenerative phase the cell fragments and eventually disappears.

The lining cells are a layer of very flat endothelial-like cells that cover the inactive surfaces of bone. They are very thin and their function is practically unknown, though they might play a role in separating the interstitial from the bone fluids.

Osteoclasts are giant, multinucleated cells attached to the bone surface whose fuction is to resorb bone. The actual mechanism of mineral resorption is not very well understood, though current findings support an extracellular dissolution of the bone mineral followed by digestion of the organic components.

Normal bone metabolism involves continuous bone remodelling which occurs at the level of the bone remodelling unit, also called the "basic multicellular unit" or BMU [23]. Bone volume must be maintained constant during the remodelling by tight coupling between osteoblastic and osteoclastic activity. A BMU goes through different phases of a dynamic process which begins with the activation of osteoclasts on the bone surface (activation phase), continues with the resorption of bone matrix and formation of Howships's lacuna (resorption phase), the disappearance of the osteoclasts which are substituted by mononuclear cells (reversion phase), and the disappearance of these cells and reappearance of osteoblasts with reparation of the resorption lacuna (formation lacuna). The local mechanisms which regulate the coupling between osteoblastic and osteoclastic activity are not well understood and await further study.

1.1.2 Bone mineral chemistry

The study of the physico-chemical properties of the mineral component of skeletal tissue has advanced significantly since Neuman and Neuman's pioneering treatise on the subject [15]. The dominant apatitic phase has been well characterized, and the dynamics of calcium phosphate precipitation in aqueous solution and in vitro systems reasonably well understood. However, *in vivo* deposition processes are less well understood and their study poses a significant challenge. The following discussion draws heavily on some recent review articles on the state of bone mineral chemistry research [24, 25].

The first step in the formation of the mineral is the nucleation of the crystal, the creation of a small cluster of ions capable of growth and survival as a crystal. A necessary thermodynamic condition for nuclei formation is that the Gibbs free energy of the reactant ions in solution exceed the free energy of the precipitated

phase. Otherwise any crystals that formed would quickly dissolve again. In addition, the energy expended in creating the cluster surface should exceed the energy released by ion bonding within the crystal. This energy barrier can be quite high for sparingly soluble salts such as apatites, and must be lowered substantially for nucleation to take place on a reasonable time scale.

The presence of foreign solids can lower the threshold for nucleation to occur if they

1. have a strong affinity for the ions being precipitated, and

2. have a surface topology closely matching that of the precipitated surface.

The dimensions of an apatitic nucleus is probably on the order of 1-2 nm [26], which is much smaller than the size of a bone crystal. Crystal growth then accounts for most of the subsequent increase in the mass of the crystal.

There has been much debate on the exact chemical nature of the first calcium phosphates precipitated. Termine and Posner [27, 28] proposed that amorphous calcium phosphate is the first mineral deposited in the calcification process, and that it acts as a metabolically active, metastable precursor of crystalline bone apatite. These amorphous calcium phosphates are considerably more soluble in water than the apatites and hence face a smaller energy barrier. An octacalcium phosphate (OCP) precursor has been proposed by Brown *et al.* [9, 10]. The highly hydrated phases can occur in preference to apatite because, although less stable thermodynamically, they apparantly have much lower surface energies which reduce the net energy required for their *de novo* formation. Glimcher and co-workers [4, 29] initially detected the presence of brushite in the lower density fractions of embryonic chicken bone, using X-ray and electron diffraction, and ^{31}P NMR spectroscopy. However, they later ascribed the presence of the brushite to the sample preparation process [30]. Pellegrino and Blitz studied the sequence of chemical transformations in developing bone and showed an inverse relationship between monohydrogen phosphate and carbonate ions, where the decreasing monohydrogen phosphate content coincided with the formation of carbonate-apatite of the mature mineral [31, 32]. Carbonate can enter the apap-

tite lattice in substitution for hydroxyl groups (type A) and for phosphate groups (type B).

Rey *et al.* have recently shown that the surface of the mineral contains a number of labile non-apatitic domains. These domains are very reactive, and are initmately linked to the metabolic activity of the mineral. These environments were shown to be unstable, gradually disappearing as the mineral matured [17, 33].

Currently, bone mineral is considered to be composed primarily of a poorly crystalline, non-stoichiometric apatite similar to hydroxyapatite ($Ca_{10}(OH)_2(PO_4)_6$), containing HPO_4^{2-} and CO_3^{2-} as well as cations like Mg^{2+}. There is still controversy as to whether hydroxyl groups are present in bone mineral, as they have not been detected in the mineral by any technique. It is known that HPO_4^{2-} ion concentrations are the highest in newly deposited bone and that this concentration decreases as the mineral matures [17, 18, 19, 34, 35]. Other changes associated with the aging of the crystals are an increase in crystallinity and in carbonate content.

1.1.3 Mineral formation in vivo

All the extracellular fluids in equilibrium with serum are supersaturated with respect to apatite, and possibly OCP as well. It is therefore remarkable that the body has the ability to restrict mineralization to skeletal and other selected tissues. A systemic nucleation inhibitor is usually postulated as the means by which soft tissues prevent nucleation. However, in skeletal tissues, the inhibitor inactivation has to be very selective, both spatially and temporally, to account for the orderly manner in which bone is laid down.

Matrix vesicle calcification

These cell-derived, membrane-bound vesicular structures appear to be the extracellular loci for initial mineral deposition in some skeletal tissues [36, 37], such as calcified growth plate cartilage. Matrix vesicles give hard tissue cells the means to directly control the mineralization process and integrate it with other cellular functions. The

vesicles may also be able to protect the nascent crystals from the inhibitors in the systemic circulation. It is unclear whether the first mineral is formed by homogeneous or heterogeneous nucleation, and what the exact chemical nature of the initial phase is. The bulk of crystal growth occurs outside the vesicles, as the interior crystals gain access to the extravesicular space by physically breaching the bilayer and then continuing to grow or seeding new crystals.

Collagen calcification

In some tissues such as intramembranous bone and mantle dentin, both collagenous as well as vesicular mineral deposits occur. No connection has been established between mineral formed in matrix vesicles and that associated with collagen calcification. It appears that the *de novo* collagen calcification is precipitated by heterogeneous nucleation by an anionic non-collagenous protein. Once collagenous mineralization is initiated, the mineral spreads throughout the fibers in an orderly progressive manner by the multiplicative proliferation of many small plate-like crystals, all of which are approximately the same size. The underlying mineralization process is still not well understood. The crystals deposited on the collagen usually have their crystallographic *c*-axis aligned parallel to the fiber axis. Apatite crystals appear to be more randomly oriented in the direction perpendicular to the fiber axis. Once started, the mineralization of individual fibers in bone tissue occurs relatively rapidly compared to the overall advancement of the mineralization front.

1.1.4 The characterization of bone mineral density

Many techniques are available for measuring the mass and apparent density of bone mineral, and for characterizing the microarchitecture of trabecular (spongy) bone, both *in vivo* and *ex vivo*. Bone mineral content (BMC, the mass of the mineral in grams) is most accurately measured gravimetrically, *ex vivo*, by ashing the specimen to drive off water and all organic substances. *In vivo* BMC may be measured by single and dual energy γ-ray photon absorptiometry (SPA and DPA) [38, 39], single and

dual energy quantitative computed tomography (QCT) [40], densitometry of plane film x-ray radiographs, dual-energy x-ray absorptiometry (DXA—now considered the "gold standard" for clinical applications) [41], neutron activation [42, 43, 44] and ultrasound [45, 46]. Quantitative solid state ^{31}P MRI shows promise as a novel tool for BMC quantitation [47]. Techniques such as DXA yield a type of "projective" density in g cm^{-2}. Although not a true density in g cm^{-3}, this DXA-derived density has been shown to correlate with the risk of fracture [48, 49].

1.2 Solid state NMR study of bone mineral

Solid state ^{31}P NMR spectroscopy has been used extensively to study synthetic calcium phosphates and biological minerals [34, 35, 50, 51, 52, 53, 54, 55, 56, 57, 58, 59], as the NMR visible ^{31}P nucleus has a natural abundance of 100%. Other solid state experiments have been performed on ^{1}H, ^{19}F, and ^{13}C nuclei [20, 60, 61, 62, 63, 64, 65, 66, 67]. Some of the important studies relating to bone mineral chemistry are outlined below.

Herzfeld *et al.* used ^{31}P spectroscopy to study samples of synthetic brushite, hydroxyapatite, and low (< 1.8 g cm^{-3}) and high (> 1.8 g cm^{-3}) density bone samples. In the non-spinning proton-decoupled phosphorus spectra they observed the presence of a broad tail in the low-density bone fraction that was not present in the high density fraction. Upon spinning the samples and comparing the intensities of the rotational sideband patterns, they observed that the spectra from the high density fraction were very similar to synthetic hydroxyapatite, while the spectra of the low density fraction contained a significant amount of brushite. The presence of HPO_4^{2-} was identified by the increase in the number of spinning sidebands due to its chemical shift anisotropy.

In a comparison of synthetic calcium phosphates and bone mineral [34, 35], Griffin and coworkers used standard ^{31}P Bloch decay, ^{1}H–^{31}P cross polarization, and dipolar suppression techniques to evaluate a group of synthetic calcium phosphates and mineral deposits in chicken bone. The synthetics included crystalline hydrox-

yapatite, two type B carbonatohydroxyapatites containing 3.2 % and 14.5 % substituted CO_3^{2-} groups, type A carbonatohydroxyapatite, a hydroxyapatite containing about 12% HPO_4^{2-}, a poorly crystalline hydroxyapatite, amorphous calcium phosphate, brushite, monetite and octacalcium phosphate. They demonstrated that the isotropic and anisotropic chemical shifts, together with data from proton-suppression techniques, could be used to differentiate the synthetic calcium phosphate compounds from one another. None of the NMR spectra of the mineral samples, obtained from 17-day-old embryonic chicks, 5-week, 30-week and 1 year old postnatal chickens, had chemical shift values and rotational sideband patterns that matched those of the synthetics. Using mathematical modelling techniques to fit the spectra of bone to a linear combination of spectra of the synthetics, they suggested that the best model for bone mineral was hydroxyapatite containing $\approx$ 5–10% CO_3^{2-} and $\approx$ 5–10% HPO_4^{2-} groups, with the HPO_4^{2-} being present in a brushite-like configuration. They also observed that the fraction of HPO_4^{2-} was highest in the youngest bone and decreased with increasing age of the specimen.

More recently, Wu *et al.* [50, 68] were able to suppress the PO_4^{3-} peak and directly observe the acid phosphate peak, using a differential cross polarization (DCP) [69, 70, 71] technique with magic angle spinning (MAS). The technique, which makes use of the different proton-phosphorus cross polarization rates for phosphorus atoms in non-protonated phosphate and monohydrogen phosphate moieties, allowed them to directly measure the isotropic and anisotropic chemical shifts of the monohydrogen phosphate group in bone. The isotropic chemical shift of the HPO_4^{2-} group in bone was the same as that of the HPO_4^{2-} in octacalcium phosphate, while its anisotropic chemical shift corresponded to that of brushite. Thus it was observed that the HPO_4^{2-} group in bone is unique and cannot be modelled exactly by any of the synthetics.

Solid state techniques have also been used to evaluate the bioabsorption of synthetic apatite compounds used to promote bone healing and remodelling [59, 72], and to study the biocompatibility of calcium phosphate bioceramics used in implants [73]. Conventional radiographic studies are insensitive to the chemical differences between the natural bone mineral and the synthetic and are unreliable in determining the

degree of resorption or remodelling.

1.2.1 Development of *in vivo* solid state techniques

The NMR study of bone is complicated by the usual problems of solid state NMR, including long spin-lattice relaxation times (T_1), short spin-spin relaxation times (T_2), and chemical shift anisotropies. While conventional high-field solid state NMR techniques can overcome most of these problems, many of these techniques, such as magic angle spinning and high power rf decoupling, cannot be used for *in vivo* applications. In order to detect the small signals arising from the bone, it is necessary to use a surface coil that can be placed adjacent to the area of interest in order to increase the filling factor of the coil and improve the detection sensitivity of the experiment. However, the use of a surface coil results in significant B_1 inhomogeneities and often necessitates extensive modification of the NMR techniques used. This is especially true when attempting quantitative measurements, spatial localization techniques, or any methods sensitive to the size of the rf flip angles.

Brown *et al.* have proposed using the relative peak areas of the ^{31}P Bloch decay spectrum of bone and a reference standard in order to quantitatively determine the mineral content of the bone. Stressing the non-invasive nature, and the absence of ionizing radiation, they suggested the use of low-resolution, solid state ^{31}P spectroscopy in the evaluation and treatment of osteoporosis [56, 74, 75, 76]. Li *et al.* have demonstrated one dimensional spatial localization in bovine bone with a surface coil, while Dolecki *et al.* have reported *in vivo* ^{31}P T_1 measurements that appear to correlate linearly with mineral density [77]. Ackerman and coworkers performed solid state imaging of calcium phosphates and bone mineral *ex vivo* and obtained chemically sensitive solid state MR images of bone mineral [78, 79]. Wu *et al.* have proposed using solid state NMR imaging to obtain spatial distributions of bone mineral content, which directly provides a measure of bone mineral density, an index that is widely used in the diagnosis of osteoporosis [47]. They use a large three-dimensional frequency encoding gradient, with a single gradient evolution period during each aquisition and reconstruct the image using backprojection reconstruction techniques.

Chapter 2

NMR Methodology

There is nothing that nuclear spins will not do for you, as long as you treat them as human beings.

Erwin L. Hahn

2.1 Introduction to cross polarization

Cross polarization is a technique in which the polarization of one spin species is transferred to a second spin species by a resonant process in the rotating frame. The landmark paper of Hartmann and Hahn [80] established the conditions under which two dissimilar spins are able to transfer polarization between them. They detected the transfer of polarization by measuring the reduction in the magnetization of ^{35}Cl (abundant species) after contact in the rotating frame with ^{39}K (rare species) in a sample of $KClO_3$. The fastest polarization transfer occurs when the Zeeman energy splittings of the two spin species in the rotating frame are equal, called the Hartmann-Hahn condition, and is mediated by the dipolar coupling between the two spin systems. The matching of energy levels is equivalent to setting the rotating frame Larmor frequencies of the two spins equal to each other.

Pines, Gibby and Waugh suggested direct detection of the rare spin polarization, using repeated transfers of polarization from the abundant spin system followed by decoupling of the abundant spins during detection to obtain high-resolution spectra

[81, 82]. Most solid state cross polarization experiments nowadays use this direct detection scheme.

Cross polarization techniques are used in samples that have two or more spin species, when one or more of the following goals must be met.

1. Enhance the detection sensitivity of a spin species that is either rare (chemically and/or isotopically dilute), has a low gyromagnetic ratio, or both, in the presence of an abundant spin species with a larger gyromagnetic ratio.

2. Shorten the recycle time when observing a spin that has a long T_1, if the second spin has a shorter T_1.

3. Perform spectral editing by either selectively enhancing or suppressing those spins of one species that are strongly coupled to the second spin species.

The cross polarization techniques proposed by Hartmann *et al.* and Pines *et al.* require the simultaneous irradiation of the sample at the resonance frequencies of the two nuclei. Ideally the magnitude of both these fields should be much larger than the local dipole-dipole fields in the sample. This represents a significant problem when applied to lossy samples such as biological tissues. The rf power absorption scales with the square of the rf field amplitude and can produce tissue heating. An alternative cross polarization technique, called adiabatic demagnetization in the rotating frame (ADRF) cross polarization deposits significantly less power when compared to spin-lock CP techniques, and is hence easier to adapt to *in vivo* application. It involves the initial creation of dipolar order in one spin system followed by the transfer of this polarization to the Zeeman system of a second spin system. The ADRF-CP technique has been known for over thirty years though it has been used infrequently.

2.2 Creating dipolar order

2.2.1 Adiabatic demagnetization in the rotating frame

The technique of ADRF was proposed by Slichter and Holton [83], and demonstrated the validity of Redfield's hypothesis of spin temperatures in the rotating frame [84] down to rf fields much smaller than the local fields of the sample. In their experiments on NaCl, they initially set the static field off-resonance with B_1 turned off for a long time to achieve thermal equilibrium between the spins and the lattice. The B_1 field was then turned on, and the *static field* brought to resonance. The change of B_0 was sufficiently slow for thermodynamic reversibility to be possible, but fast enough to prevent spin-lattice relaxation from being significant. In order to be ensure reversibility, the nucleus must precess many cycles in the time it takes the effective field to change significantly. Their results showed that the demagnetization achieved on resonance was reversible for all values of B_1. With the B_1 field much larger than the local field B_L , the spins are spin-locked along the B_1 field, while when B_1 is much less than the local field B_L, the individual spins are aligned along their local fields. Since these local fields are randomly distributed in space the bulk magnetization tends towards zero. However, the alignment of the spins has not changed, and the spins have the same degree of order as at the start of the experiment.

Anderson and Hartmann further extended the Redfield theory down to the case where B_1 is zero [85], in their detailed study of the rotating frame demagnetized state which appeared in the same issue of Physical Review as Hartmann and Hahn's classic paper. In addition to Slichter and Holton's method of a fast passage to the center of the line using a low intensity rf field, they also performed ADRF by initially spin-locking the magnetization with a strong rf field and then reducing the amplitude of this rf field adiabatically to zero. The spin-locking can be performed either with a fast passage onto resonance with a strong rf field, or a "hard" 90 degree pulse followed by a 90 degree phase shift of the rf to align the magnetization along the tranverse field.

The initially spin-locked spins are described by a Boltzmann distribution with a

temperature much lower than the lattice temperature. As the rf field is adiabatically reduced to zero, this Boltzmann distribution is preserved even as the spacing between the energy levels changes. It is important to note that this is possible only because the Zeeman energy levels are equally spaced, and the spacing is proportional to the strength of the rf field. At the end of the demagnetization, the spins are still described by a Boltzmann distribution, though with a lower temperature than at the start. At the end of the demagnetization the spins are aligned along their local dipolar fields, and are thus ordered with respect to their local fields. This high degree of ordering in the spin system is equivalent to a low spin temperature. In this dipolar state the Zeeman energy is zero, but the dipole-dipole energy is significantly different from zero. If the process is truly adiabatic the order present in the Zeeman alignment with respect to the external dc field is now resident in spin alignment in the dipole-dipole fields. The order will persist for times of the order of T_1 if the dc field is large. In systems containing many different spin species, preparation of the lowest possible dipole-dipole temperature requires successive ADRF of each of the spin species [86].

Recently Hatanaka and Hashi have observed a significant degree of irreversibility in the ADRF process in experiments on ^{27}Al in Al_2O_3 [87], which was absent in ^{19}F in CaF_2 and ^{7}Li and ^{19}F in LiF. They have suggested that the source of the irreversibility is thermal mixing between the Zeeman and dipolar systems during the demagnetization process. However, if the unequally spaced energy levels (due to the quadrupolar interaction) are not shifted proportionally during the demagnetization, the system cannot be described by a Boltzmann temperature during the demagnetization process.

2.2.2 Pulse methods

Jeener *et al.* proposed a fast method to prepare a dipolar ordered system using a sequence of two rf pulses, 90 degrees out of phase with one another and separated by a time of the order of T_2 [86, 88]. They observed that the system is not in a state of internal quasiequilibrium after the application of the second pulse, but that it approaches this state in a time of the order of T_2 for most regularly organized

spin systems. This evolution towards equilibrium results in an irreversible creation of entropy, reducing the efficiency of the transfer of order between the Zeeman and dipolar systems. For a single spin ingredient the greatest transfer of order occurs when the first pulse is a $\pi/2$ pulse, and the second pulse is a $\pi/4$ pulse phase shifted from the first by 90 degrees, applied at a time τ when the slope of the Zeeman component of the fid of the first pulse is at a maximum. Assuming purely dipolar coupling and a Gaussian lineshape, the maximum efficiency in this case is 52%. They used a $\pi/4$ pulse to transfer the dipolar order back to Zeeman order and detect it.

In the case of multiple spin species, the first pulse should still be $\pi/2$ and the phase difference between the pulses 90 degrees, but the angle of the second pulse and the interval between the pulses will now depend on the relative magnitudes of the homonuclear and heteronuclear spin coupling terms.

2.3 ADRF cross polarization

In their study of the demagnetized state, Anderson and Hartmann [85] suggest that in a sample containing multiple spin species, the different spin systems will readily couple in the ADRF state. If one system is prepared in an ordered ADRF state, part of this order can be transferred to other systems by energy-conserving multiple spin flips. Thus they suggest that following the ADRF of one spin species, it is possible to adiabatically remagnetize at the frequency of a second spin species and lower the entropy of the second spin system. Hartmann and Hahn also discussed cross polarization following ADRF in their double resonance paper [80].

In their experiment, Anderson and Hartmann explored whether two spin systems in the ADRF state would undergo energy-conserving spin-flips and reach a common temperature. The experiment was carried out on a sample of lithium metal, enriched to 25% ^{6}Li. In the absence of z-axis modulation, rf irradiation at the ^{6}Li frequency had no effect on the ^{7}Li system in the ADRF state. The presence of the ^{6}Li spins was only detected in the ^{7}Li resonance when the ^{7}Li ADRF state was monitored after rf irradiation at the ^{6}Li frequency in combination with z-axis modulation. They

suggest that the combination of rotary saturation in the ^{6}Li system combined with ^{6}Li–^{7}Li dipolar coupling led to the warming of the ^{7}Li spin system. The maximum ^{6}Li B_1 field used was 0.2 G and the size of the z-axis modulation field was 0.1 to 1.0 G. The experiment thus suggests a coupling between the ^{6}Li Zeeman system and the ^{7}Li dipolar system.

Lurie and Slichter used ADRF-CP to study lithium metal, containing 92.6% ^{7}Li and 7.4% ^{6}Li at 1.5K [89]. They performed an ADRF of the ^{7}Li spins, and observed the decrease in magnetization of this system produced by heating the ^{6}Li spins. The heating of the ^{6}Li system was performed by applying an rf at the ^{6}Li resonance frequency for a fixed time period during which the spin temperatures of the two systems equilibrate. After the rf was turned off and the S spin magnetization allowed to decay, the rf was turned on again and the process repeated a number of times. As the heat capacity of the ^{7}Li spins is much greater than that of the ^{6}Li, the ^{6}Li rf needs to be cycled many times before a significant change is observed in the ^{7}Li magnetization. The warming of the ^{7}Li spins brought about by contact with the ^{6}Li spins represents a heat flow between two systems at different temperatures, and results in an irreversible loss of order, or an increase in entropy.

When the applied ^{7}Li rf field was larger than the local fields, essentially producing a spin-locked state with respect to the applied rf rather than a true ADRF state, they observed cross polarization over a range of values about the Hartmann-Hahn matching condition. As the contact time between the spins was increased, the range of values of the ^{6}Li B_1 field over which mixing could occur also increased. In the ADRF experiment, they observed that the rate of mixing between the ^{6}Li and ^{7}Li was inversely proportional to the ^{6}Li B_1 field, though the range of ^{6}Li B_1 amplitudes over which mixing took place increased. Their data indicates that the B_1 field used by Anderson and Hartmann in their experiment was too small to detect appreciable mixing in the absence of the rotary saturation.

McArthur *et al.* performed an extensive study of the ADRF-CP of the 100% naturally abundant ^{19}F and 0.013% abundant ^{43}Ca spins in a single crystal of CaF_2 [90], in which they investigated the dipolar fluctuation spectrum of the ^{19}F spins and

the thermodynamics and kinetics of the cross relaxation process.

Their preparation of the ADRF state consisted of a $\pi/2$ pulse followed by a 90 degree phase shift of the rf field to spin-lock the magnetization. The rf field was then adiabatically reduced to zero. They monitored the dipolar state of the ^{19}F by applying a $\pi/4$ pulse, as used in the Jeener-Broekaert sequence. The Zeeman and dipolar signals excited by the pulse are out of phase by 90 degrees and can thus be separated.

In their first series of experiments they were able to measure the relative heat capacities of the two spin systems and the cross-relaxation time as a function of the ^{43}Ca B_1 field, using a multiple-contact scheme similar to that used by Lurie and Slichter. Their results indicated that the cross-relaxation displays exponential behaviour, with $(T_{IS})^{-1} \propto \exp\{-\omega_{1Ca}\ \tau_c\}$, where ω_{1Ca} is the rotating frame Larmor frequency of the ^{43}Ca and τ_c is the correlation time of the random I–S spin flips. Spin-diffusion effects were largely absent. When rotary saturation was used to heat the ^{43}Ca spins, they did observe spin-diffusion limitation of the cross-relaxation rates. In this situation spin diffusion is not fast enough to maintain a Boltzmann distribution among the spins during the cross polarization process.

During the pulsed double resonance experiments they noted that the initial behaviour of the ^{43}Ca rotating frame magnetization consisted of a small step function accompanied by short lived oscillations of similar magnitude at a frequency ω_{1Ca}, representing the change in the energy of the ^{19}F–^{43}Ca coupling term of the dipolar spin Hamiltonian in response to the applied ^{43}Ca rf field. They were first observed by Jeener *et al.* who noted that in the case of a strong irradiation exactly on resonance, the oscillations occured at *twice* the Larmor frequency in the effective field [91]. These oscillations are the rotating frame analogues of those detected by Strombotne and Hahn [92].

Using an indirect detection scheme, they also measured the T_{1D} of the ^{43}Ca nuclei and obtained a value of 202 ± 19 s compared to a value of 4.1 s for ^{19}F. This appears to indicate that the two dipolar reservoirs are not in thermal contact with each other in the ADRF state (or that the thermal mixing time is much slower than the T_{1D} of

the ^{43}Ca nuclei). The low abundance of the ^{43}Ca spins raises questions about whether these nuclei can actually be considered a single reservoir rather than a collection of isolated spins. In contrast, the single value of spin lattice relaxation time observed for different species in multiple spin systems in the laboratory frame adiabatic demagnetization experiment, for example in ^{6}Li and ^{7}Li, indicated the strong thermal mixing between the two dipolar reservoirs in that situation [93]. In the rotating frame relaxation experiments of Bloembergen and Sorokin on CsBr, the spin-lock fields were not extended to the low-field case where a single relaxation time is expected, though they did find evidence that the relaxation of the ^{133}Cs spins was influenced by the dipolar coupling to the ^{79}Br and ^{81}Br spins [94].

2.4 Mathematical formalism

The discussion in this section draws heavily from the treatments of Wolf [95] and Mehring [96]. A rigorous description of the thermodynamics of spin systems has been given by Philippot [97].

2.4.1 Basic Hamiltonians

The strongly coupled spins of a solid can usually be considered to be weakly coupled to the non-spin degrees of freedom or the lattice. Thus the Hamiltonian of the sample in an external magnetic field can be written as

$$\mathcal{H} = \mathcal{H}_S + \mathcal{H}_{SL} + \mathcal{H}_L \tag{2.1}$$

where $\mathcal{H}_S$ represents the Hamiltonian of the completely isolated spin system, $\mathcal{H}_L$ the Hamiltonian of the lattice and $\mathcal{H}_{SL}$ the coupling between the spin system and the lattice. In general the isolated spin Hamiltonian can be written as

$$\mathcal{H}_S = \mathcal{H}_Z + \mathcal{H}_D^{RL} + \mathcal{H}_{ex} + \mathcal{H}_Q^{RL} + \mathcal{H}_{e-n}^{RL}. \tag{2.2}$$

The terms in Equation (2.2) above are defined below. In defining the isolated spin Hamiltionian we only consider the rigid-lattice (RL) contributions, as the components due to lattice-induced motions leads to spin-lattice coupling.

$\mathcal{H}_Z$ $\equiv$ the Zeeman interaction of the nuclear spins with the external magnetic field (both static and time varying)

$\mathcal{H}_D^{RL}$ $\equiv$ the direct dipolar interaction of the magnetic moments of the nuclear spins

$\mathcal{H}_{ex}$ $\equiv$ the exchange-coupling Hamiltonian, a purely quantum-mechanical interaction produced by the overlap of the wave functions of half-integer spins (Fermi-Dirac statistics)

$\mathcal{H}_Q^{RL}$ $\equiv$ the nuclear electric quadrupolar interaction arising from non-spherical nuclear charge distributions of spins with spin quantum number ≥ 1

$\mathcal{H}_{e-n}^{RL}$ $\equiv$ the interaction between the nuclear and electronic magnetic moments. In substances showing electron paramagnetism, these interactions include orbital hyperfine coupling, electron-nuclear direct dipolar coupling, and the Fermi contact interaction which is the origin of the Knight shift in metals. In diamagnetic substances the first order interaction vanishes, though the remaining second-order interactions produce chemical shifts, and the pseudo-exchange and pseudo-dipolar couplings due to the indirect interaction of magnetic moments via conduction electrons or ion cores.

We are primarily concerned with the Zeeman and direct dipolar interactions in spin-1/2 systems in this thesis. We also consider interactions that take place on a time scale short compared to the spin-lattice relaxation time. Thus we can simplify Equations (2.1) and (2.2) to give $\mathcal{H} = \mathcal{H}_S$ where $\mathcal{H}_S = \mathcal{H}_Z + \mathcal{H}_D^{RL}$. The dipolar

Hamiltonian can be further divided into secular and non-secular components (defined with respect to $\mathcal{H}_Z$)

$$\mathcal{H}_D^{RL} = \mathcal{H}_D^{(0)RL} + \mathcal{H}_D^{(n)RL}. \tag{2.3}$$

The Zeeman and dipolar Hamiltonians are discussed in more detail in Appendix A.

2.4.2 Single spin species

The laboratory frame

Consider a sample containing N_I nuclei of a single spin species I, placed in a static external magnetic field $B_0\hat{k}$. The density of nuclear spins is low enough that there is little overlap of the spin wave functions. Thus we can apply Maxwell-Boltzmann statistics to the nuclear spin system. Even when the spins are not in thermal equilibrium with the lattice, they can still be coupled together in a quasiequilibrium state, described by a Boltzmann distribution with a temperature different from that of the lattice. The density matrix of the system can then be written as

$$\sigma = \frac{1}{Z} \exp(-\mathcal{H}_S/k\theta_S) \tag{2.4}$$

$$Z = \mathrm{Tr}\{\exp(-\mathcal{H}_S/k\theta_S)\} \tag{2.5}$$

where θ_S is the spin temperature. In the high temperature approximation we can replace the exponential by the first two terms of its power series expansion as the splitting of the Zeeman energy levels is small compared to the average thermal energy $k\theta$, yielding

$$\sigma \cong \frac{1}{Z}(1 - \frac{\mathcal{H}_S}{k\theta_S}). \tag{2.6}$$

During spin-lattice relaxation, this temperature θ_S relaxes towards the lattice temperature θ_L. In the absence of an rf field, the average spin energy is

$$E = <\mathcal{H}_S> = \mathrm{Tr}\{\sigma\mathcal{H}_S\} = -\frac{C(B_0^2 + B_L^2)}{\theta_S}, \tag{2.7}$$

where C is Curie's constant and B_L the local field in the laboratory frame is defined by

$$B_L^2 = \frac{\mathrm{Tr}\{(\mathcal{H}_D^{RL})^2\}}{M_z^2}. \tag{2.8}$$

In this high temperature approximation, the total spin entropy is given by

$$S = S_Z + S_D \tag{2.9}$$

where S_Z and S_D are the entropies associated with the Zeeman and dipolar systems respectively. In the high temperature approximation we have [86]

$$S_Z = -\frac{1}{2}\frac{CB_0^2}{\theta_S^2} \qquad S_D = -\frac{1}{2}\frac{CB_L^2}{\theta_S^2}. \tag{2.10}$$

The heat capacities of the Zeeman and dipolar systems are given by

$$C_Z = C \cdot B_0^2 \qquad C_D = C \cdot B_L^2. \tag{2.11}$$

B_L contains both secular and non-secular terms, derived from the respective terms of the Hamiltonian,

$$B_L^2 = (B_L^{(0)})^2 + (B_L^{(n)})^2. \tag{2.12}$$

In order for a temperature to be established among the spins, it is necessary that diffusion processes exist to transport the spin energy through the sample. This diffusion can take place by pure spin diffusion due to energy conserving spin flips, or motion-induced diffusion requiring mass transport. These diffusion processes must operate on a time scale that is short compared to any of the interactions being studied in order for the spin temperature concept to be valid.

The individual parts of the spin reservoirs and their interactions are illustrated in Figure 2-1. As $\mathcal{H}_Z$ and $\mathcal{H}_D^{(0)RL}$ commute, they do not interact directly, but can interact via $\mathcal{H}_D^{(n)RL}$. This results in thermal mixing between $\mathcal{H}_Z$ and $\mathcal{H}_D^{(0)RL}$. It is usually possible to assign different temperatures to these sub-reservoirs during the thermal mixing process. In contrast, $\mathcal{H}_D^{(n)RL}$ and $\mathcal{H}_Z$ do not commute so any fluctuations in

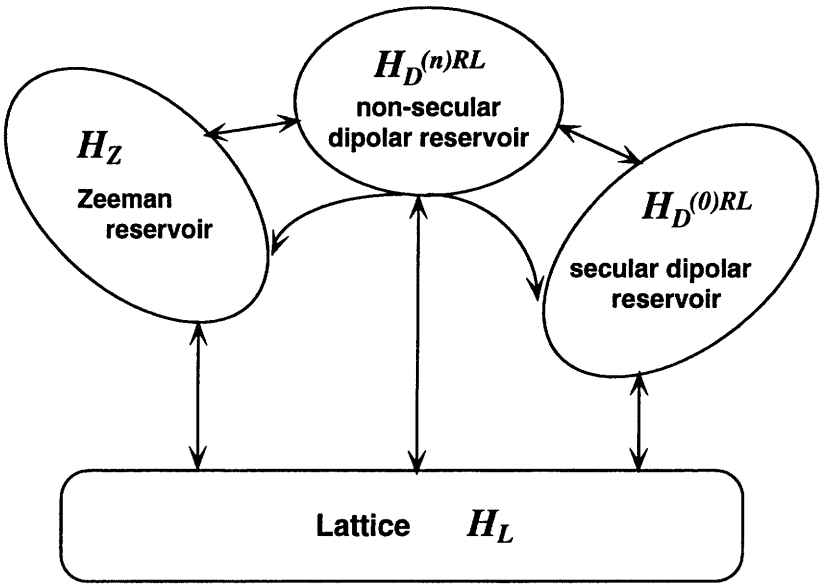

Figure 2-1: The important spin-reservoirs and interactions for a single spin species in the laboratory frame. Due to the isomorphism between the tilted rotating frame and the laboratory frame the same picture is valid in the tilted rotating frame, with each of the Hamiltonians replaced by its rotating frame equivalent.

one are immediately communicated to the other. Similarly $\mathcal{H}_D^{(n)RL}$ and $\mathcal{H}_D^{(0)RL}$ do not commute and interact instantaneously. When $\mathcal{H}_Z$ is large compared to $\mathcal{H}_D^{(0)RL}$ (in large Zeeman fields), $\mathcal{H}_D^{(n)RL}$ is more tightly coupled to $\mathcal{H}_Z$. As $\mathcal{H}_Z$ becomes comparable to $\mathcal{H}_D^{(0)RL}$, all the sub-reservoirs are well-coupled. Note that while $\mathcal{H}_D^{(n)RL}$ is described as a sub-reservoir due to its non-zero average energy, it is always strongly coupled to one of the secular reservoirs.

In a weak Zeeman field, the thermal mixing time $T_m \approx T_2^{RL}$ and thus the three reservoirs are tightly coupled and have the same spin temperature. When the Zeeman fields applied become comparable to the local fields of the sample, the concept of well defined energy levels for individual spins breaks down, and the entire system needs to be treated together with its $(2I+1)^{N_I}$ levels described by a common temperature θ_S.

In a large Zeeman field the thermal mixing time increases considerably from its value at low field, and $T_m \gg T_2^{RL}$. If T_m is long compared to the correlation time of the fluctuations inducing spin-lattice relaxation, $\mathcal{H}_D^{(0)RL}$ cannot maintain a common temperature with $\mathcal{H}_Z + \mathcal{H}_D^{(n)RL}$. There are now (2I+1) different Zeeman levels, and while $\mathcal{H}_D^{(0)RL}$ does not participate in a common temperature with $\mathcal{H}_Z$, it plays an important role in producing spin diffusion and establishing a temperature.

The tilted rotating frame

If an rf field of amplitude B_1 and frequency ω is now applied, we can transform the description of the spin system into a coordinate system that is precessing with frequency ω about the direction of the constant Zeeman field. The rotation is described by the unitary operator

$$R_z(\omega t) = \exp\{i\omega t I_z\}. \tag{2.13}$$

The effective Zeeman field in this frame

$$B_{\text{eff}} = \left(B_0 - \frac{\omega}{\gamma}\right)\hat{z}_r + B_1\hat{x}_r \tag{2.14}$$

is oriented at an angle $\Theta = \arctan\left(\frac{B_1}{B_0 - (\omega/\gamma)}\right)$ with respect to the static field. By applying another unitary rotation we can tilt the z-axis along the effective field, with the corresponding rotational operator given by $R_{y_r}(\Theta) = \exp\{i\Theta I_y^r\}$. The resulting coordinate system is called the tilted-rotating (TR) frame. Neglecting the explicitly time-dependent terms, which are non-secular if $B_{\text{eff}} \gg B_L$, the resulting spin-Hamiltonian is

$$\mathcal{H}_Z^\rho = \mathcal{H}_Z^\rho + \mathcal{H}_D^{\rho\,RL}. \tag{2.15}$$

The Hamiltonians in the tilted rotating frame can be shown to be formally equivalent to those of the laboratory frame. The time independent dipolar Hamiltonian in Equation (2.15) is obtained from the transformation of $\mathcal{H}_D^{(0)RL}$ exclusively, as the terms corresponding to $\mathcal{H}_D^{(n)RL}$ become explicitly time dependent in the rotating frame and are dropped. The TR frame dipolar Hamiltonian can be expressed in terms of

its secular and non-secular contributions (now defined with respect to $\mathcal{H}_Z^\rho$),

$$\mathcal{H}_D^{\rho\,RL} = \mathcal{H}_D^{\rho\,(0)RL} + \mathcal{H}_D^{\rho\,(n)RL}. \tag{2.16}$$

Redfield's hypothesis allows us to define a density matrix in this representation

$$\sigma_\rho = \frac{1}{Z^\rho} \exp(-\mathcal{H}_S^\rho / k\theta_S^\rho) \tag{2.17}$$

$$Z^\rho = \mathrm{Tr}\{\exp(-\mathcal{H}_S^\rho / k\theta_S^\rho)\} \tag{2.18}$$

where θ_S^ρ is now the spin temperature in the tilted rotating frame. Using the high temperature approximation we find the spin energy in this frame

$$E^\rho = < \mathcal{H}_S^\rho > = \mathrm{Tr}\{\sigma_\rho \mathcal{H}_S^\rho\} = -\frac{C(B_{\mathrm{eff}}^2 + B_{L\rho}^2)}{\theta_S^\rho}, \tag{2.19}$$

where $\mathrm{B_{L\rho}}$ is the local field in the tilted rotating frame, and is defined by

$$B_{L\rho}^2 = \frac{Tr\{(\mathcal{H}_D^{\rho\,RL})^2\}}{(M_z^\rho)^2}. \tag{2.20}$$

The secular and non-secular components of this field are $\mathrm{B_{L\rho}^{(0)}}$ and $\mathrm{B_{L\rho}^{(n)}}$. While the total local field is constant, the relative magnitude of the secular and non-secular terms depends on the size of the off-resonance angle Θ.

In a weak Zeeman field where $\mathrm{B_{eff}} \leq \mathrm{B_{L\rho}}$, $\mathrm{T_m^\rho} \approx \mathrm{T_2^{RL}}$ the three reservoirs are tightly coupled and the entire system is again described by a single rotating frame spin temperature θ_S^ρ.

When $\mathrm{B_{eff}} \gg \mathrm{B_{L\rho}}$, the thermal mixing time between $\mathcal{H}_D^{\rho\,(0)RL}$ and $\mathcal{H}_Z^\rho$ increases considerably from its value at low field, and $\mathrm{T_m^\rho} \gg \mathrm{T_2^{RL}}$ and the two systems do not share a common temperature.

2.4.3 Multiple spin species

In a spin system with multiple spin species, the process of cross relaxation between the species that equilibrates their temperatures usually requires a finite amount of time. During this process different spin temperatures may be assigned to the individual sub-reservoirs of the entire spin system. The spin density matrix then takes the form

$$\sigma = \frac{1}{Z}\exp\{-\sum_{\alpha}\mathcal{H}_S^{(\alpha)}/k\theta_{S\alpha}\} = \prod_{\alpha}\left(\frac{1}{Z_\alpha}\exp\{-\mathcal{H}_S^{(\alpha)}/k\theta_{S\alpha}\}\right) \tag{2.21}$$

Two spin system in the laboratory frame

Consider a sample containing N_I and N_S spins of two dissimilar spin-1/2 systems I and S with gyromagnetic ratios γ_I and γ_S respectively, in an external magnetic field $B_0\hat{k}$. The spin-Hamiltonian of this system is given by

$$\mathcal{H}_S = \mathcal{H}_{ZI} + \mathcal{H}_{ZS} + \mathcal{H}_{DII}^{RL} + \mathcal{H}_{DSS}^{RL} + \mathcal{H}_{DIS}^{RL} \tag{2.22}$$

Each of the dipolar terms has secular and non-secular contributions. The non-secular contributions of $\mathcal{H}_{DIS}^{RL}$ contain components which commute with $\mathcal{H}_{ZI}$ or with $\mathcal{H}_{ZS}$ but not both. We can thus express this non-secular Hamiltonian as

$$\mathcal{H}_{DIS}^{(n)RL} = \mathcal{H}_{DIS}^{I(n)RL} + \mathcal{H}_{DIS}^{S(n)RL} + \mathcal{H}_{DIS}^{IS(n)RL}. \tag{2.23}$$

The different sub-reservoirs and interations are shown in figure 2-2.

The dipolar local field of the system is defined as

$$B_L^2 = \frac{Tr\{(\mathcal{H}_D^{RL})^2\}}{\hbar^2\{\gamma_I^2 Tr(I_z^2) + \gamma_S^2 Tr(S_z^2)\}} \tag{2.24}$$

$$\tag{2.25}$$

$$= B_{LI}^2 + B_{LS}^2 + B_{LIS}^2 \tag{2.26}$$

where each of these contributions can further be sub-divided into secular and non-secular components.

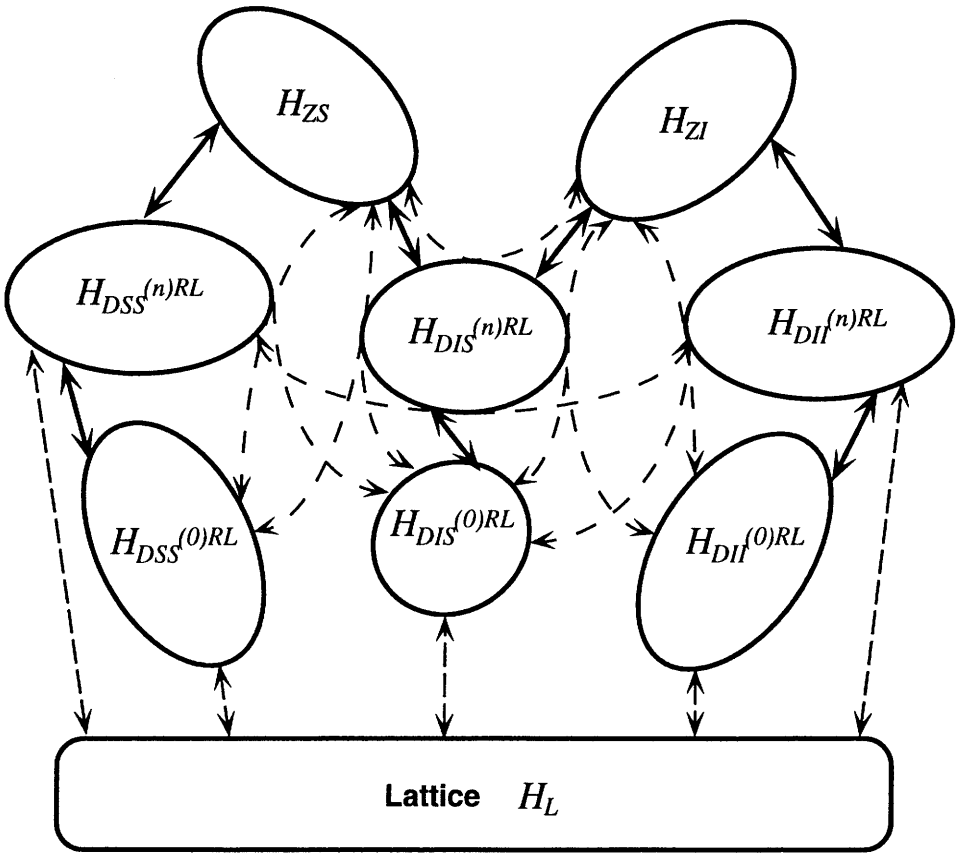

Figure 2-2: The different secular and non-secular reservoirs and interaction terms in the two spin situation. The introduction of the second spin species increases the complexity of the spin system greatly. As a result, simplifying assumptions are usually used in studying these systems.

Internal equilibrium between the different sub-reservoirs of the spins is achieved by the following five processes:

1. thermal mixing between $\mathcal{H}_{DII}^{(0)RL}$ and $\mathcal{H}_{ZI}$ via $\mathcal{H}_{DII}^{(n)RL}$ and $\mathcal{H}_{DIS}^{IS(n)RL} + \mathcal{H}_{DIS}^{I(n)RL}$;
2. thermal mixing between $\mathcal{H}_{DSS}^{(0)RL}$ and $\mathcal{H}_{ZS}$ via $\mathcal{H}_{DSS}^{(n)RL}$ and $\mathcal{H}_{DIS}^{IS(n)RL} + \mathcal{H}_{DIS}^{S(n)RL}$;
3. thermal mixing between $\mathcal{H}_{DIS}^{(0)RL}$ and $\mathcal{H}_{ZI}$ via $\mathcal{H}_{DII}^{(n)RL}$ and $\mathcal{H}_{DIS}^{IS(n)RL} + \mathcal{H}_{DIS}^{I(n)RL}$;
4. thermal mixing between $\mathcal{H}_{DIS}^{(0)RL}$ and $\mathcal{H}_{ZS}$ via $\mathcal{H}_{DSS}^{(n)RL}$ and $\mathcal{H}_{DIS}^{IS(n)RL} + \mathcal{H}_{DIS}^{S(n)RL}$; and
5. cross relaxation between $\mathcal{H}_{ZI}$ and $\mathcal{H}_{ZS}$ via $\mathcal{H}_{DIS}^{IS(n)RL}$.

The characteristic times of all these processes depends strongly on the strength of the Zeeman field. At high field these times become very long and thermal mixing and cross relaxation are strongly inhibited. Cross relaxation is the most important of these processes for establishing internal equilibrium. It is most effective when the energy-level spacings of the I and S spins are almost equal. This is almost never satisfied in high Zeeman fields due to the difference between γ_I and γ_S. In this case separate spin temperatures θ_S and θ_I have to be assigned to the I- and S-spin reservoirs. In addition, the long thermal mixing times can result in different Zeeman and secular dipolar temperatures within each spin system. In low Zeeman fields however, thermal mixing and cross relaxation may take place fast enough so that the entire system is characterized by a single spin temperature. In this case the properties of the spin system will be the same when monitored by either the I or S spins.

The tilted rotating frame

If two rf fields B_{1I} and B_{1S} are applied to the spin system at frequencies ω_I and ω_S near the I- and S-spin resonance frequencies respectively, we can transform both systems into their tilted rotating frames, defined by the rotation operators

$$R(\omega_I, \omega_S, \Theta_I, \Theta_S) = \exp\{i(\Theta_I I_y^r + \Theta_S S_y^r)\} \exp\{it(\omega_I I_z + \omega_S S_z)\}. \qquad (2.27)$$

where Θ_I and Θ_S are the off resonance angles for the I- and S-spins respectively. The spin Hamiltonian is

$$\mathcal{H}_Z^\rho = \mathcal{H}_Z^\rho + \mathcal{H}_D^{\rho\,RL} = \mathcal{H}_{ZI}^\rho + \mathcal{H}_{ZS}^\rho + \mathcal{H}_{DII}^{\rho\,RL} + \mathcal{H}_{DIS}^{\rho\,RL} + \mathcal{H}_{DSS}^{\rho\,RL} \tag{2.28}$$

where all explicitly time-dependent terms have been excluded. The total time-independent dipolar Hamiltonian in the TR frame is derived only from the secular contributions in the laboratory frame. As in the laboratory frame, we can separate each of the dipolar Hamiltonians into secular and non-secular terms and identify four thermal mixing processes in addition to cross relaxation as mechanisms of temperature equilibration. The Hartmann-Hahn matching condition corresponds to the fastest cross relaxation rate, and occurs when the energy levels of I and S spins in the TR frame are equal. The magnitudes of the I- and S-spin Zeeman fields are now independent of each other.

The total dipolar local field in the TR frame is

$$B_{L\rho}^2 = \frac{Tr\{(\mathcal{H}_D^{\rho\,RL})^2\}}{\hbar^2\{\gamma_I^2 Tr(I_{z\rho}^2) + \gamma_S^2 Tr(S_{z\rho}^2)\}} \tag{2.29}$$

$$= (B_{LII}^\rho)^2 + (B_{LSS}^\rho)^2 + (B_{LIS}^\rho)^2 \tag{2.30}$$

If the intensity of both applied rf fields is large, the thermal mixing and cross relaxation processes will be slow and the I- and S-spin Zeeman and secular dipolar reservoirs will be decoupled and can all have different temperatures. However if the relative amplitudes of the two large rf fields are adjusted so that their Zeeman energy splitting in the TR frame are equal, cross relaxation will be fast while the thermal mixing processes are slow. If one of the B_1 fields is reduced to a value comparable to the local field, the Zeeman and dipolar reservoirs of that spin system may be able to attain a common spin temperature as well. If both B_1 fields are small, the thermal mixing and cross relaxation processes may bring the entire spin system into quasi-equilibrium at a common spin-temperature. The actual rate of thermal mixing

and cross relaxation at the low field strength will determine whether a common spin temperature is achieved before significant spin-lattice relaxation takes place.

In the following description, it is assumed that the applied rf fields are large compared to the secular local fields. If this is not true, the pure Zeeman order described will actually represent a combination of Zeeman and dipolar order. Also, the I–S coupling is considered small compared to the I–I coupling.

2.5 The ADRF experiment

The ADRF-CP experiment consists of the following steps, and is shown in figure 2-3.

1. Apply a $\pi/2$ pulse to the I spins (protons) and spin-lock them. This establishes an I-spin Zeeman temperature given by

$$\theta_{ZI}^{\rho} = \theta_L \frac{B_{1I}}{B_0} \tag{2.31}$$

   where θ_L is the lattice temperature, B_0 is the external magnetic field, and B_{1I} is the spin-lock field.

2. Adiabatically demagnetize the spin-lock field to produce a state of high dipolar order in the I spins. The I-spin dipolar temperature becomes

$$\theta_{DI}^{\rho} = \theta_L \frac{B_{LII}^{\rho}}{B_0}. \tag{2.32}$$

   At this point the temperature of the proton dipolar reservoir is significantly less than that of the S-spin (phosphorus) Zeeman reservoir.

3. Turn on an S-spin rf field, and observe the polarization of the S spins. When the S-spin rf field is turned on, the proton dipolar reservoir and the phosphorus Zeeman reservoir are brought into Hartmann-Hahn contact with each other, so that their temperatures begin to equilibrate. This results in a cooling of the phosphorus reservoir and the consequent development of a polarization of the ^{31}P spins.

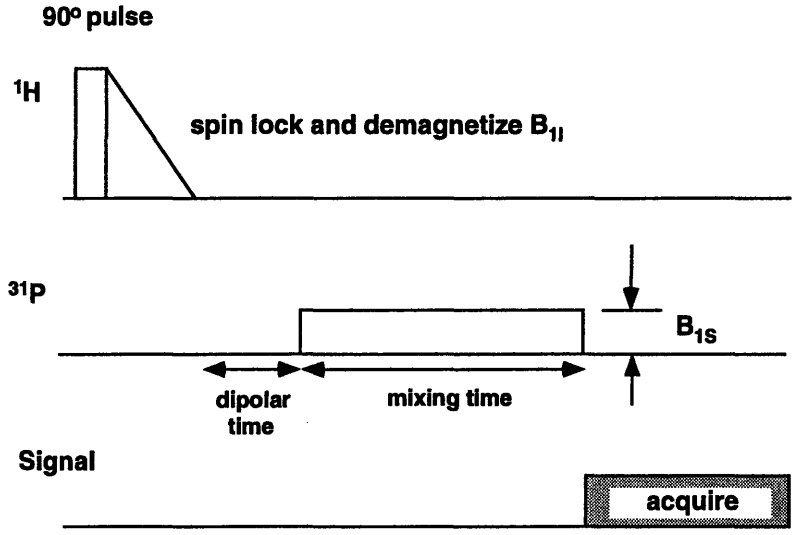

Figure 2-3: Pulse sequence for the ADRF cross polarization experiment

If the Zeeman energy of the S-spin RF is Hartmann-Hahn matched to the I-spin dipolar energy, the two reservoirs can exchange energy, and there will be a transfer of polarization from the dipolar reservoir of the I spins to the Zeeman reservoir of the S spins:

$$Tr\{(\mathcal{H}_{DII}^{\rho\,RL})^2\} = Tr\{(\mathcal{H}_{ZS}^{\rho})^2\}, \tag{2.33}$$

$$\omega_{LII}^{\rho} = \omega_{eS} \tag{2.34}$$

where $\omega_{LII}^{\rho} = \gamma_I B_{LII}^{\rho}$. In the absence of spin lattice relaxation, the rate of change of the I- and S-spin TR temperatures is described by the following set of coupled differential equations [96].

$$\begin{aligned} \frac{d}{dt}\left(\frac{1}{\theta_S^{\rho}}\right) &= -\frac{1}{T_{IS}}\left(\frac{1}{\theta_S^{\rho}} - \frac{1}{\theta_I^{\rho}}\right) \\ \frac{d}{dt}\left(\frac{1}{\theta_I^{\rho}}\right) &= -\frac{\epsilon\alpha^2}{T_{IS}}\left(\frac{1}{\theta_I^{\rho}} - \frac{1}{\theta_S^{\rho}}\right) \end{aligned} \tag{2.35}$$

where

$$\alpha = \frac{\omega_{eS}}{\omega_{LI}} \quad \epsilon = \frac{N_S S(S+1)}{N_I I(I+1)}. \tag{2.36}$$

α is the Hartmann-Hahn mismatch parameter, equal to unity when the fields are matched, and $\epsilon\alpha^2$ is the ratio of the heat capacities of the two spins. The asymptotic magnetization achieved in the absence of spin-lattice relaxation is

$$\frac{M_{S\infty}}{M_{0S}} = \frac{\gamma_I}{\gamma_S} \frac{\alpha}{1+\epsilon\alpha^2}. \tag{2.37}$$

The maximum asymptotic magnetization occurs when $\alpha = \epsilon^{-1/2}$. For rare S-spins with $\epsilon \ll 1$, the Hartmann-Hahn match corresponds to a magnetization that is far from the maximum achievable. In the case of the calcium phosphates, $\epsilon \sim 1$ ($\epsilon = 3$ for hydroxyapatite), so that the maximum asymptotic magnetization occurs in the neighbourhood of a perfect Hartmann-Hahn match.

For the case of rare S spins, T_{IS} can be expressed as [96]

$$T_{IS}^{-1} = \sin^2\theta_S \, M_{IS}^2 \, J_z(\omega_{eS}) \tag{2.38}$$

where M_{IS}^2 is the second-moment of the I-S coupling Hamiltonian, and J_z is a spectral density function that describes the fluctuations of $\mathcal{H}_{DIS}^{\rho\,(n)RL}$, which is dominated by I spin flips in this case. Since $J_z(\omega)$ is a monotonically decreasing function of ω, it appears that the fastest cross polarization would occur at $B_{1S} = 0$. However, this corresponds to a value of $\alpha = 0$ which means that the asymptotic magnetization is also zero. Thus the maximum signal represents a trade-off between the magnitude of the asymptotic magnetization, the cross polarization time and the spin-lattice relaxation rate.

At short times after the application of the S-spin rf, there is a transient oscillatory exchange of magnetization between the I-spin dipolar reservoir and the S-spin Zeeman reservoir. These oscillations are produced by the modulation of the I-S dipolar coupling by the applied S-spin rf, and occur at the effective Larmor frequency ω_{eS} of the S-spins in the rotating frame. The decay of the oscillations is characterized by

the correlation time of the random fluctuations of $\mathcal{H}_{DIS}^{\rho\,(n)RL}$. A detailed theoretical analysis using a Mori memory function formalism has been made by Demco *et al.* [98]. The transient oscillations detected during spin-lock cross polarization are due to well-resolved dipolar couplings, and occur at the natural frequency of the I-S coupling [99, 100, 101].

Since the cross polarization occurs between the proton dipolar reservoir and the phosphorus Zeeman reservoir, only one rf field is on at a time. In addition, the S-spin rf field required to Hartmann-Hahn match the I-spin dipolar field is fairly small. Thus, the power deposition in the sample is significantly reduced as compared to traditional spin-lock cross polarization. This is an enormous advantage for *in vivo* application.

2.5.1 ADRF differential cross polarization

The differential cross polarization or inversion recovery cross polarization technique developed by Melchior [69] has been used to resolve overlapping spectra in heterogenous, multicomponent polymer systems. The technique discriminates between overlapping spectra on the basis of their cross polarization times and allows selective resonances to be nulled [71, 102]. A similar spectral technique based on differences in $T_{1\rho}$ between overlapping species has been proposed by Zumbulyadis [103].

Differential cross polarization is performed by inverting the temperature of one of the spin systems within a very short time, during the cross polarization process. The subsequent evolution of the spins towards a common spin temperature may cause the observed spins to go through zero. This zero-crossing time will be different for species with different cross polarization times T_{IS}.

In conventional spin-lock cross polarization this inversion is produced by shifting the phase of either the I or S spin RF by 180 degrees. If this is done rapidly, the "sudden approximation" of quantum mechanics applies, and the populations of the spin states do not change, but the spins that were parallel to the B_1 field in the TR frame will now be anti-parallel to the field, resulting in an instantaneous change in the spin temperature of that system from θ to $-\theta$. The existence of a negative

spin temperature is only possible due to the existence of an upper bound to the spin energy levels.

The symmetry between the I and S spin systems is broken in the case of ADRF cross polarization, as the I spins are aligned along their local dipolar fields and not along an external RF field. An rf pulse of angle α applied to the dipolar system of a sample containing a single spin species will result in a change in its energy given by [86]

$$E_{D\alpha} = E_D \left(1 - \frac{3}{2}\sin^2\alpha\right), \tag{2.39}$$

where E_D and $E_{D\alpha}$ are the energies of the dipolar system before and after the pulse. The most negative energy is thus produced by a $\pi/2$ pulse and results in a dipolar energy of $-E_D/2$. If θ is the temperature of the system before the pulse, the temperature after the pulse corresponds to a temperature -2θ. This represents a significant loss of polarization.

During the ADRF-CP experiment described in the previous section, the S-spin Zeeman and I-spin dipolar temperatures approach a common spin temperature θ^{ρ}_{com}. If the phase of the S-spin rf is shifted by 180 degrees, the S-spins will now be anti-parallel to the Zeeman field, and the S-spin temperature changed instantaneously from θ^{ρ}_S to $-\theta^{\rho}_S$. The pulse sequence for the ADRF differential cross polarization experiment is shown in figure 2-4. If the phase shift is performed after equilibration of the spins, the spin temperatures immediately after the shift are θ^{ρ}_{com} and $-\theta^{\rho}_{com}$. The value of θ^{ρ}_{com} depends on the initial temperatures of the two spins before thermal contact, and their relative heat capacities. Spin lattice relaxation during this process will increase the value of θ^{ρ}_{com}.

The rate at which the two spin systems again approach a common spin temperature is described by Equations (2.35). At short times after the phase of the rf is shifted, there is once again an oscillatory exchange of magnetization between the Zeeman and dipolar reservoirs as described in the previous section.

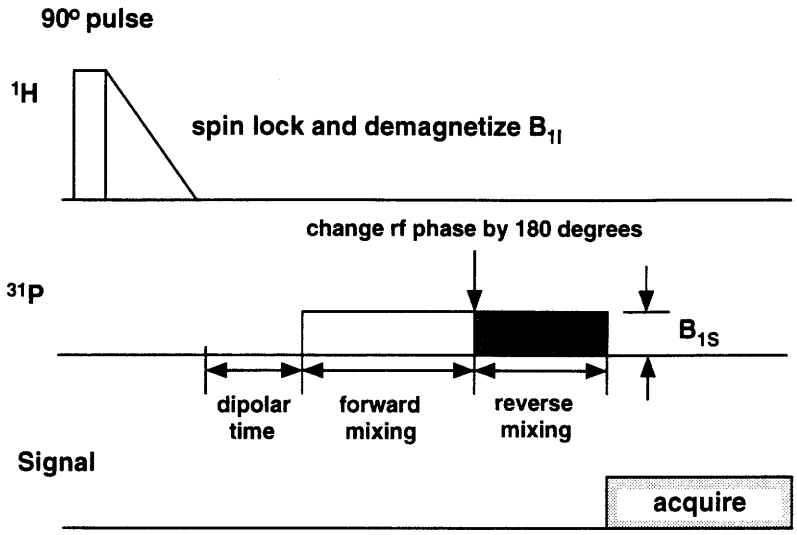

Figure 2-4: Pulse sequence for the ADRF differential cross polarization experiment.

Chapter 3

ADRF Cross Polarization

3.1 Application to bone mineral

Bone mineral contains large quantities of ^{31}P and ^{1}H nuclei, both of which are readily observable, so there may be little or no gain in sensitivity in the acquisition of a single ^{31}P FID by cross polarization from protons. However, we have measured the T_1 of ^{31}P in bone to be about 35–40 s at 4.7 T, while that of protons is less than one second. Hence cross polarization can significantly reduce the data acquisition time when collecting ^{31}P spectra. Of greater significance to the problem of detecting HPO_4^{2-} is that it may be possible to use ^{1}H–^{31}P cross polarization to selectively detect the HPO_4^{2-} and suppress the PO_4^{3-} in bone mineral. The spectra of these ions overlap, and it is essentially impossible to observe and quantify the small amount (~1–10%) of HPO_4^{2-} in the presence of an overwhelming amount of PO_4^{3-} in bone, without some form of spectral editing.

In the ADRF-CP experiment, the strength of the proton dipolar field is a property of the material being studied. It depends on the relative abundance of the protons as well as their spatial arrangement within the sample. Several classes of protons may exist with varying homonuclear dipolar coupling strengths to other protons. Thus the ^{31}P rf field required for efficient cross polarization is dependent on the material being studied, and may also depend on the particular S-spin resonance. If the HPO_4^{2-} and PO_4^{3-} ions have different local proton dipolar fields, they will cross polarize at different

^{31}P rf intensities. Thus, we might be able to selectively cross polarize the HPO_4^{2-} ions and detect them without detecting the PO_4^{3-} ions. In reality, cross polarization occurs over a range of values of the Hartmann-Hahn mismatch parameter α with varying degrees of efficiency, as discussed in the previous chapter. Thus it is not possible to entirely eliminate the PO_4^{3-} signal in this way. In addition, it is still uncertain whether the HPO_4^{2-} in bone mineral exists as individual ions scattered through the lattice or clustered within domains. The difference between the local fields of the PO_4^{3-} and the HPO_4^{2-} ions will be greater if the HPO_4^{2-} ions are clustered.

The HPO_4^{2-} groups have a shorter H-P distance compared to the H-P distance between PO_4^{3-} groups and neighbouring waters of crystallization or hydroxyl groups, and experience a significantly stronger internuclear dipolar interaction. Consequently, the monohydrogen phosphate ions cross polarize faster than the non-protonated phosphates, when the Hartmann-Hahn condition is satisfied. Thus, by manipulating the mixing time, we have a second variable that can be optimized for the detection of HPO_4^{2-}. The use of short contact time cross polarization to distinguish between the HPO_4^{2-} and PO_4^{3-} has been suggested previously [68].

3.2 Methods

3.2.1 Samples

We performed experiments on powdered samples of synthetic calcium phosphates as well as a specimen of porcine bone. The synthetic phosphates included hydroxyapatite (HA, $Ca_{10}(OH)_2(PO_4)_6$), and brushite (BRU, $CaHPO_4 \cdot 2H_2O$) (Aldrich Chemical Company Inc., Milwaukee, WI). While these two compounds have been used as representative models of the protonated and non-protonated phosphates in bone mineral, it is important to note that the actual phosphate moeities in bone mineral may be quite different from those in these synthetic compounds. Experiments were also performed on a mixture of the two containing 10% BRU and 90% HA in order to test the ability of the pulse sequence to detect small quantities of HPO_4^{2-} in a large PO_4^{3-}

background. The specimen of diaphyseal tibial porcine bone, obtained *abattoir*, was cleaned of external soft tissue, and the specimen was allowed to dry in air, retaining its complement of protein and lipid.

3.2.2 Experimental setup

The experiments were conducted with a two-port double resonance, transmit/receive ^{1}H–^{31}P 4.8 cm diameter single loop surface coil in an Omega CSI (formerly General Electric, now Bruker Instruments, Fremont, CA) NMR system equipped with an Oxford Instruments (Oxford, UK) 4.7 T 30 cm horizontal bore magnet. The probe has been described in detail elsewhere [68], and is a modification of the design proposed by Cross *et al.* [104]. The cylindrical samples were placed in the center of the coil to reduce the effect of the rf inhomogeneities in this first series of experiments. The proton and phosphorus transmitter frequencies were set on resonance for a sample of phosphoric acid. A linear ramp was used for the adiabatic demagnetization, and a 300 μs interval introduced before the phosphorus CP mixing pulse to allow any transients to die away. The experiment was repeated for different values of the mixing time, ranging from 5 μs to 5 ms, as well as a range of ^{31}P rf amplitudes. The recycle time TR, determined by the proton T_1, was set at 2 s. No rf decoupling of the protons was performed during signal acquisition, as this will not be possible *in vivo*. An eight-step phase cycle, with spin temperature alternation, was used to remove the nutation signal due to the ^{31}P rf, allowing observation of the true CP signal. The pulse sequence is shown in Figure 2-3, and the principal experimental parameters given in Table 3.1.

3.3 Results

Each FID was baseline corrected and apodized with a 750 Hz exponential before Fourier transformation. The amplitude and linewidth of each spectrum were then examined as a function of the mixing time using the peak analysis routines of NMR1 (formerly New Methods Research, now Tripos, St. Louis, MO). A 1.5 kHz wide

Table 3.1: Experimental conditions for ADRF-CP spectra

Number of acquisitions	
synthetic calcium phosphates	64
bone specimen	128
^{1}H 90 degree pulse	45–70 μs
Ramp time	50–80 μs
Recycle time	
synthetic calcium phosphates	2 s
bone	1.8 s
Single spectrum acquisition time	
synthetic calcium phosphates	2.25 min
bone specimen	4 min

isochromat centered on the peak was integrated to calculate the signal strength. The spectra obtained for each sample varied with the length of the mixing time as well as with the intensity of the ^{31}P rf applied.

3.3.1 Brushite

The ADRF-CP sequence was first tested with brushite, since the presence of HPO_4^{2-} groups ensures that the ^{1}H–^{31}P dipolar coupling is strong, and cross polarization will be efficient. Brushite peak heights are plotted as a function of mixing time and B_{1S} in Figure 3-1.

At the lowest B_1 field of 70 μT, no oscillations were observed, and the growth of the brushite signal resembled a growing saturation curve. As the magnitude of B_1 was increased, transient oscillations were observed soon after the rf was turned on. The frequency of the oscillations increased as the rf amplitude was increased. At longer times, the oscillations decay and the saturation curve representing the true CP signal can be observed. The maximum ^{31}P CP signal occured for a single value of the rf amplitude, and decreased when the rf amplitude was either increased or decreased from this value. This results from the trade-off between the magnitude of the asymptotic magnetization and the I-S cross polarization time T_{IS}, represented by the optimal value of the Hartmann-Hahn mismatch parameter $\alpha = \epsilon^{1/2}$ as discussed

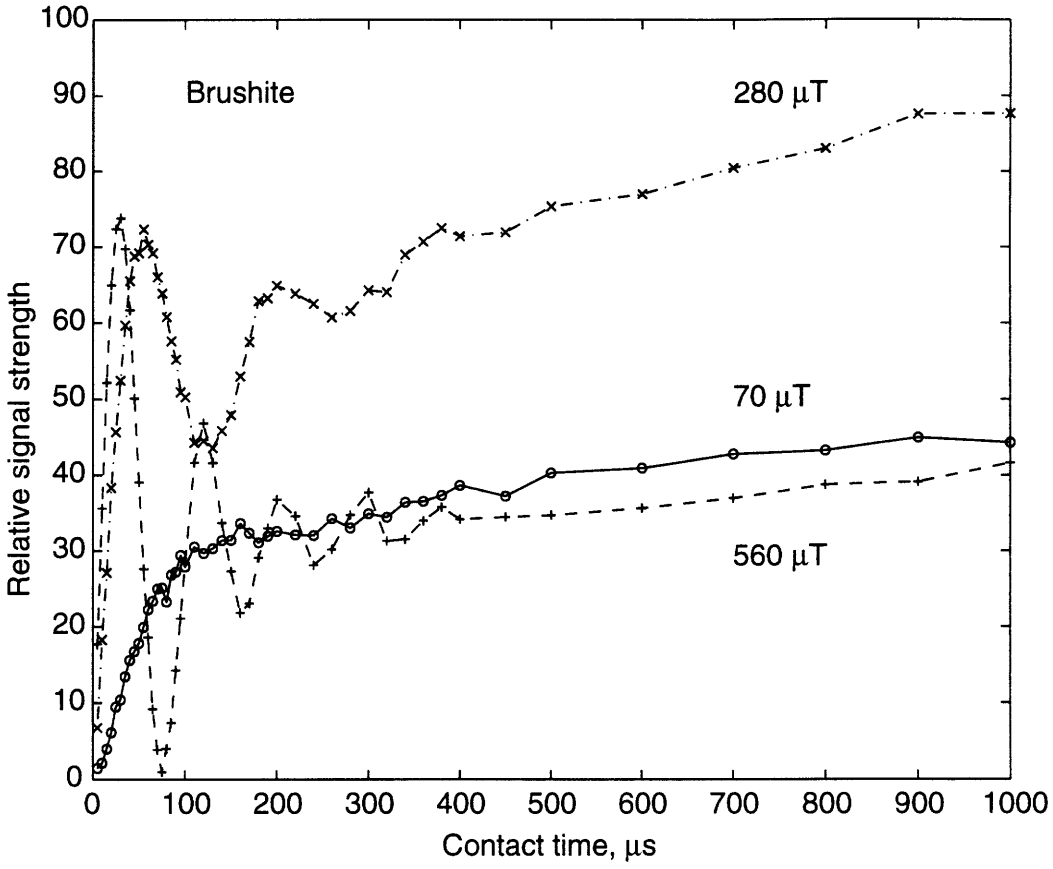

Figure 3-1: Peak height of the phosphorus spectrum of brushite plotted as a function of mixing time from 0 to 1 ms. Curves are shown for three phosphorus B_1 field strengths: 70 μT, 280 μT, and 560 μT. The most efficient cross polarization occurs at a field strength of 280 μT.

previously. For brushite, the optimal matching condition occured at a B_1 field of ~280 μT or ~4800 Hz. The signals did not change significantly between 1 and 5 ms.

3.3.2 Hydroxyapatite

The ^{31}P peak height of hydroxyapatite as a function of mixing time and rf amplitude is plotted in Figure 3-2. Once again it is possible to observe the transient oscillations after the rf is turned on, and the variation of the oscillation frequency with rf amplitude. In the case of hydroxyapatite, the most efficient cross polarization occured at a B_1 field of ~60 μT or ~1100 Hz, significantly smaller than that for brushite. The rate of cross polarization in hydroxyapatite was observed to be slower than that in brushite, with a much smaller final cross polarization signal. An important feature of the hydroxyapatite signal oscillation was the inversion of the phosphorus spectrum at short contact time. This was not observed in the brushite, as the growing cross polarization signal prevented an inversion.

3.3.3 Mixture of 10% brushite and 90% hydroxyapatite

The results from the mixture of HA and BRU were very similar to those of pure HA, except at those rf power levels where the BRU cross polarized strongly. The differences were particularly obvious when the oscillation passed through a null point, as can be seen in Figure 3-3. At these points the transient signal has been suppressed and the observed signal is derived purely from the cross polarization signal. Since the rf field is optimally matched to the local brushite field, the efficiency of cross polarization is high for brushite and low for hydroxyapatite. In addition, the stronger H–P coupling in brushite leads to a smaller T_{IS} and hence the brushite CP signal builds up faster. Thus the signal observed at these null points is largely a brushite signal, as can be seen in Figure 3-4.

At later times, the signal is a superposition of the hydroxyapatite and brushite lineshapes. While the brushite signal may be larger at these times, the hydroxyapatite signal has also increased and it is difficult to separate the two. Thus spectral selection

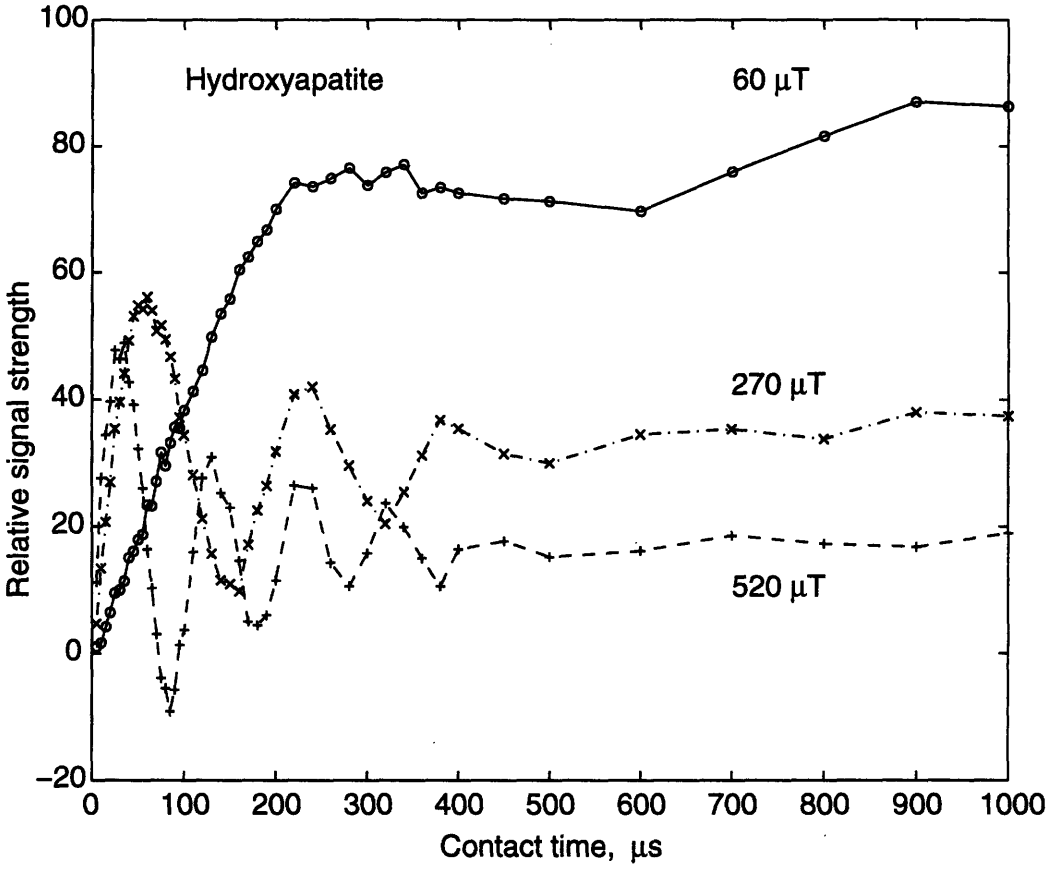

Figure 3-2: Peak height of the phosphorus spectrum of hydroxyapatite plotted as a function of mixing time from 0 to 1 ms. Curves are shown for three phosphorus B_1 field strengths: 60 μT, 270 μT, and 520 μT. The most efficient cross polarization occurs at a field strength of 60 μT. Note that the signal is inverted for some contact times when the Hartmann-Hahn condition is mismatched.

is achieved at the expense of low signal strength.

3.3.4 Porcine bone

The experiments on the specimen of porcine bone revealed that the oscillations persisted for much longer in the bone specimen as compared to the samples of synthetic calcium phosphates. The ^{31}P spectrum during the transient oscillations was observed to be very similar to that of hydroxyapatite. However, at certain rf power levels it was possible to isolate the presence of a broader phosphate peak, indicative of a protonated phosphate, when the oscillation was passing through a null point.

Figure 3-5 illustrates the oscillation of the narrower unprotonated phosphate peak in the presence of a growing cross polarization signal from the protonated phosphate, as the contact time is increased. The normal phosphorus spectrum of bone mineral and the spectrum of the protonated phosphate observed in the mineral are shown in Figure 3-6. This represents the first direct NMR observation of protonated phosphates in bone mineral under conditions compatible with *in vivo* application.

3.4 Discussion

3.4.1 Creation of dipolar order

The conditions for creating dipolar order in the proton spin system are different for brushite and hydroxyapatite and may also be so for the protonated and non-protonated phosphate ions in the mineral. As the magnitude of the local field decreases, it becomes increasingly difficult to satisfy the adiabatic condition, while ensuring that the demagnetization occurs on a time scale short compared to $T_{1\rho}$ and T_{1D}. Thus a relatively fast demagnetization will preserve the populations of those protons in strong local fields, while disturbing the populations of protons in weaker local fields, leading to a loss of order. No attempt was made to optimize the duration or shape of the demagnetization ramp for the detection of the monohydrogen phosphate. As the $\pi/2$ pulse used was not a true hard pulse, the efficiency of creation of

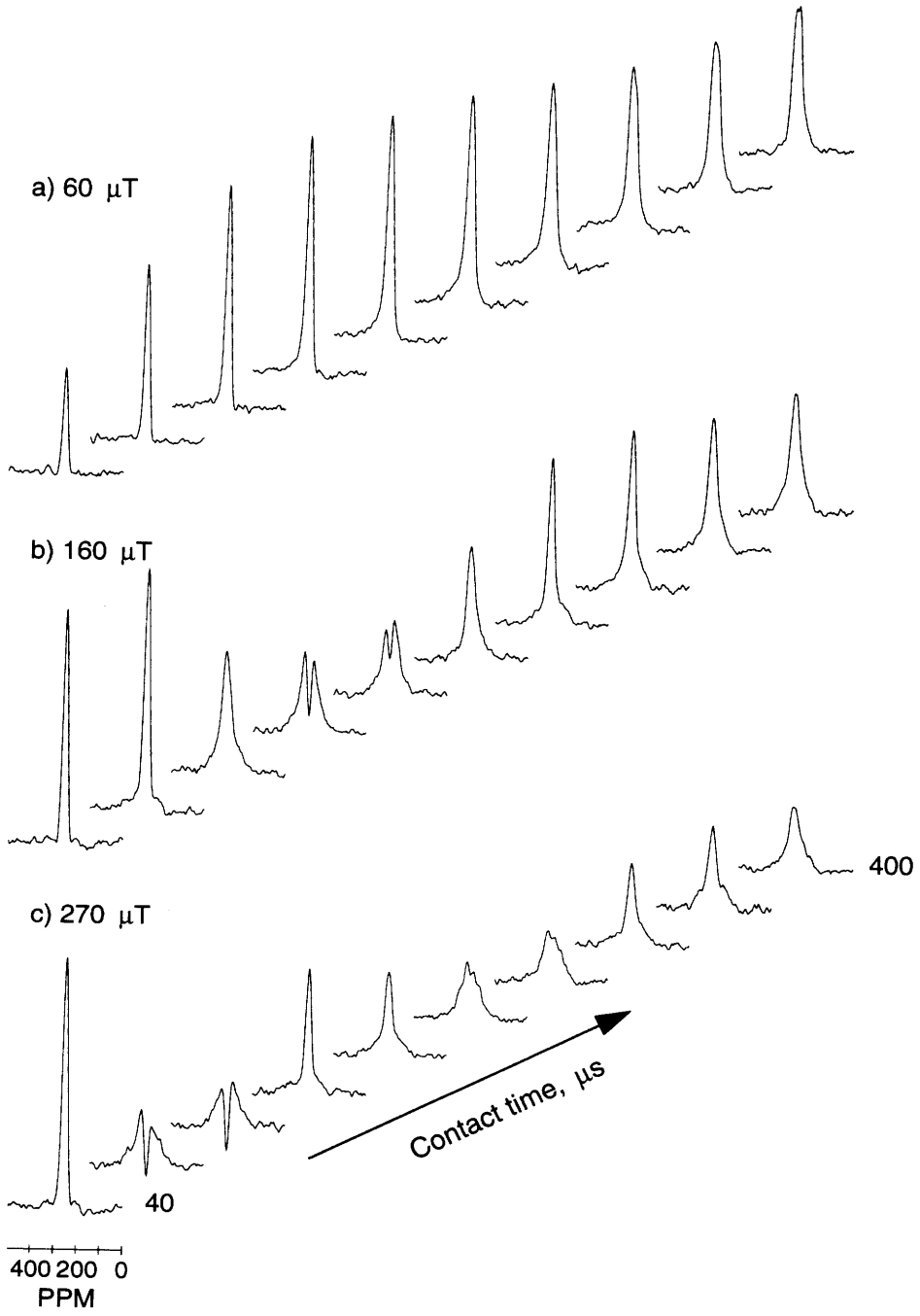

Figure 3-3: ADRF-CP spectra of a mixture of 90% hydroxyapatite and 10% brushite as a function of increasing contact time for three phosphorus B_1 field strengths: (a) 60 μT, (b) 160 μT, and (c) 270 μT. Each series shows the spectra obtained as the contact time was varied from 40 μs to 400 μs, in increments of 40 μs. Note the change in oscillation frequency with the magnitude of the B_1 field, and the observation of a broader peak as the oscillation passed through zero.

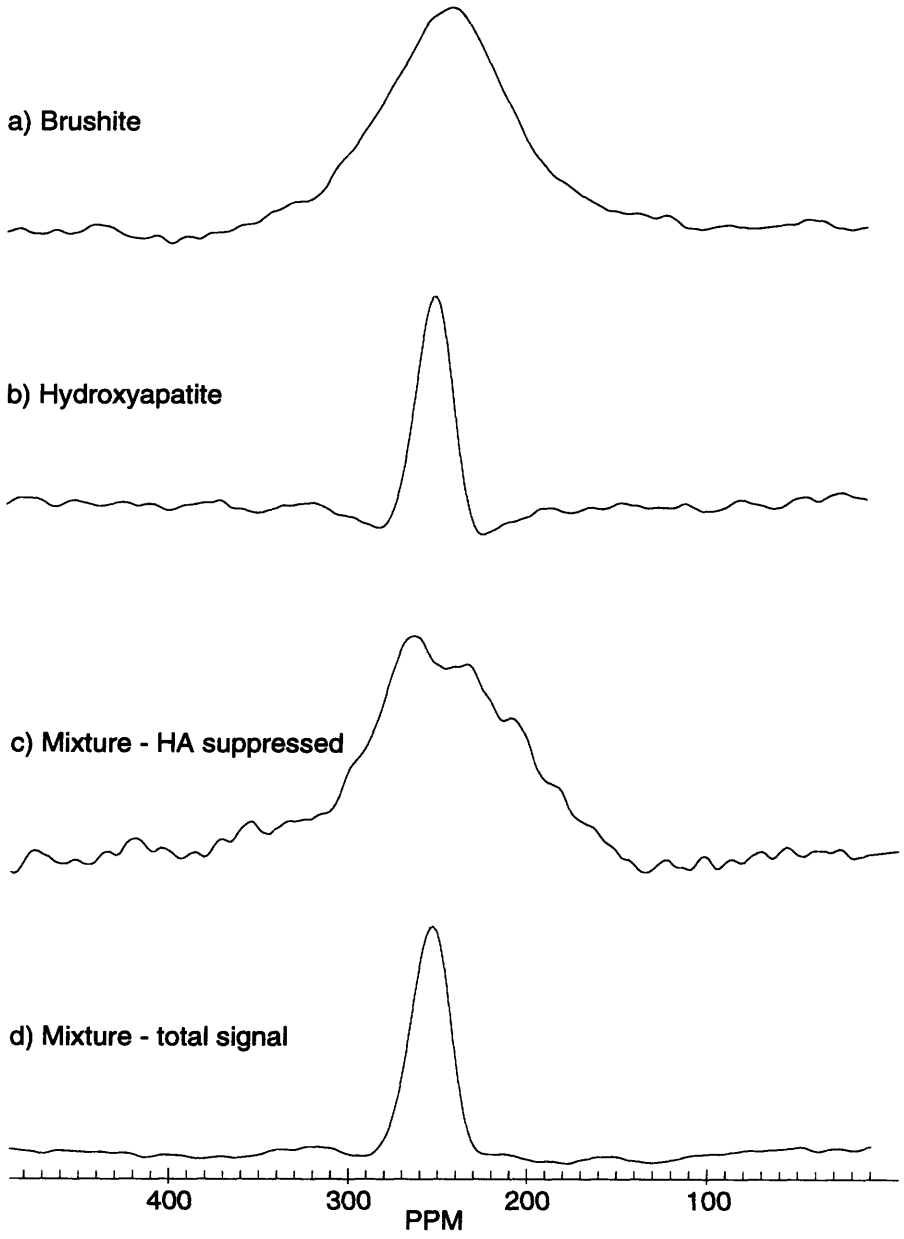

Figure 3-4: (a) ADRF-CP spectrum of brushite; (b) ADRF-CP spectrum of synthetic hydroxyapatite; (c) ADRF-CP spectrum of a mixture of 90% hydroxyapatite and 10% brushite with B_1 equal to 270 μT detected at a cross polarization time of 280 μs, as the oscillation passes through zero; and (d) ADRF-CP spectrum of the mixture with B_1 equal to 270 μT detected at a cross polarization time of 35 μs, when the entire phosphorus reservoir contributes to the signal.

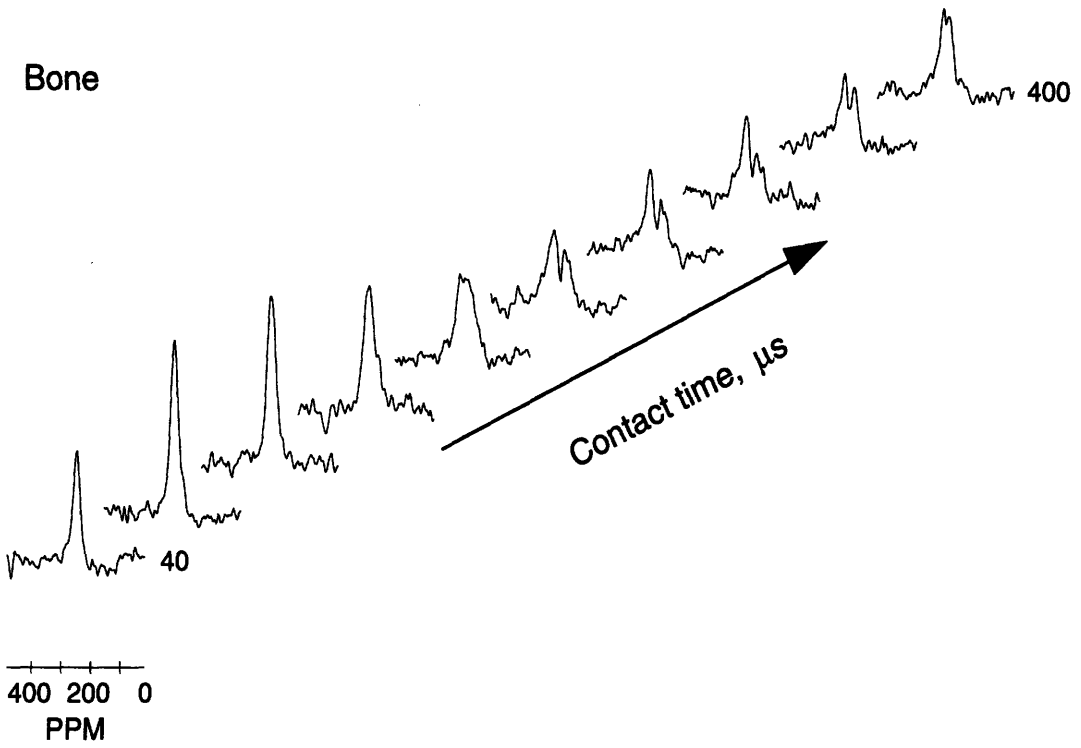

Figure 3-5: ADRF-CP spectra of a specimen of porcine bone as a function of increasing contact time, with B_1 equal to 110 μT. The figure show the spectra obtained as the contact time was varied from 40 μs to 400 μs, in increments of 40 μs. Note the oscillation of the narrow non-protonated peak, and the presence of the broader protonated peak.

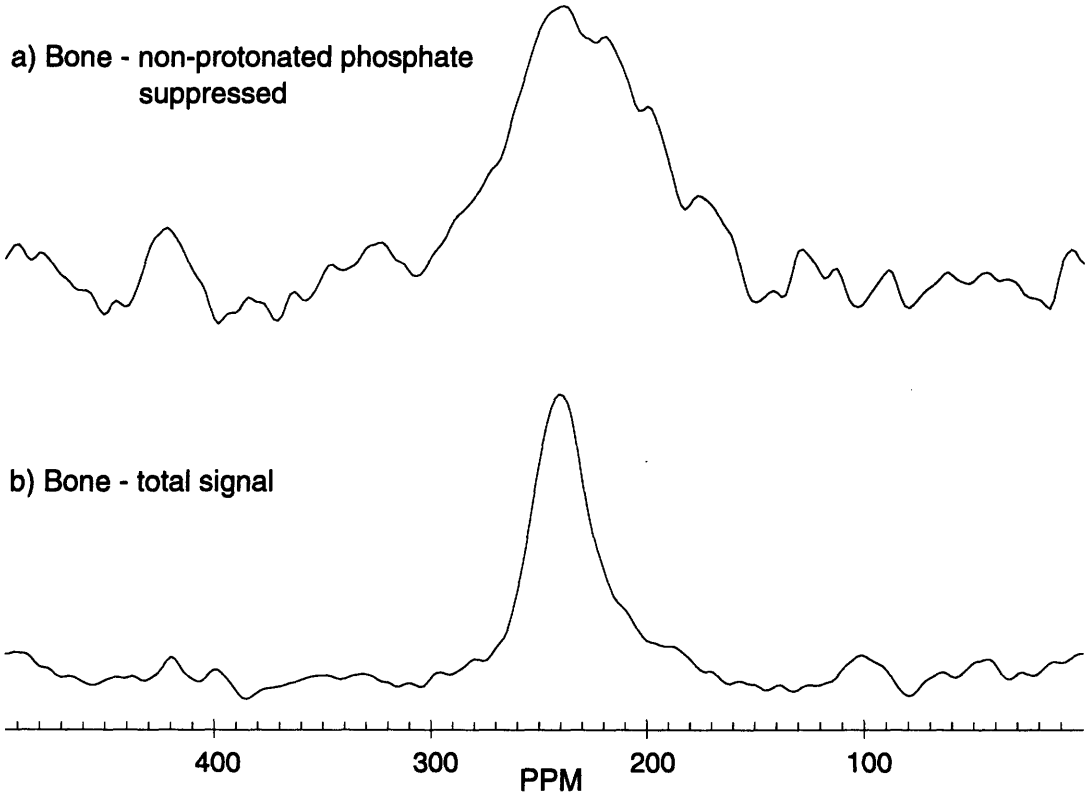

Figure 3-6: (a) ADRF-CP spectrum of a specimen of porcine bone with B_1 equal to 110 μT, detected at a cross polarization time of 200 μs, near a zero crossing of the oscillation; and (b) at a cross polarization time of 90 μs, when the signal is detected near a peak of the oscillation.

dipolar order in different proton species may vary.

3.4.2 Transient oscillations

The transient oscillations are observed to occur at a frequency ω_{eS}, the Larmor frequency of the S-spins in the rotating frame. The oscillations are expected to decay in a time τ characterizing the decay of the autocorrelation function of the I-spin dipolar fluctuations as seen by the S-spins [98]. The magnitude of the ^{31}P spectrum at the peak of the first oscillation was observed to be either the largest signal in the experiment, or very close to the maximum signal obtained after cross polarization. This is probably due to the fact that at short times after rf is turned on, the entire ^{31}P reservoir contributes coherently to the signal. It is therefore possible to obtain a relatively large CP signal in a time much shorter than T_{IS} by halting the I-S contact at the peak of the first transient oscillation. This has previously been suggested by Müller *et al.* for the transient oscillations observed in spin-lock CP due to resolved dipolar couplings [99]. Lineshape distortions were also observed during the oscillations. This distortion occurs because different isochromats (appearing at different frequencies in the spectrum) experience different local and effective rf fields, which strongly influences their dynamical behaviour.

Adiabatic Remagnetization

We briefly investigated the application of an adiabatic remagnetization (ARRF) of the phosphorus spins instead of the step application of the rf, to eliminate the transient oscillations. Figure 3-7 illustrates the results obtained for hydroxyapatite and brushite. A slow linear ramp remagnetization was used to turn on the ^{31}P rf after an ADRF of the protons.

It was possible to entirely eliminate the oscillations using the ARRF. The duration of the ramp required is around 2 ms in both cases, while magnitude of the observed signal was larger than that during the sudden application of the rf.

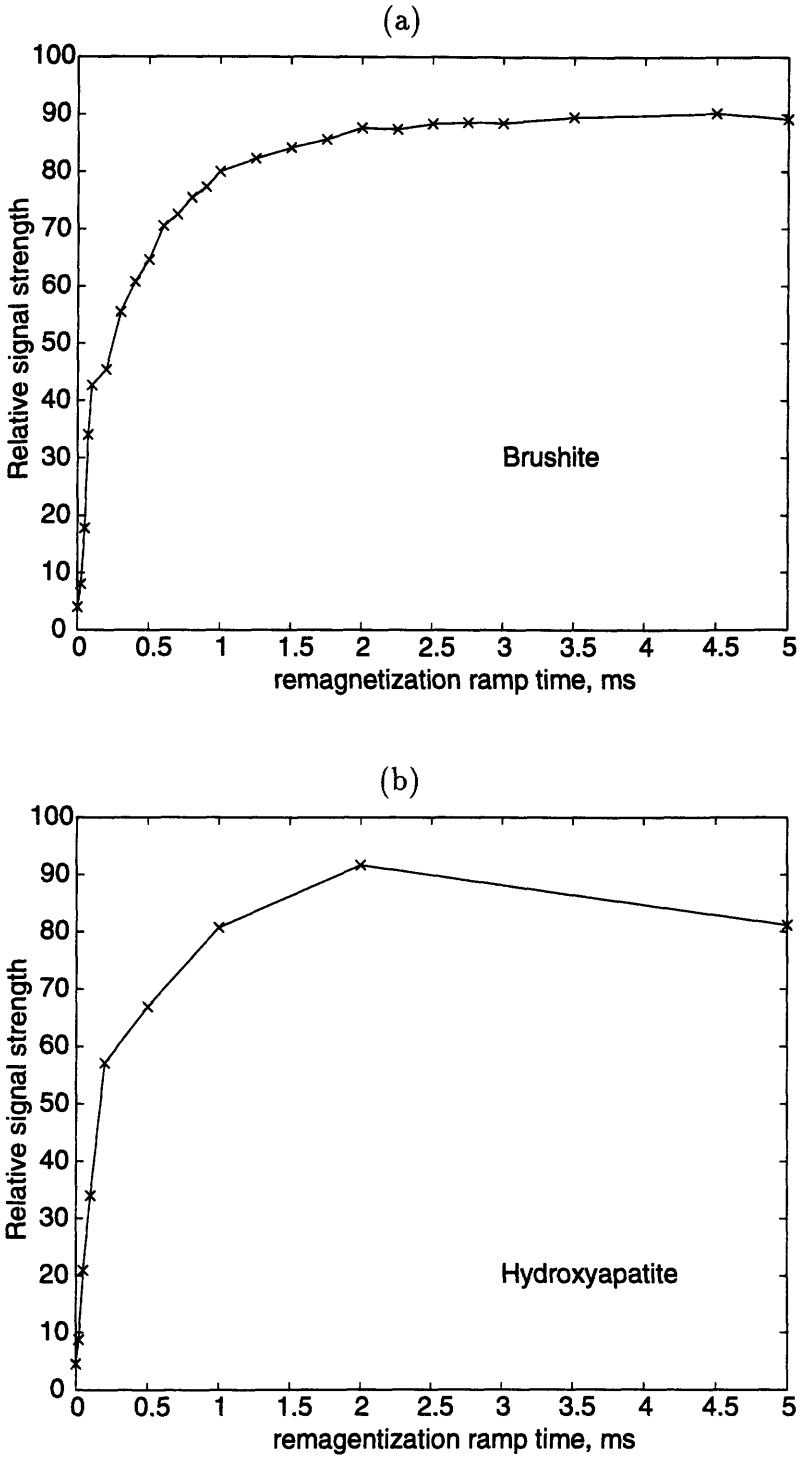

Figure 3-7: Adiabatic remagnetization of the phophorus spins in a sample of (a) brushite, and (b) hydroxyapatite, following an ADRF of the protons.

3.4.3 Cross polarization behaviour

The cross polarization behaviour depended strongly on the magnitude of the ^{31}P rf and thus the Hartmann-Hahn matching condition. The rate of cross polarization of the HPO_4^{2-} in brushite was seen to be significantly faster than in the PO_4^{3-} in hydroxyapatite when the optimal matching condition was satisfied. The strength of the H–P coupling determines the rate of the cross polarization, whereas the asymptotic value of M_S is determined by the initial temperature of the I-spin reservoir, the relative heat capacities of the I and S reservoirs, and the Hartmann-Hahn mismatch parameter, as shown in Equation (2.37). The presence of T_{1D} processes in the proton reservoir and $T_{1\rho}$ in the phosphorus reservoir can prevent the ^{31}P signal from reaching its asymptotic value, and eventually lead to the decay of the signal at longer times.

3.4.4 Detection of monohydrogen phosphate

The detection of HPO_4^{2-} groups in the presence of a large background of PO_4^{3-} has been a primary motivation of this study. This goal is advanced by the following three features of the ADRF-CP process that have been discussed above.

1. The signal exhibits transient oscillations of *a reasonably well-defined frequency* that pass through a null point, before inverting the spectrum.

2. The Hartmann-Hahn condition is dependent on the *chemical structure and environment of the spins*, i.e. the local proton dipolar fields, and not just the identity of the spin species.

3. The cross polarization rates of the two species, PO_4^{3-} and HPO_4^{2-}, that need to be discriminated are different.

The first step is to adjust the magnitude of the rf field to achieve an optimal Hartmann-Hahn match for the HPO_4^{2-} ions. If the local field of the PO_4^{3-} ions is different, these ions do not satisfy the conditions for cross polarization, and their cross polarization efficiency is reduced. The magnitude of the rf field also determines

the frequency of the oscillations, and hence the times at with the oscillation passes through zero.

We can then make use of the fact that the HPO_4^{2-} ions cross polarize much faster than the PO_4^{3-} ions and, by controlling the mixing time, to largely suppress the PO_4^{3-} ions and observe the HPO_4^{2-} ions. For example, we can observe the ^{31}P signal at one of the earlier null points of the oscillation. The signal observed will be due only to the cross polarized PO_4^{3-} and HPO_4^{2-} ions. However, since we are observing the signal after a relatively short time, the signal is almost entirely due to the HPO_4^{2-} ions. Observing the signal at short contact times does involve a sacrifice of signal to noise ratio, since we detect the signal before it grows to its maximum value. ADRF-CP represents the only feasible method of obtaining spectroscopic information on bone mineral *in vivo* at present.

Chapter 4

Creating Dipolar Order

4.1 Introduction

The strength of the signal obtained at the end of the cross polarization experiment depends directly on the degree of order in the dipolar reservoir. As noted during the discussion in the previous chapter, no attempt was made to optimize the demagnetization to create the greatest degree of dipolar order. The duration of the proton 90 degree pulse used was not short enough to be a true hard pulse for the samples being considered. This limit on the amplitude of the proton rf field also implied that the spin lock field was not much larger than the local fields, though the results of Slichter and Holton appear to indicate that this is not a significant problem. While our experiments were limited by the available power output of our amplifiers, increasing the magnitude of the applied spin-lock field will also increase the rf heating in lossy samples. Another concern is that the field inhomogeneities of the surface coil result in a variable flip angle across the field of view of the coil, and hence the efficiency of transfer of order between the Zeeman and dipolar reservoirs becomes spatially dependent.

We would ideally like to find a technique that is insensitive to the B_1 inhomogeneities of a surface coil, and does not require the application of large rf fields. We examined the efficiency of creation of dipolar order using three variants of the ADRF technique and the Jeener-Broekaert pulse sequence.

4.2 Methods

The techniques used in this chapter have all been suggested previously as discussed in Chapter 2. They include:

1. a hard 90 degree pulse followed by spin-locking with a strong RF field whose magnitude is adiabatically reduced to zero;

2. an adiabatic frequency sweep onto resonance with a strong RF field followed by spin-locking with a strong RF field that is again adiabatically turned off;

3. an adiabatic frequency sweep onto resonance with a weak RF field;

4. a two pulse Jeener-Broekaert sequence.

The samples used were powdered samples of synthetic hydroxyapatite and brushite.

4.2.1 Experimental setup

These experiments were also performed in the 4.7 T magnet described in the previous chapter. The probe used was a home-built, two-port, double resonance, cylindrical resonator tuned to ^{1}H and ^{31}P. The key experimental parameters are outlined in Table 4.1.

The proton 90 degree pulse was measured to be about 60 μs in the hydroxyapatite experiment and 50–55 μs in the brushite experiment. The adiabatic demagnetization in the first two methods was accomplished with a linear ramp from the maximum rf amplitude to zero. The length of the demagnetization ramp was varied from 10 μs to 5 ms. The adiabatic frequency sweeps were performed with a phase roll that resulted in an exponentially decaying frequency offset. The duration of the frequency sweep was varied from 500 μs to 10 ms, and two frequency offsets of 10 kHz and 100 kHz were used. The interpulse duration in the Jeener-Broekaert sequence was varied from 2 μs to 75 μs for hydroxyapatite and from 2 μs to 40 μs for brushite.

An eight-step phase cycle with spin temperature alternation was used in all cases except in the frequency sweep onto resonance with a small rf field. In that case a

Table 4.1: Experimental conditions for creation of dipolar order

Number of acquisitions	
hydroxyapatite	128
brushite	32
^{31}P remagnetization ramp time	
hydroxyapatite	3 ms
brushite	2 ms
constant ^{31}P rf duration	200 μs
recycle time	2 s
sweep width	
hydroxyapatite	40 kHz
brushite	60 kHz
dipolar time	500 ms

subtraction technique was used to eliminate the phosphorus nutation signal as spin temperature alternation was not possible.

Detection of dipolar order was performed with an adiabatic remagnetization of the phosphorus spins and is illustrated in Figure 4-1. A 3 ms linear ramp was used, followed by a 200 μs duration constant RF, before the phosphorus was detected. As the dipolar state is not in equilibrium immediately after a Jeener-Broekaert preparation, a 500 μs interval was introduced before detection. The same interval was introduced in all experiments so as to be able to compare signal amplitudes quantitatively. The use of a two-spin system simplified the detection of dipolar order, but is likely to complicate the thermodynamics as the spin systems may exchange energy in the demagnetized state.

4.3 Results

The data obtained were baseline corrected, apodized with a 750 Hz exponential, and Fourier transformed. After first order phasing, the area in a 3 kHz wide isochromat centered on the peak was used to calculate the the signal amplitude.

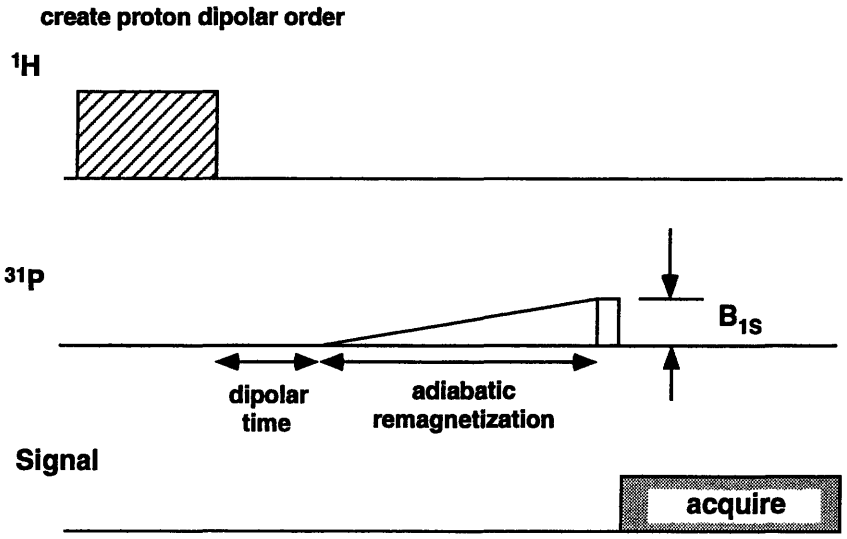

Figure 4-1: Detection of proton dipolar order using an ARRF of the phosphorus spins

4.3.1 Spin lock pulse and ramp demagnetization

This technique was used in all the experiments discussed in the previous chapter.

Hydroxyapatite

The effect of varying the duration of the demagnetization ramp is shown in Figures 4-2. The oscillation observed at short times is produced by an effective Jeener Broekaert pulse sequence. The peak occurs at a time approximately equal to that of a 90 degree pulse, which corresponds roughly to a 45 degree pulse, since we are using a linear ramp. At longer times a true adiabatic demagnetization is achieved, with the maximum signal obtained with a ramp time between 1 and 2 ms. For ramp times longer than 2 ms we can observe the effect of $T_{1\rho}/T_{1D}$ (or amplifier droop) which cause the signal to decay. The amplitude of the initial oscillation is about 66 % of the maximum signal obtained. The peak of the oscillation appears to be less sensitive to errors in the pulse angle.

Brushite

The effect of varying the initial flip angle and the duration of the demagnetization ramp is shown in Figures 4-3. The oscillation at short times is observed here as well. The peak of the oscillation corresponded to the greatest degree of dipolar order produced in brushite by any of the methods examined. While the exact reason for this is not known, we postulate a possible explanation in the discussion. As expected, it is observed that small angular offsets in the initial 90 degree pulse do not change the signal significantly.

4.3.2 Adiabatic frequency sweep and ramp demagentization

The use of a large rf field does not solve the power deposition problem, but the adiabatic frequency sweep onto resonance used to spin-lock the magnetism is insensitive to the amplitude of the applied rf field, and overcomes the problems introduced by the spatial inhomogeneity of the surface coil.

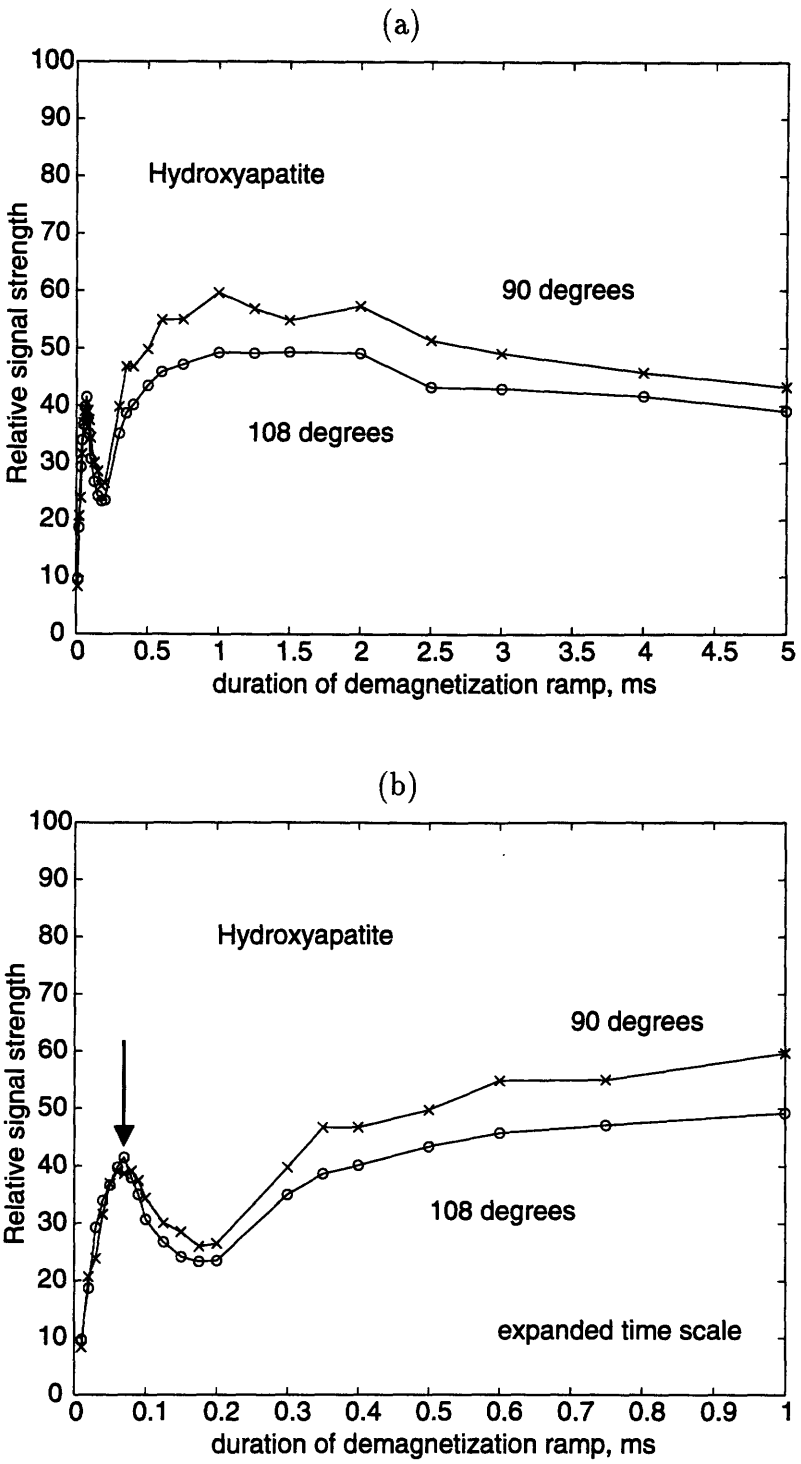

Figure 4-2: (a) The variation in signal strength due to changes in the length of the demagnetization ramp during the pulsed ADRF experiment in a sample of hydroxyapatite. The effect of a small angular deviation from a true 90 degree pulse is also shown. (b) Note the presence of the oscillation at early times. The peak of the oscillation (arrow) corresponds to the application of a Jeener-Broekaert sequence.

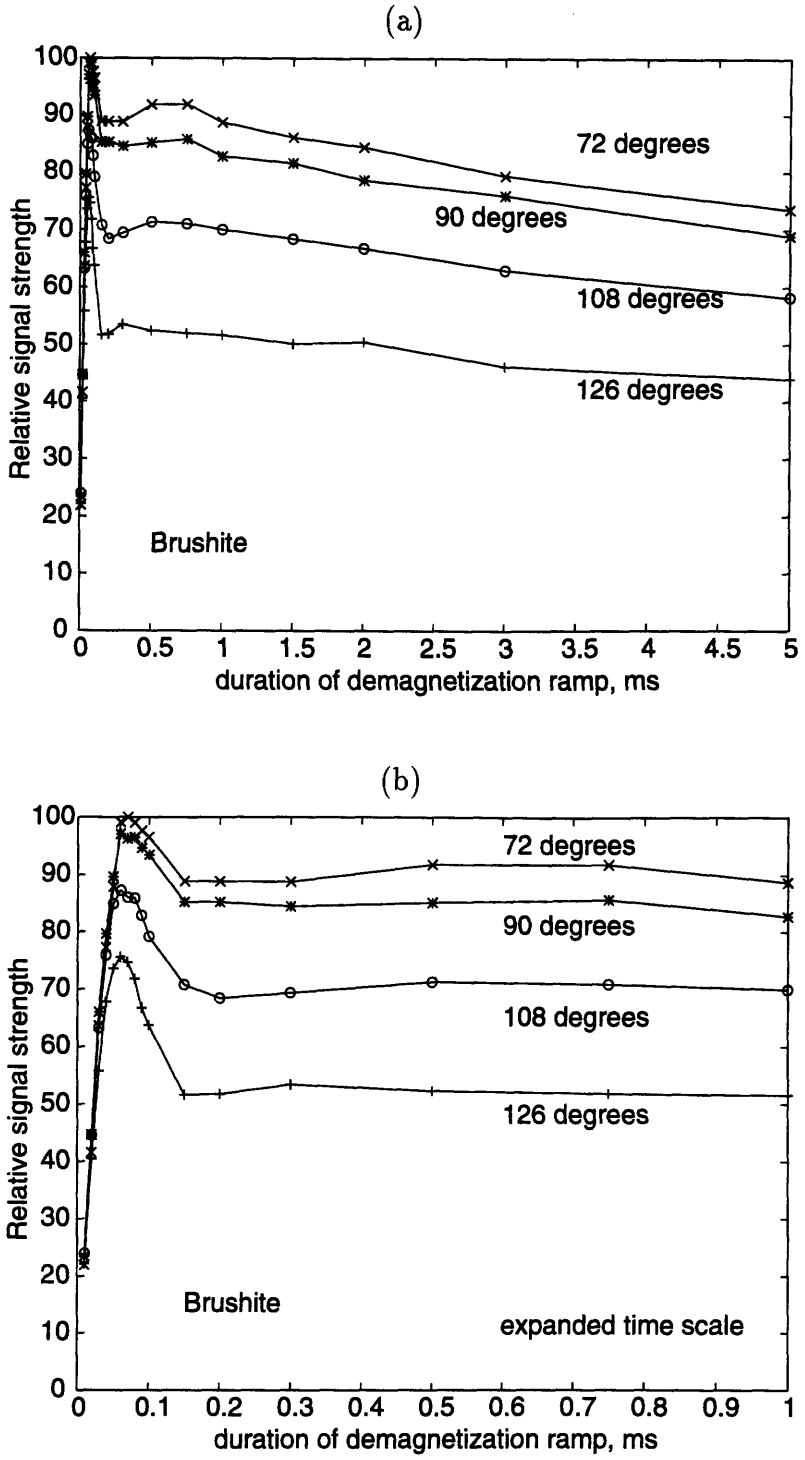

Figure 4-3: (a) The variation in signal strength due to changes in the length of the demagnetization ramp during the pulsed ADRF experiment in a sample of brushite. The figure also illustrates the effect of small angular deviations from a true 90 degree pulse. (b) The size of the initial oscillation is very large in brushite and represents the most efficient method of creating dipolar order in this system.

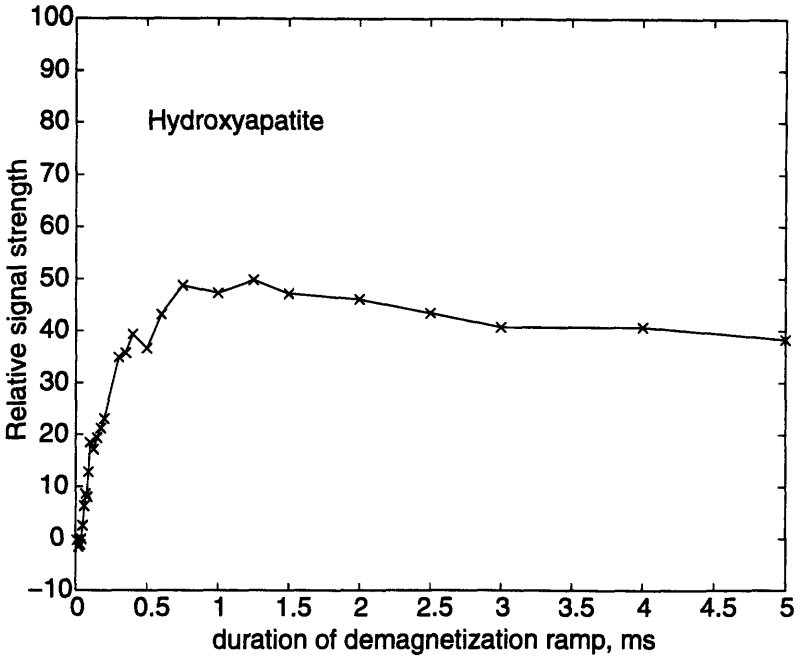

Figure 4-4: The effect of varying the duration of the demagnetization ramp after an adiabatic sweep onto resonance from a frequency offset of 10 kHz, with a strong rf field in a sample of hydroxyapatite. The initial oscillation is absent in this technique.

Hydroxyapatite

The optimal duration of the frequency sweep was found to be 1 ms from a frequency offset of 10 kHz, for this sample. The effect of varying the demagnetization ramp time, with this sweep time, is shown in Figure 4-4. Apart from the absence of the oscillation characteristic of the pulse method discussed above, the shape of the curve is essentially the same as that of Figure 4-2.

Brushite

The effects of varying both the duration of the frequency sweep onto resonance and the demagnetization ramp time are shown in Figure 4-5. The decrease in signal with increasing sweep times is largely due to the droop in the output of the amplifier at longer times. The shape of the curves is very similar to those of Figure 4-3 barring the initial oscillation.

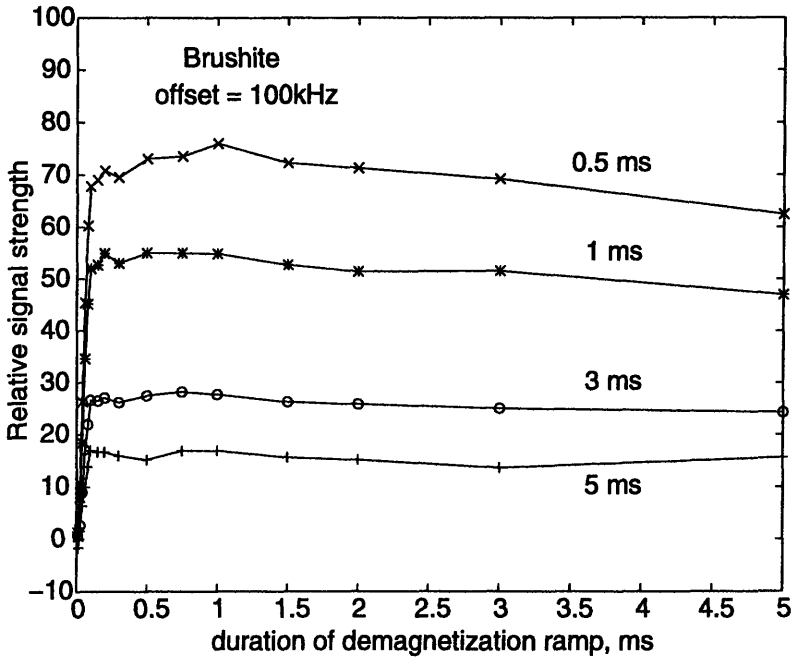

Figure 4-5: The effect of varying the duration of the demagnetization ramp after an adiabatic sweep onto resonance from a frequency offset of 100 kHz. The four curves were obtained by changing the duration of the frequency sweep. The loss of signal at long sweep times is primarily due to the droop in the output of the amplifier.

4.3.3 Adiabatic frequency sweep with a small rf field

If the amplitude of the rf field used is less than the local field, the spins will be aligned along their local fields at the end of the sweep onto resonance, and turning off the rf will not change the effective field significantly. This method should ideally help to overcome both the rf power deposition problem as well as the field inhomogeneities.

It was not possible to perform spin temperature alternation with this technique, so a baseline signal representing the ^{31}P nutation signal was obtained in each case with the proton RF turned off. This baseline was then subtracted before further data processing.

Hydroxyapatite

The length of the frequency sweep and the amplitude of the proton rf were varied as shown in Figure 4-6. The maximum signal was obtained using a proton rf field of $\approx 20\mu$T, and appeared to plateau at a sweep time of 5 ms. The increase in signal observed at long sweep times for the nominally higher powers is produced by the sag in the amplifier output at longer times, essentially producing a low power situation. It was observed that a frequency offset of 10 kHz resulted in a greater transfer of Zeeman to dipolar order than an offset of 100 kHz. This technique was optimal for the creation of dipolar order in hydroxyapatite.

Brushite

The effect of varying the duration of the frequency sweep and the rf amplitude are shown in Figure 4-7. The maximum signal was obtained with a proton rf field of $\approx 14\mu$T, and reached a plateau around 7.5 ms. The data shown corresponds to a frequency offset of 100 kHz only as no difference was found between the 10 kHz and 100 kHz offsets. It is possible that both offsets were too short for the study of brushite. The power droop in the amplifier at higher powers is also observed, and is a major drawback to finding the magnitude of the most efficient sweep field.

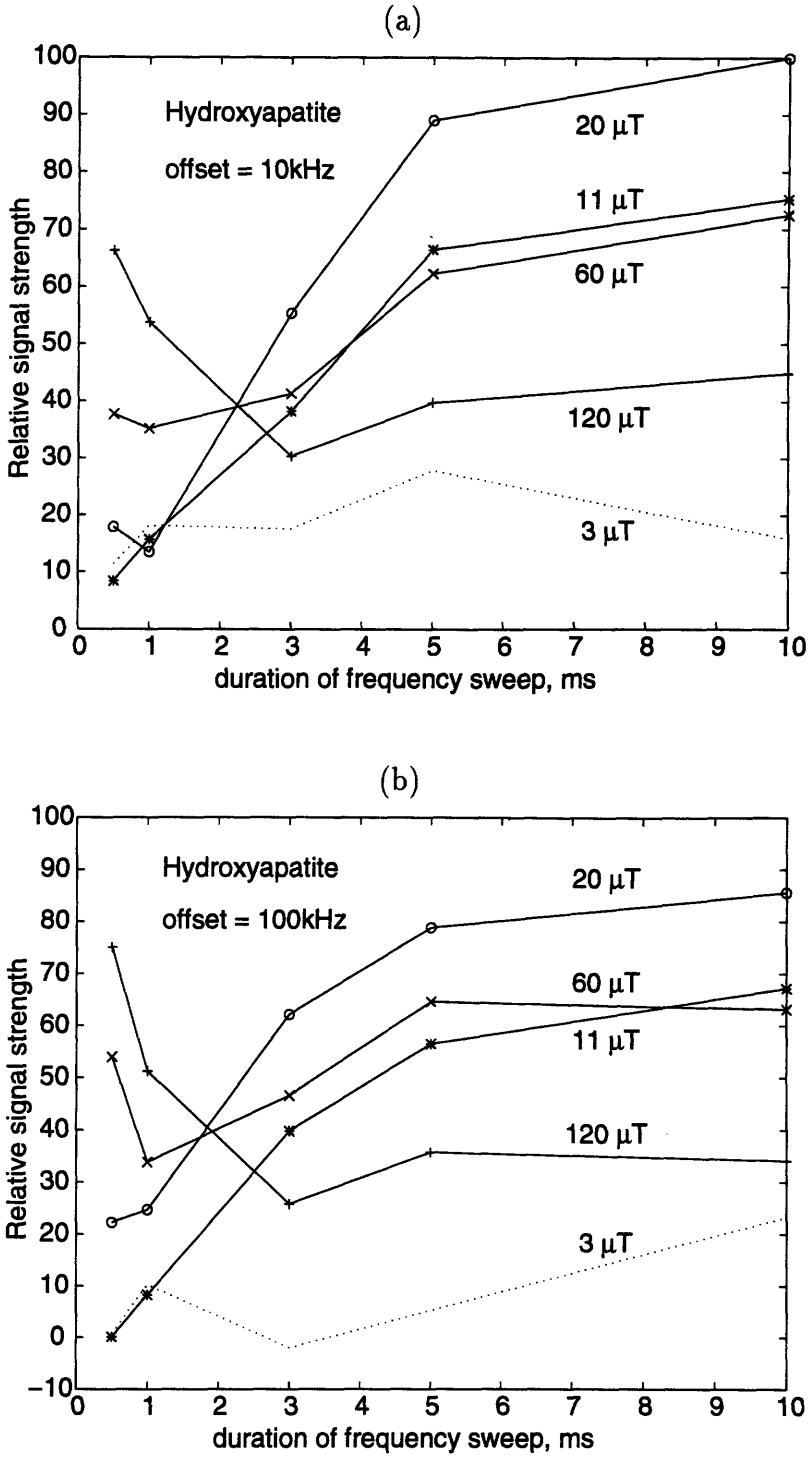

Figure 4-6: The effects of varying the duration of the frequency sweep and the amplitude of the rf are illustrated. The initial frequency offsets were a) 10 kHz and b) 100 kHz. The sweeps from an offset of 10 kHz were more efficient than those from 100 kHz.

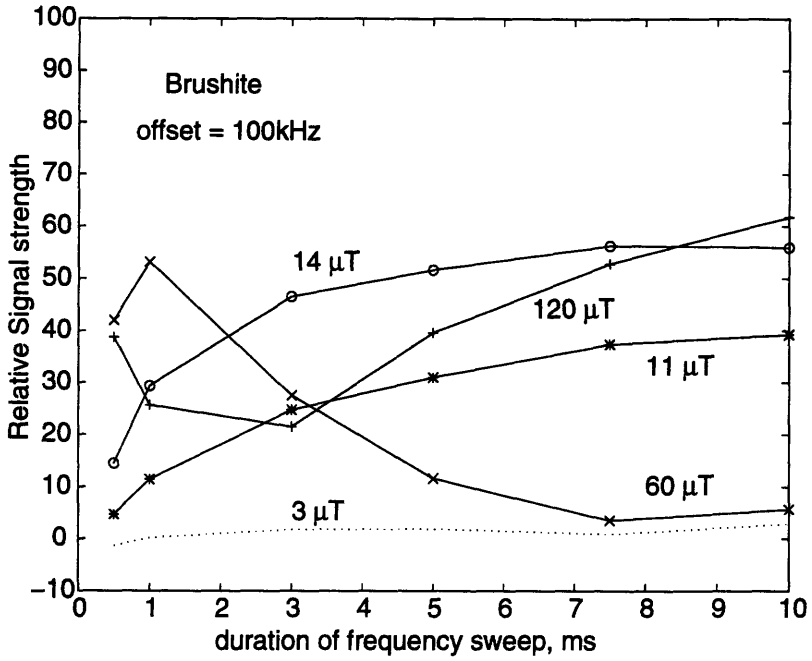

Figure 4-7: The effects of varying the duration of the frequency sweep and the amplitude of the rf are illustrated. The frequency offset used here is 100 kHz, though no difference was detected between the experiments performed with frequency offsets of 10 kHz and 100 kHz in brushite. The power droop in the amplifier can be observed at higher rf fields.

4.3.4 Jeener-Broekaert sequence

This technique represents the fastest method of producing dipolar order and is important in samples with short dipolar spin-lattice relaxation times T_{1D}. The lack of adiabaticity is compensated for by the absence of spin-lattice relaxation effects. While the length of the first pulse was varied, the length of the second pulse was always adjusted to be half the duration of the first. The signals obtained with this method were fairly close to the largest observed, even though the theoretical efficiency is only about 52 % of that of the ADRF techniques. The maximum signal should be attained when the second pulse is applied at the steepest portion of the fid.

Hydroxyapatite

The angle of the pulses and the inter-pulse duration were varied as shown in Figure 4-8. It is interesting to note that the maximum signal occured at different inter-pulse intervals for each length of the initial pulse used, indicating lineshape variations with pulse width. The largest signal was obtained when a 90–45 degree pulse combination was used with a very short inter-pulse duration of the order of 10 μs. The signal decays rapidly as the inter-pulse spacing is increased. The 40 μs pulse appears to be close to a hard pulse for hydroxyapatite.

Brushite

The effect of varying the pulse angle and the inter-pulse spacing is shown in Figure 4-9. Once again the maximum signal was obtained when a 90–45 pulse combination was used, in this case with a shorter inter-pulse duration of about 5 μs. None of the pulse durations used was hard in the brushite experiment, as can be seen from the steep slope of the curves in all cases. The signal again decays rapidly as the inter-pulse spacing is increased.

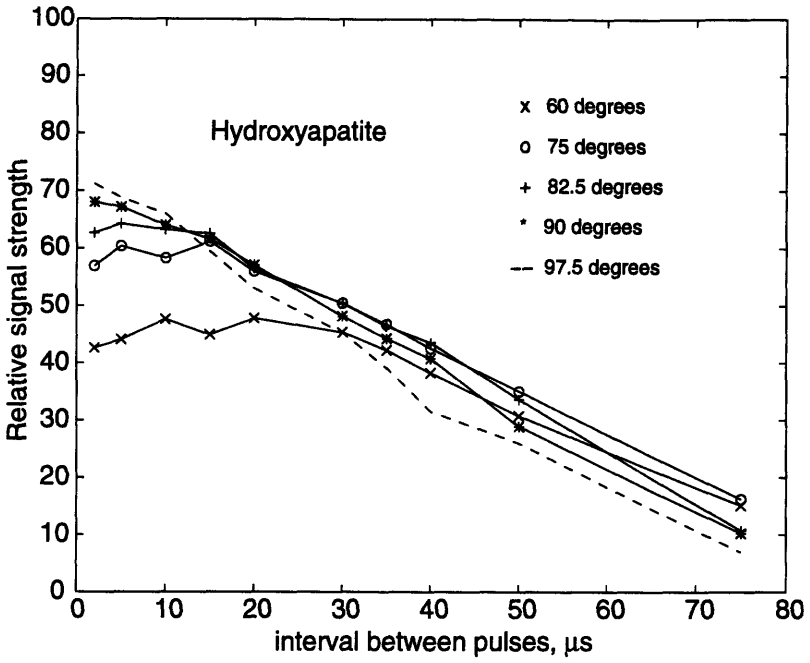

Figure 4-8: The variation in signal with pulse angle and inter-pulse spacing during the Jeener-Broekaert experiment in hydroxyapatite. The variation in the initial slope of the curves with rf flip angle is due to the finite width of the pulses applied.

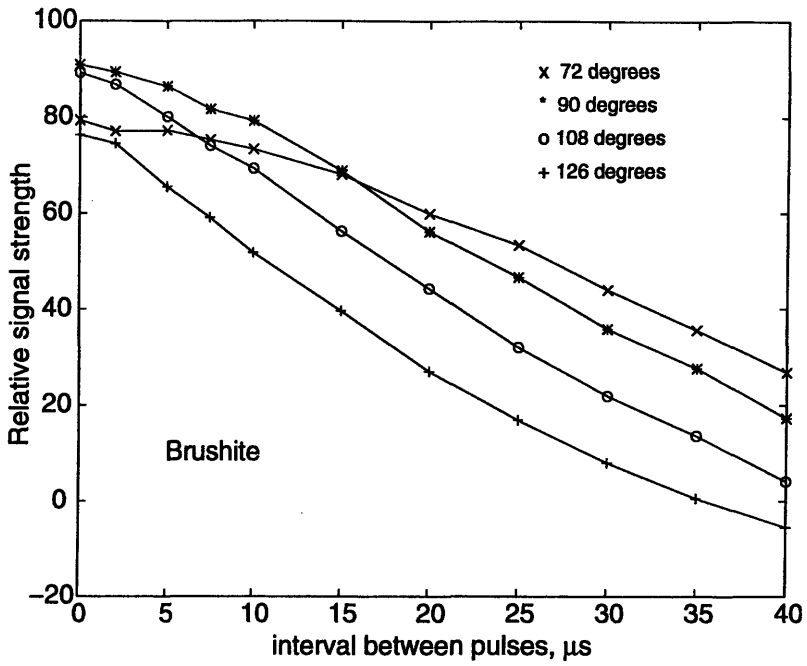

Figure 4-9: The variation in signal with pulse angle and inter-pulse spacing during the Jeener-Broekaert experiment in brushite.

4.4 Discussion

The relative signal strengths obtained in hydroxyapatite with each of the techniques are shown in Table 4.2. The adiabatic sweep onto resonance with a small RF field was significantly better than any of the other techniques. This advantage is likely to be magnified further when we perform the experiments on a surface coil as the adiabatic sweep onto resonance is insensitive to RF inhomogeneities, while the pulse

Table 4.2: Relative degree of dipolar order creation in hydroxyapatite

Method	*relative signal strength*
$\pi/2$ pulse - SL - demagnetize	60
sweep onto resonance with large B_1 - demagnetize	50
sweep onto resonance with small B_1	100
Jeener-Broekaert sequence	71

Table 4.3: Relative degree of dipolar order creation in brushite

Method	*relative signal strength*
$\pi/2$ pulse - SL - demagnetize (effective Jeener-Broekaert)	100
sweep onto resonance with large B_1 - demagnetize	76
sweep onto resonance with small B_1	56
Jeener-Broekaert sequence	91

methods are not. The ability to perform these experiments at low RF power levels improves our chances of applying them *in vivo*.

The results obtained with brushite are shown in Table 4.3. The 90 degree pulse followed by a demagnetization of the spin-lock field was the most efficient method here, though the maximum signal was obtained during the Jeener-Broekaert-like pulse. The frequency sweep methods did not fare as well in brushite, though their relative performance will probably improve in a surface coil. It is possible that an even shorter frequency sweep time might improve the efficiency for of the ramp demagnetization method. The two pulse Jeener-Broekaert sequence was still a fairly efficient technique of transferring order. The poor performance of the ADRF techniques is puzzling. It is possible that thermal mixing between the Zeeman and dipolar reservoirs is responsible, resulting in an increase in entropy.

The durations of our 90 degree pulses were too long for them to be considered hard pulses. The effect of this was mainly observed in the Jeener-Broekaert experiment. The observation that the maximum signal occured at different inter-pulse durations for different pulse lengths indicates that the shape of the fid was different in each case.

If the length of the frequency sweep or the demagnetization time starts to approach the dipolar spin-lattice relaxation time, the efficiency of the corresponding technique will be reduced. We have measured the T_{1D} of brushite to be 38 ms while that of hydroxyapatite was 13 ms. Thus this restriction is much more important in the case of hydroxyapatite than brushite. The frequency sweep followed by the ramp

demagnetization was the most susceptible to T_{1D} effects due to the length of time taken to produce the dipolar ordered state.

A number of clarifications are required in interpreting the comparative results shown above.

1. The ramp demagnetization is probably not the best shape for the adiabatic demagnetization. Physical considerations suggest that an exponential shape will be more efficient.

2. The nature of the frequency sweeps to resonance were also not investigated in detail. The shape, duration and offset of the sweep can probably be optimized further to improve the performance of these techniques.

3. The 45 degree pulse used for the second pulse in the Jeener-Broekaert sequence is no longer the most efficient in two spin systems, especially if the heteronuclear dipolar coupling is comparable to the homonuclear coupling.

4. The droop of the amplifier output for long pulses at the higher power levels prevented a proper evaluation of the sequences in these parameter ranges.

Further studies are required to investigate the dependencies in greater detail.

Chapter 5

ADRF differential cross polarization

5.1 Introduction

The problem of spectral selection in low resolution solid state spectroscopy still poses many interesting challenges. As the results in Chapter 3 indicate, it is possible to use differences in cross polarization time in combination with the zero crossings of the transient oscillation to achieve spectral selectivity. However, the low signal intensities that result are a significant obstacle if data acquisition time must be limited. In an effort to improve spectral selection and signal intensity, an ADRF-CP variant of the differential cross polarization (DCP) technique has been developed.

5.2 Methods

The experiments were conducted in the 4.7 T magnet described earlier. In the first experiment, a step rf pulse was applied to the ^{31}P spins following an ADRF of the protons, and the spins allowed to cross polarize. After a variable forward cross polarization time, the phase of the rf was shifted by 180 degrees to invert the temperature and reverse cross polarization initiated, as illustrated in Figure 2-4. Experiments were performed on powdered samples of synthetic brushite and hydroxyapatite, as well as

Table 5.1: Experimental conditions for surface coil ADRF-DCP spectra

number of acquisitions	
synthetic calcium phosphates	64
bone specimen	128
^{1}H 90 degree pulse	64 μs
demagnetization ramp time	80 μs
recycle time	
synthetic calcium phosphates	2 s
bone	1.7 s

a specimen of porcine bone, using a two-port double-resonance surface coil [68]. Each spectrum obtained represents a unique combination of forward and reverse cross polarization times. The principal experimental parameters are outlined in Table 5.1. During the study of the bone specimen, the magnitude of the B_1 field was also varied.

In the second experiment, an adiabatic remagnetization (ARRF) of the ^{31}P spins was performed to a constant rf field. After a short period of constant rf, the phase of the rf was shifted by 180 degrees and the reverse cross polarization of the spins studied. The pulse sequence is illustrated in Figure 5-1. This experiment was performed on samples of hydroxyapatite and brushite. The hydroxyapatite experiment was performed with the surface coil under the conditions outlined in Table 5.1. A 2 ms ^{31}P linear ramp was used to remagnetize the spins, after which the rf was held constant for 500 μs before the temperature inversion. The brushite experiment was performed with a cylindrical double-tuned resonator as the surface coil had been modified for other experiments. The length of the remagnetization ramp was 2.5 ms and the duration of the constant rf period before temperature inversion was 100 μs. The main experimental details of the brushite experiment are given in Table 5.2

The ordered dipolar state was created by applying a 90 degree pulse, spin locking the magnetization and linearly ramping the magnitude of the rf field to zero. Spin temperature alternation was used to remove the nutation signal.

Table 5.2: Experimental conditions for resonator ADRF-DCP spectra

number of acquisitions	16
^{1}H 90 degree pulse	50 μs
demagnetization ramp time	1 ms
recycle time	2 s

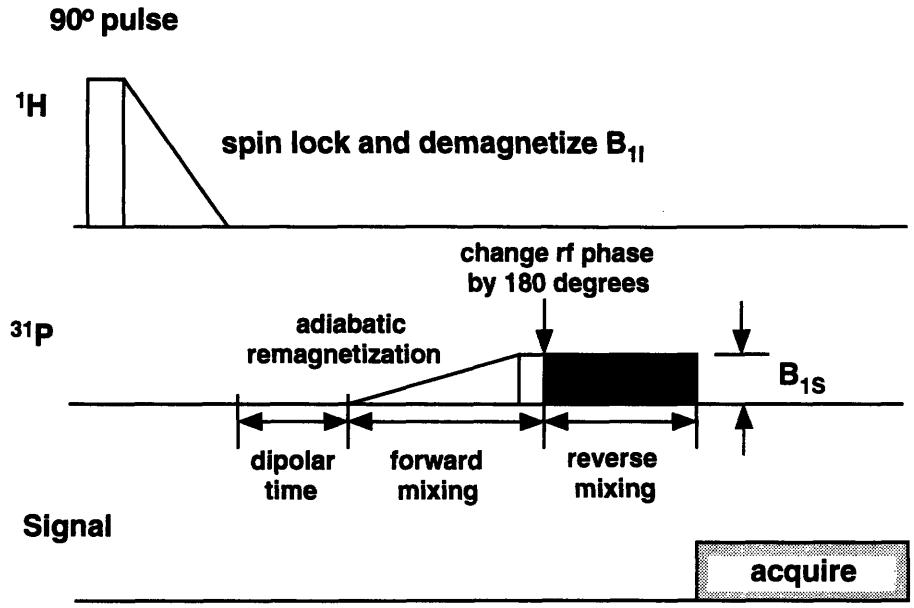

Figure 5-1: Pulse sequence for ADRF differential cross polarization following ARRF of the phosphorus

5.3 Results

Each FID was baseline corrected and apodized with a 750 Hz exponential before being Fourier transformed. An isochromat of spins 3 kHz wide and centered around the peak was integrated to calculate the signal intensity.

5.3.1 Brushite

In the first series of experiments with the step rf, a number of combinations of forward and reverse cross polarization times were used to study the dynamics of the spins under this pulse sequence. The results for brushite are shown in Figure 5-2. The usual forward cross polarization signal is shown extending out to a contact time of 5 ms. The figure also shows the effect of inverting the ^{31}P temperature at 20 μs, 60 μs, 150 μs, 750 μs and 2 ms after the rf is first turned on. It is observed that the inversion of the signal is stronger if the phase is shifted early in the cross polarization process, before the ^{31}P and ^{1}H can equilibrate completely. Transient oscillations were observed immediately following the temperature inversion in every experiment. When the temperature was inverted at 2 ms, the asymptotic value of the curve obtained was very close to zero, indicating that the ratio of the heat capacities of the ^{1}H and ^{31}P spins is close to unity.

5.3.2 Hydroxyapatite

The response of the hydroxyapatite spin system to the step rf experiment is illustrated in Figure 5-3. It shows the effect of inverting the temperature at 40 μs, 125 μs, 400 μs, 1 ms and 2 ms after the rf is first turned on. Once again the inversion of the signal is stronger if the phase is shifted early in the cross polarization process before equilibration proceeds very far. The signal was only observed to pass through zero if the phase was shifted during the early part of the transient oscillation. The slope of the oscillation immediately after the inversion of the phase is the negative of the slope just before the inversion. From the magnitude of the asymptotic signal after inversion, it appears that the heat capacity of the ^{31}P spins in hydroxyapatite

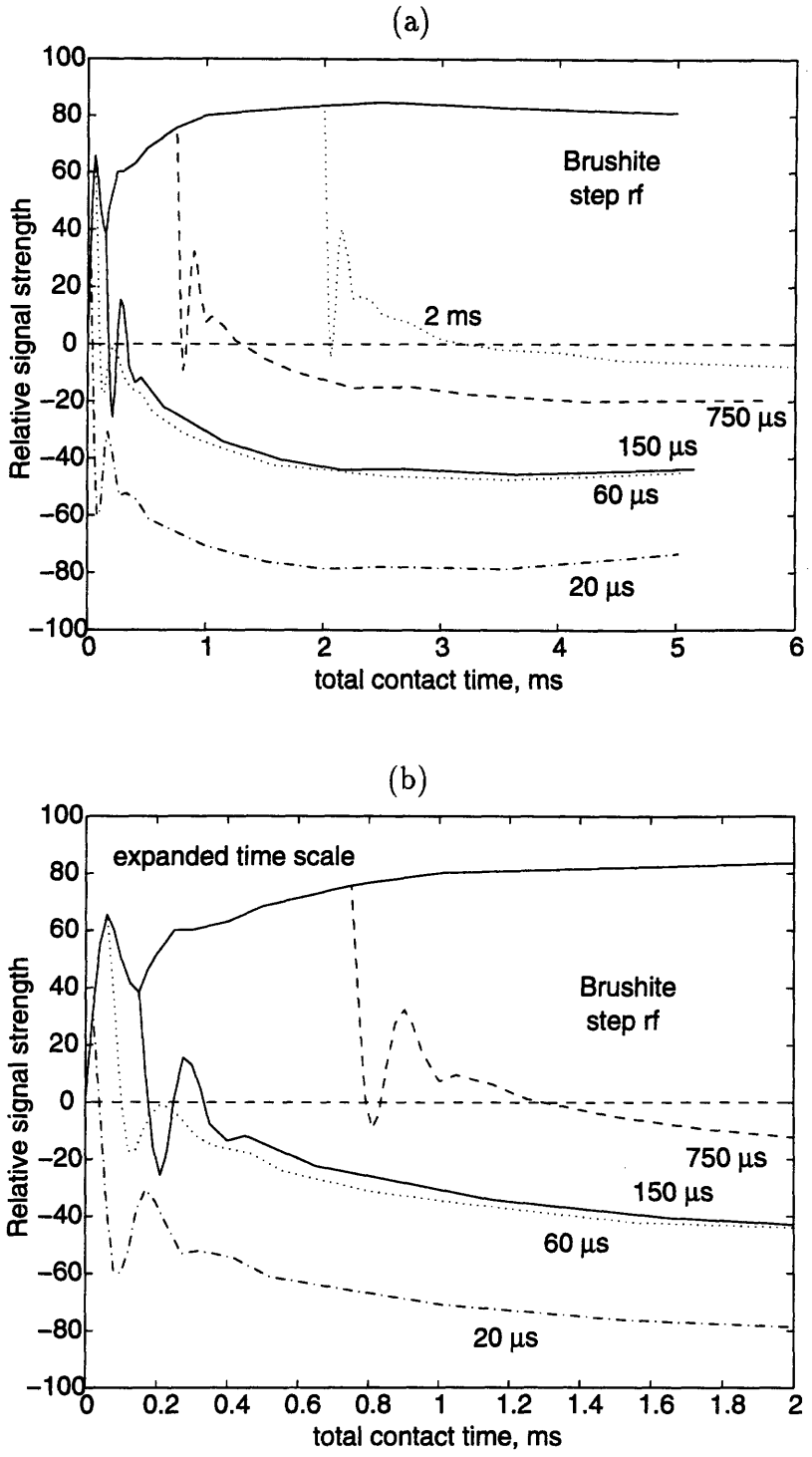

Figure 5-2: (a) The effect of inverting the ^{31}P phosphorus temperature at various times during the cross polarization process in a sample of brushite. The magnitude of the rf field is ≈ 200 μT. (b) The early part of the curve is expanded to show the effect of inverting the phase during the transient oscillation, before the system can be described by a temperature.

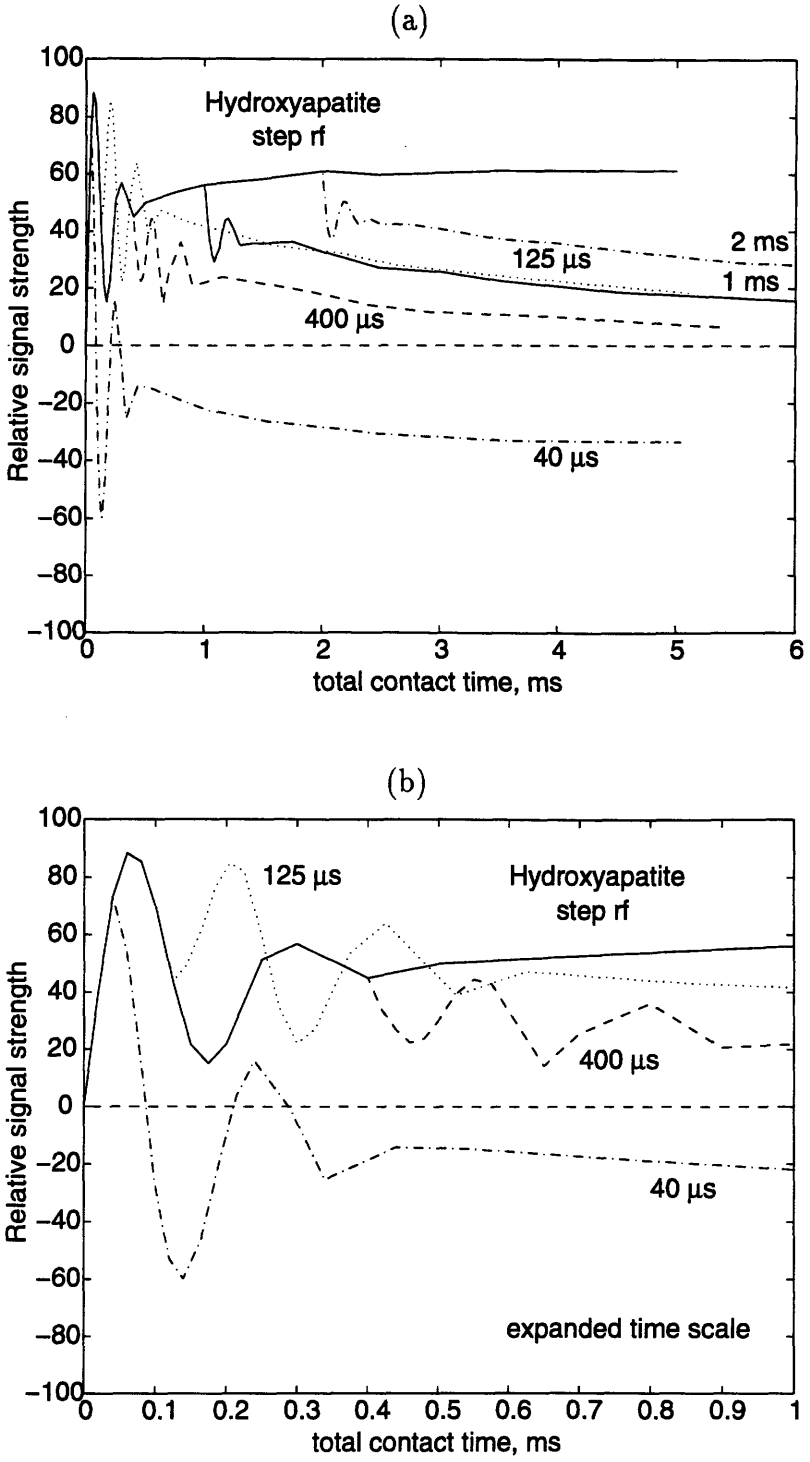

Figure 5-3: (a) The effect of inverting the ^{31}P phosphorus temperature at various times during the cross polarization process in a sample of hydroxyapatite. The magnitude of the rf field is ≈ 180 μT. (b) The early part of the curve is expanded to show the effect of inverting the phase during the transient oscillation, before the system can be described by a temperature.

is significantly larger than that of the ^{1}H.

5.3.3 Porcine bone

The response of the bone specimen to the step rf field is shown in Figure 5-4 for three different field intensities of 130 μT, 200 μT and 320 μT. The strongest cross polarization takes place at the lowest field. The response of the ^{31}P spins to the temperature inversion is also the greatest in the 130 μT field, indicating strong thermal contact between the two systems. We can observe the change in the heat capacity of the ^{31}P spins as the strength of the applied rf field is changed. At 320 μT there was a very small response to the phase change after the initial oscillation.

Figure 5-5 shows the series of spectra obtained when the phase is inverted 60 μs after the rf is turned on. There is a strong oscillation before the asymptotic signal can be observed. Note the change in shape of the spectra at 1 ms, 2.5 ms and 5 ms. The linewidths obtained from a Gaussian curve fit to the spectra at these times are 4450 Hz, 3400 Hz and 3000 Hz respectively. The broad spectrum at a 1 ms reverse cross polarization time is indicative of the presence of HPO_4^{2-} groups in the bone. Figure 5-6 allows direct comparison of the spectra just before the phase shift (lw = 2300 Hz) and after 1 ms of reverse cross polarization (lw = 4450 Hz).

5.3.4 Phosphorus rf field strength

In this second series of experiments a linear ramp remagnetization was performed on the phosphorus spins to different maximum rf field strengths. After a brief interval during which the rf was kept constant, the rf phase was shifted by 180 degrees while the magnitude was kept fixed.

The results obtained with brushite are shown in Figure 5-7 for two values of B_1, 100 μT and 300 μT. Only 16 acquisitions were averaged per spectrum due to time constraints. It can be seen that while the magnetizations at the end of the remagnetization ramp are very similar (60% for 100 μT and 67% for 300 μT), the two cases diverge after the temperature inversion. In the case of the 300 μT field, it

(a)

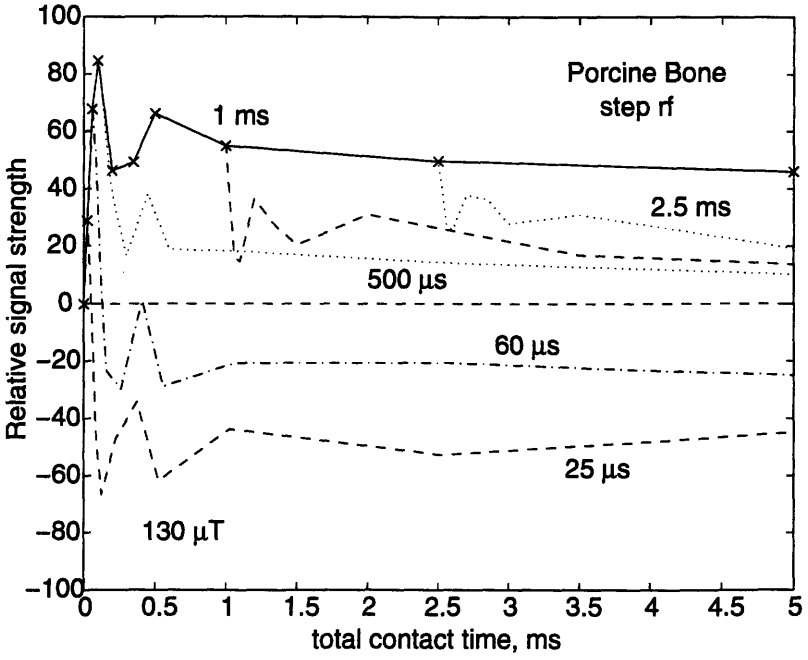
Porcine Bone
step rf
1 ms
2.5 ms
500 µs
60 µs
25 µs
130 µT
Relative signal strength
total contact time, ms

(b)

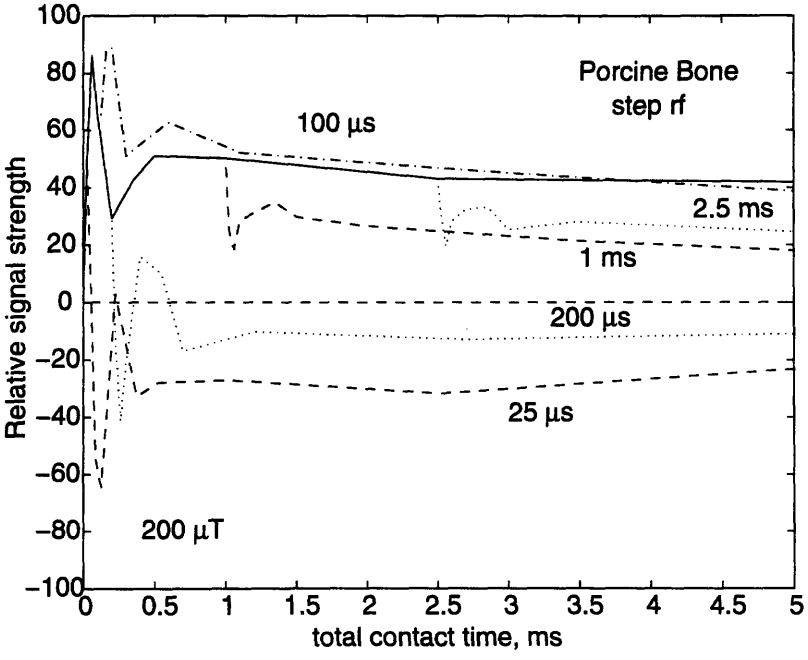
Porcine Bone
step rf
100 µs
2.5 ms
1 ms
200 µs
25 µs
200 µT
Relative signal strength
total contact time, ms

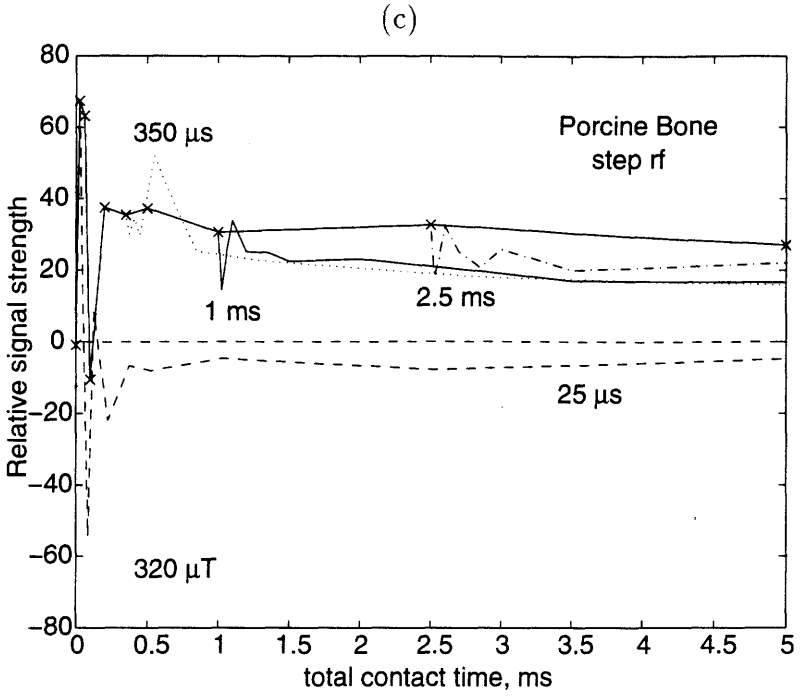

Figure 5-4: The effect of inverting the ^{31}P phosphorus temperature at various times during the cross polarization process in the bone specimen. The three rf field strengths are a) 130 μT, b) 200 μT, and c) 320 μT.

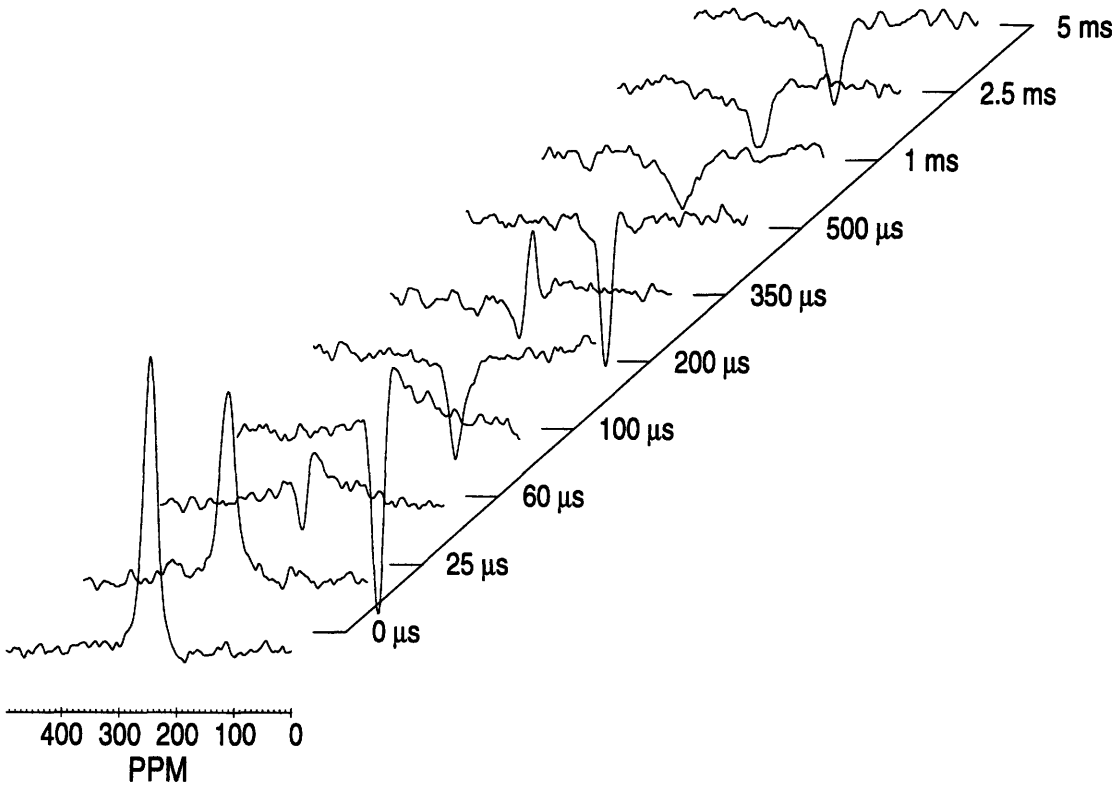

Figure 5-5: The spectra of porcine bone obtained at different reverse cross polarization times—indicated on the figure—after a forward cross polarization time of 60 μs. The rf field strength is 130 μT.

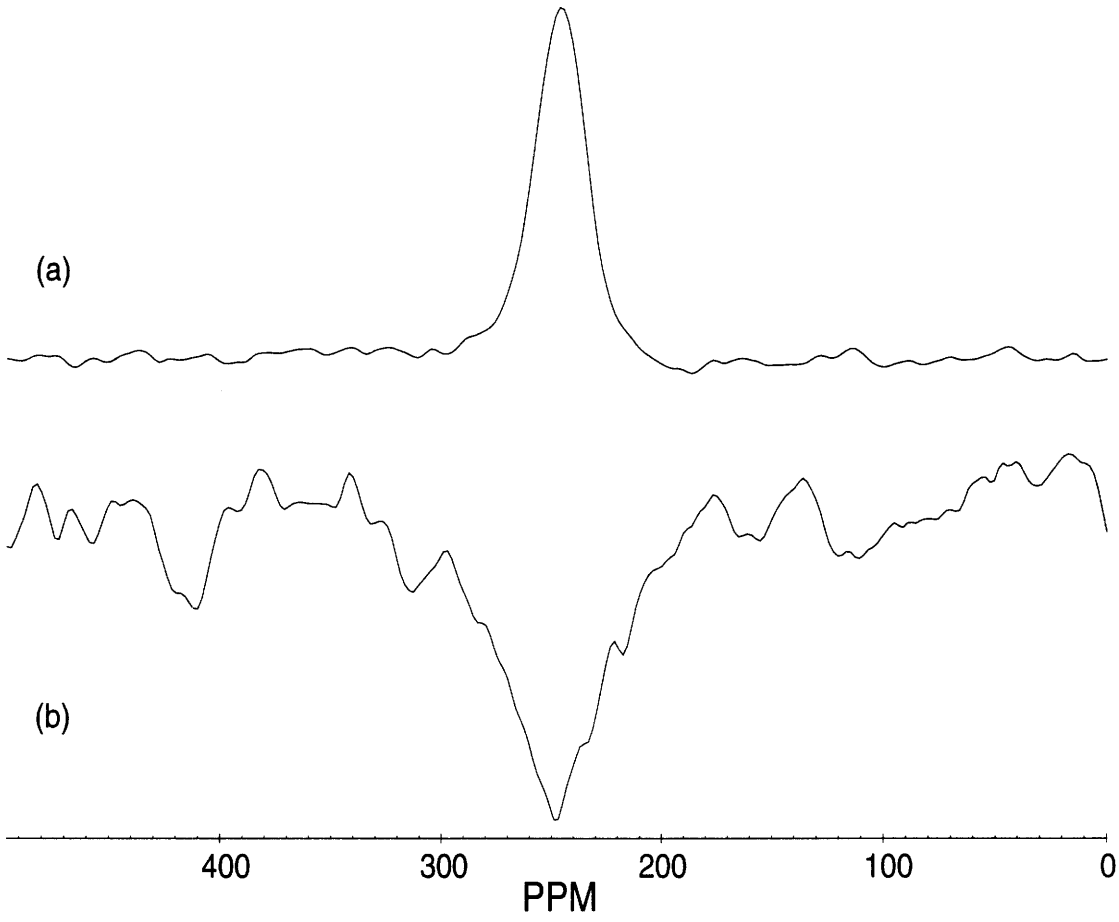

Figure 5-6: The spectrum of porcine bone obtained at (a) a forward cross polarization time of 60 μs, and (b) after an additional 1 ms reverse cross polarization. The linewidth of the best Gaussian fit is 2300 Hz for spectrum (a) and 4450 Hz for spectrum (b). The rf field strength is 130 μT.

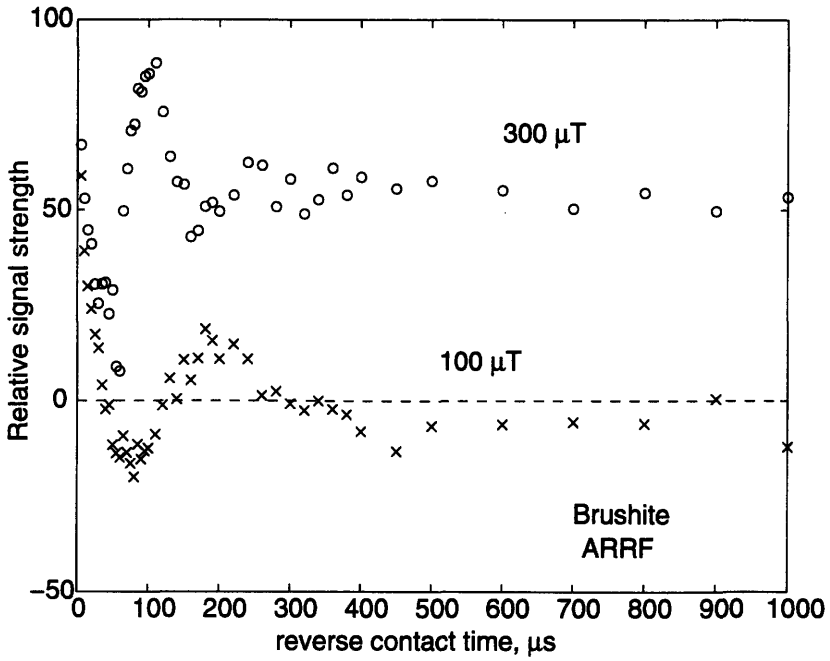

Figure 5-7: The effect of inverting the phase after an adiabatic remagnetization of the ^{31}P spins of brushite to maximum fields of 100 μT and 300 μT.

is easy to see that the ^{31}P and ^{1}H reservoirs are either no longer in contact with each other, or that the heat capacity of the ^{31}P spins has increased to the point where it is relatively unaffected by the proton system. There is a transient oscillation of the magnetization, but the asymptotic value of the signal does not change. In contrast, with a 100 μT field the ^{31}P spins respond very strongly, with the magnetization tending towards zero as the spin temperatures of the ^{1}H and ^{31}P systems equilibrate. The absolute magnitude of the transients is similar in both cases.

The results of the ramp remagnetization experiment on hydroxyapatite are shown in Figure 5-8, and closely parallel those of brushite. For a B_1= 70 μT there is a strong response to the change in the rf phase, while for the 500 μT field, there is no significant change in the signal after the transient oscillation. The artifactual straight line between 1 and 2 ms is due to the absence of data points in this interval.

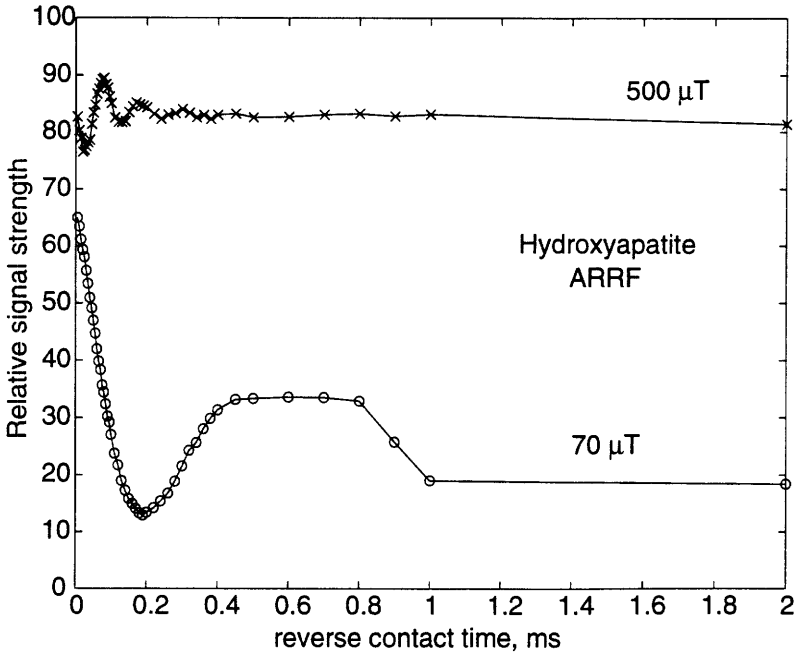

Figure 5-8: The effect of inverting the phase after an adiabatic remagnetization of the ^{31}P spins of hydroxyapatite to maximum fields of 70 μT and 500 μT.

5.4 Discussion

5.4.1 Transient oscillations

The sudden disequilibrium between the ^{1}H and ^{31}P spins produced transient oscillations in all our experiments. These oscillations occur after a discontinuous change in the Hamiltonian of one of the two spin systems. The presence of these transient oscillations makes it difficult to predict the zero-crossing of the signal based on the cross polarization time T_{IS} alone, as is usually done in conventional DCP experiments. The selection of an appropriate combination of forward and reverse cross polarization times to achieve spectral selection is therefore no longer straightforward task.

5.4.2 Spin calorimetry

As long as the experiments are conducted in a time short compared to the spin-lattice relaxation times T_{1D} and $T_{1\rho}$ of the sample it is possible to make quantitative

calculations of the relative heat capacities of the two spin systems. In addition, as the heat capacity of the ^{31}P spins depends on the size of the rf, it should also be possible to find the strength of the effective proton local field of the sample and to measure the effective number of protons in contact with each phosphorus nucleus in bone mineral, thus providing some information on the local ordering in the system.

5.4.3 Thermal contact

The adiabatic remagnetization experiments show that it is possible to break thermal contact between the Zeeman and dipolar reservoirs by increasing the strength of the rf sufficiently. This is expected as the thermal mixing and cross relaxation rates become very slow as the rf field in increased to a value much larger than the local fields. By varying the size of the applied rf field the interaction of these reservoirs can be examined over different regimes.

Chapter 6

Probe design

6.1 Introduction

The cross polarization experiments described in this thesis require irradiation of the samples at two frequencies, hence necessitating the use of a double resonance probe. The double resonance probe described here will be used for a number of experiments in the 4.7 T magnet, including *in vivo* studies on small animals. The probe was designed so that modular coils of different geometries may be interchanged by simply plugging the unit into a base which contains the variable tuning and matching capacitors for each port. This allows us to use the same set of high power variable capacitors, which are fairly expensive, with a variety of coils. In addition, this arrangement will allow us to perform most of the preparations outside the magnet where space constraints are not a problem, and to just slide the entire apparatus in when ready. The implementation of this modular design should not compromise the mechanical strength of the probe.

While the current experiments do not require simultaneous irradiation at the two frequencies, other experiments that we plan to perform do, requiring that the two ports are well isolated from each other. The most critical performance criterion is the efficiency of the low frequency channel that is used to detect the NMR signal. Poor performance in the high-frequency channel can be overcome by increasing the power output of the amplifiers, while the isolation can be improved with the use of external

filters.

6.2 Probe construction

The probe consists of a large 19.1 cm diameter, 162.6 cm long, acrylic cylinder that just fits into the bore of the magnet. A 91.4 cm long cutaway section on the side of the cylinder permits easy access to the inside for moving the animal in or out, or changing the coil unit. The base of the circuit containing the tunable capacitors is located 50.8 cm from one end of the cylinder. The capacitors are mounted on a semicircular printed circuit board that is mounted within the bore of the cylinder. The high frequency port is in a series-tune, parallel-match configuration, while the low frequency port is configured in a parallel-tune, series-match arrangement. Presently two flexible RG-9 coaxial cables with type-N connectors connect these capacitors to the external rf circuitry. This will eventually be replaced by rigid coaxial cable running from the capacitors to an end-panel at the edge of the cylinder, on which connectors will be mounted. Long acrylic tubes attached to the tuning and matching capacitors also extend out to the edge of the probe. They will later be attached to dials mounted on the end-panel. These dials will allow the tuning and matching capacitances for each coil to be recorded, and thus allow quick retuning when the coils are changed. A sketch of the apparatus is shown in Figure 6-1.

The coil mount uses the plastic inserts of Amphenol series MS 3106A–24–10 connectors, with only three of the seven pins used, one for each channel and a common ground path. We found that this connector provided sufficient rigidity and strength that no additional support was needed for the coil. The variable capacitors for the high and low frequency ports were shielded from each other with grounded copper foil in order to reduce the crosstalk between the two ports. This is not an ideal arrangement as it is susceptible to eddy currents if pulsed gradient fields are applied. We will be exploring alternative shielding arrangements in the future.

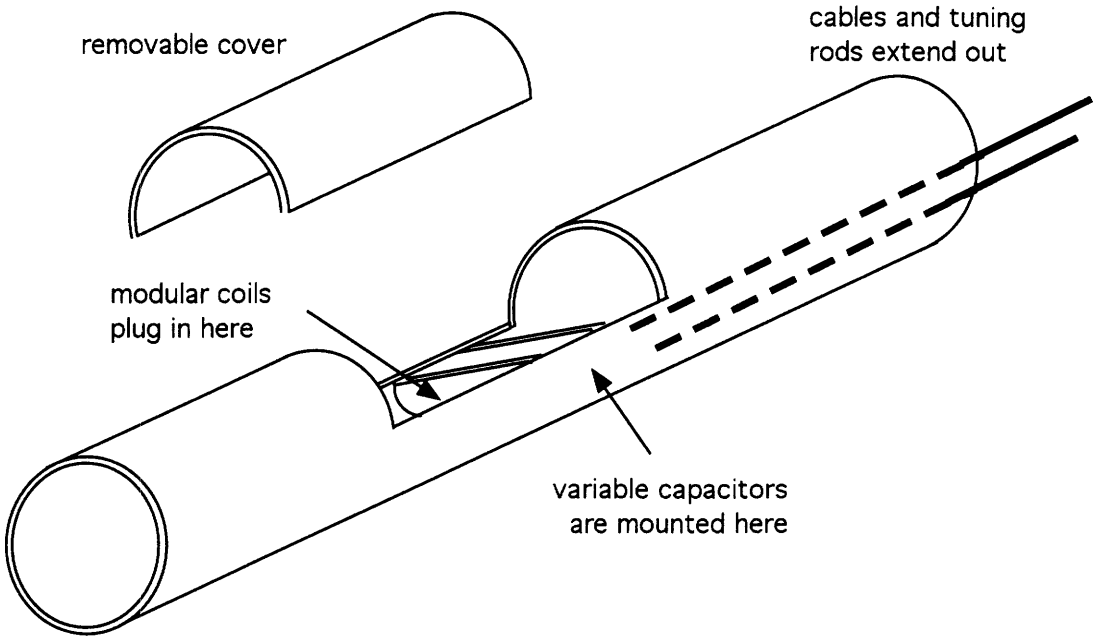

Figure 6-1: A sketch of the constructed probe

6.3 Coils

Two coils have been built for use with this probe, a surface coil and a cylindrical resonator.

6.3.1 The surface coil

The surface coil was built using a novel double resonant circuit that is described in detail here. It uses a generalized approach to two-port double resonant circuit design.

Circuit Design

The circuit configuration is based on a six-sided bridge with one branch shorted out in order to provide a common ground to both ports. We decided to try this configuration when we noticed that several two-port double resonance circuits are based on a four-sided bridge [104, 105, 106, 107, 108, 109, 110]. The generalized branch diagram of the circuit is shown in Figure 6-2. We can use Kirchoff's current and voltage laws to

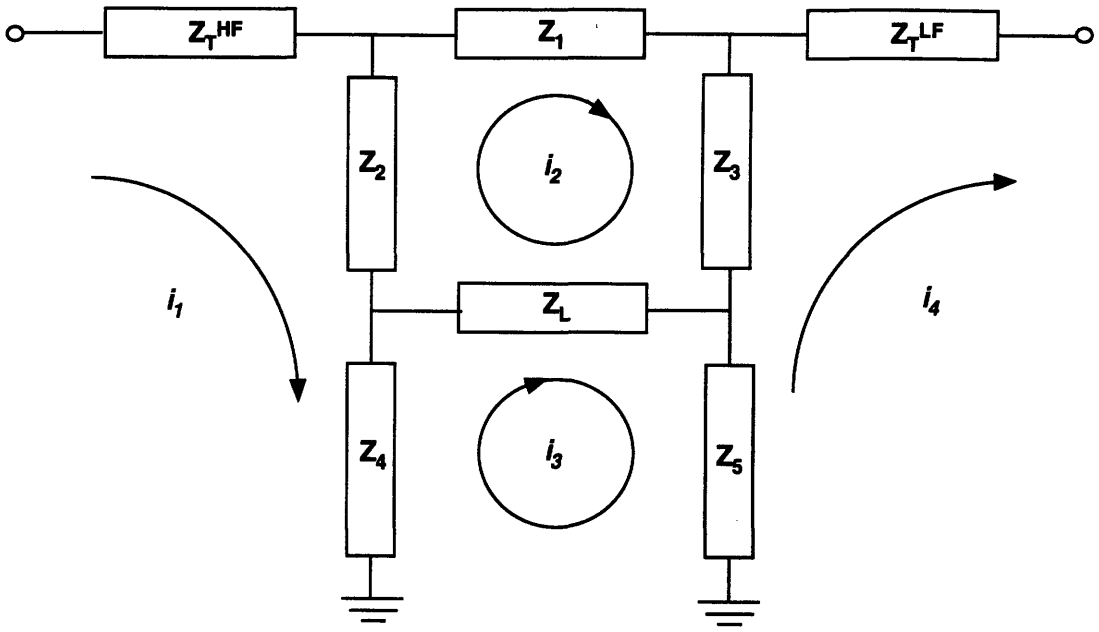

Figure 6-2: Schematic branch diagram of the double resonance circuit

write down the impedance matrix of this circuit.

$$\vec{V} = \bar{Z} \cdot \vec{I} \tag{6.1}$$

$$\vec{V} = \begin{bmatrix} v_1 \\ v_2 \\ v_3 \\ v_4 \end{bmatrix} \qquad \vec{I} = \begin{bmatrix} i_1 \\ i_2 \\ i_3 \\ i_4 \end{bmatrix} \qquad \bar{Z} = \begin{bmatrix} z_{11} & z_{12} & z_{13} & z_{14} \\ z_{21} & z_{22} & z_{23} & z_{24} \\ z_{31} & z_{32} & z_{33} & z_{34} \\ z_{41} & z_{42} & z_{43} & z_{44} \end{bmatrix} \tag{6.2}$$

The exact expressions for the impedance parameters z_{ij} in terms of the branch impedances are straightforward and are not presented here. We selected Z_L as the coil inductance, as it is the balanced element of the bridge. All the other elements were chosen to be capacitors, except Z_1 which was allowed to take on arbitrary values. The resulting impedance matrix $\bar{Z}$ was inverted to obtain the admittance matrix $\bar{Y} = \bar{Z}^{-1}$. The high frequency (HF) resonance condition is established by setting

the imaginary component of the current at the high frequency port to zero when the circuit is excited at that port, or

$$Im\{y_{11}\} = 0 \qquad \omega = \omega_{HF}. \tag{6.3}$$

In order for the low frequency port to be isolated from the high frequency port during high frequency excitation, we set

$$y_{41} = 0 \qquad \omega = \omega_{HF}. \tag{6.4}$$

Similarly, for the low frequency resonance and isolation conditions we have

$$Im\{y_{44}\} = 0 \qquad \omega = \omega_{LF}. \tag{6.5}$$

$$y_{41} = 0 \qquad \omega = \omega_{LF}. \tag{6.6}$$

The matrix inversion was performed with the symbolic mathematics package Maple, from the University of Waterloo. The conditions shown above lead to the following constraints on the branch impedances.

1. The impedance Z_1 is inductive at the low frequency and capacitative at the high frequency.

2. The high frequency isolation condition is

$$\omega_{HF}^2 L_S(C_3 + C_5)(C_2 + C_4) = C_2 + C_3 + C_4 + C_5 + \frac{C_2 C_3}{C_1}. \tag{6.7}$$

3. The low frequency isolation condition is

$$\omega_{LF}^2 L_S(C_3 + C_5)(C_2 + C_4) = C_2 + C_3 + C_4 + C_5 - \omega_{LF}^2 L_1 C_2 C_3. \tag{6.8}$$

4. The high frequency resonance condition is

$$(C_1 + C_T^{HF})(C_2 + C_3 + C_4 + C_5) + C_2(C_3 + C_4 + C_5) = \omega_{HF}^2(C_1 + C_T^{HF})(C_3 + C_5)(C_2 + C4) + \omega_{HF}^2 L_S C_2 C_4(C_3 + C_5). \quad (6.9)$$

5. The low frequency resonance condition is

$$C_2 + C_3 + C_4 + C_5) + \omega_{LF}^4 L_1 LS(C_2 + C_4)\left[C_T^{HF}(C_3 + C_5) + C_3 C_5\right] = \omega_{LF}^2 L_1\left[(C_3 + C_T^{LF})(C_2 + C_4 + C_5) + C_T^{LF} C_3\right] + \omega_{LF}^2 L_S(C_2 + C_4)(C_3 + C_5). \quad (6.10)$$

Circuit simulations

The circuit design was then simulated using the software package P-SPICE, a commercially available version of Berkeley SPICE for the IBM-PC. The software package has a graphical interface that automatically generates a net list from the circuit that is drawn by the user, making it much easier to use SPICE. The circuit schematics used in the simulation are shown in Figure 6-3.

The calculated values for the circuit elements were put into the simulation and the circuit was tested from 20 MHz to 250 MHz at both ports. The simulation package allows for easy testing of the circuit as various parameter values are changed. It was not possible to simulate an ideal circuit since SPICE requires that every node in the circuit have a dc path to ground so that a dc bias point can be found. This was done by placing 10 GΩ resistances in parallel with those capacitors that did not have a parallel dc path. This did not affect the calculations significantly here. We tested the circuit under conditions of sample loading, as well as with stray capacitances. Sample results of such a simulation are shown in Figure 6-4.

The simulations could, however, only provide proof of the general validity of the circuit design and did not help very much with finding correct values for the actual circuit construction. The introduction of stray capacitances and the strong depen-

(a)

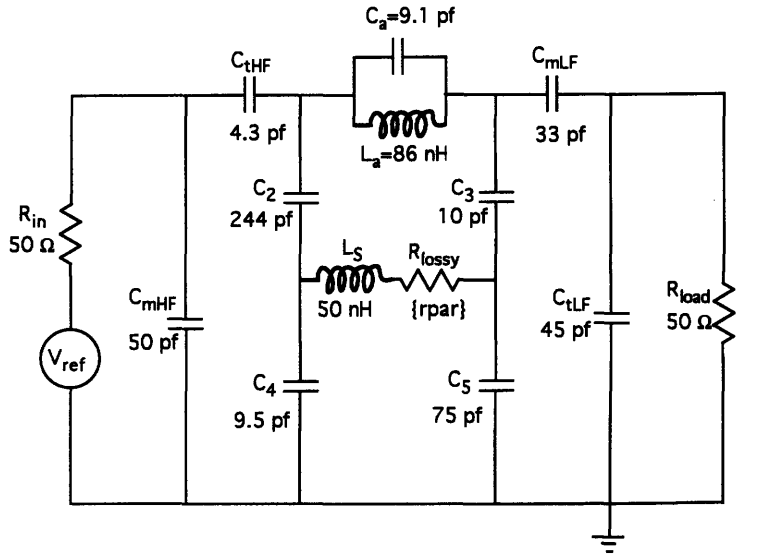

(b)

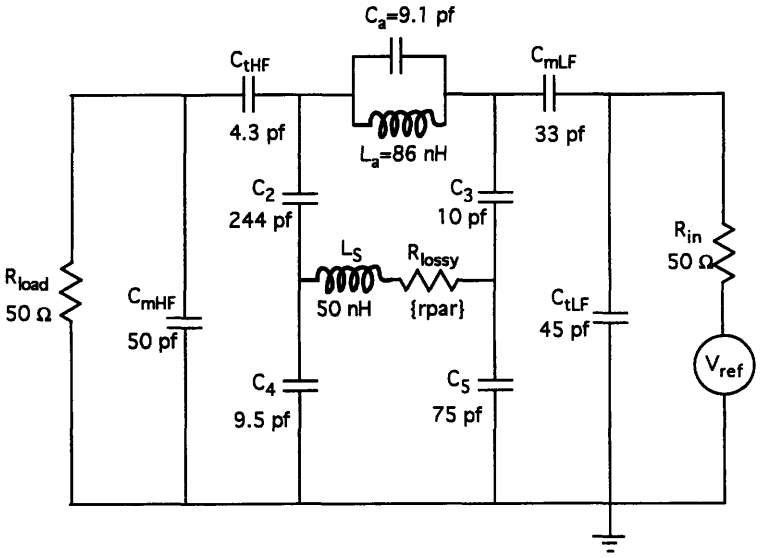

Figure 6-3: The P-SPICE representation of the double resonance circuit, during the simulation of a) the excitation of the high frequency port; and b) the excitation of the low frequency port. *Rpar*, representing the sample losses in this case is a variable parameter that can be varied easily.

dence on the actual physical construction of the coil make it very difficult to obtain more than a ballpark estimate of the actual component values needed.

Physical realization

The surface coil being built for the *in vivo* studies needs to have a diameter of at least 7.5 cm in order to achieve the penetration required to reach the limb bones or vertebrae of a small animal. An 8.9 cm diameter surface coil was etched on a printed circuit board, to provide coil rigidity as well as keep its inductance to a minimum. Finding the optimal capacitance values required a few iterations and required a compromise between optimizing the coil performance at the two frequencies and ensuring sufficient isolation between the two ports during rf irradiation.

The isolation between the two ports of the coil once it was mounted in the probe was 14 dB at 81 MHz and 21 dB at 200 MHz. The ninety degree pulses obtained were 425 μs at 81 MHz and 250 μs at 200 MHz, with about 450 W power (^{1}H and ^{31}P) available at the probe. The previous 4.8 cm diameter surface coil has 90 degree pulses of 30 μs and 60 μs at 81 MHz and 200 MHz respectively. As the diameter of the new surface coil is 1.85 times larger than that of the old coil, a scaling of the pulse lengths of the old coil to the larger size gives us expected 90 degree pulses of 103 μs and 206 μs at 81 MHz and 200 MHz. These long pulses indicate that the circuit performance needs to be optimized further. However, the large effective volume of this coil will probably necessitate the use of even higher powered amplifiers if short pulses on the order of 25 μs are required.

6.3.2 A double tuned resonator

In order to test the modularity of the probe design, a second plug-in coil, a double-tuned resonator, was designed. Double-tuned resonators have been discused in detail by Hecke *et al.* [111]. The design of this double-tuned 2.5 cm diameter, 7.6 cm long cylindrical resonator was suggested to us by Dr. Cory. The coil was built to be relatively proton-free in order to eliminate the background signal while performing

(a)

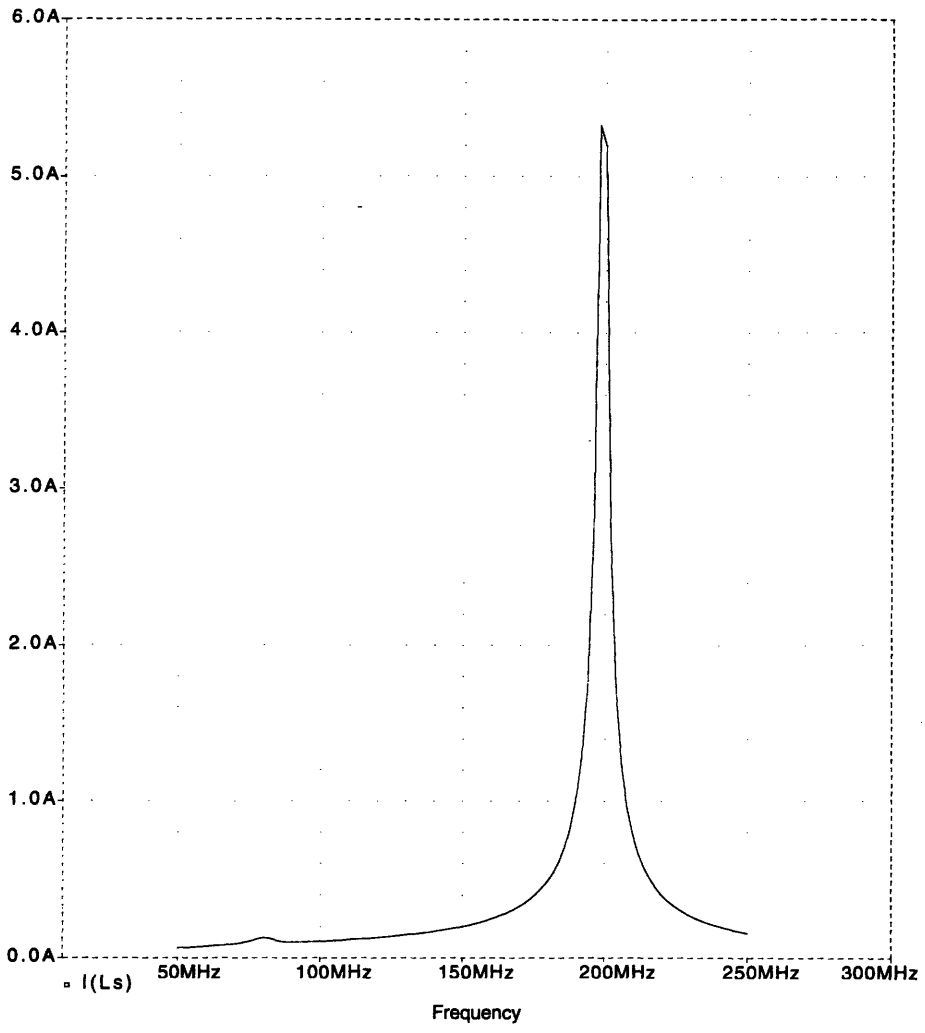
6.0A
5.0A
4.0A
3.0A
2.0A
1.0A
0.0A
I(Ls)
50MHz
100MHz
150MHz
200MHz
250MHz
300MHz
Frequency

(b)

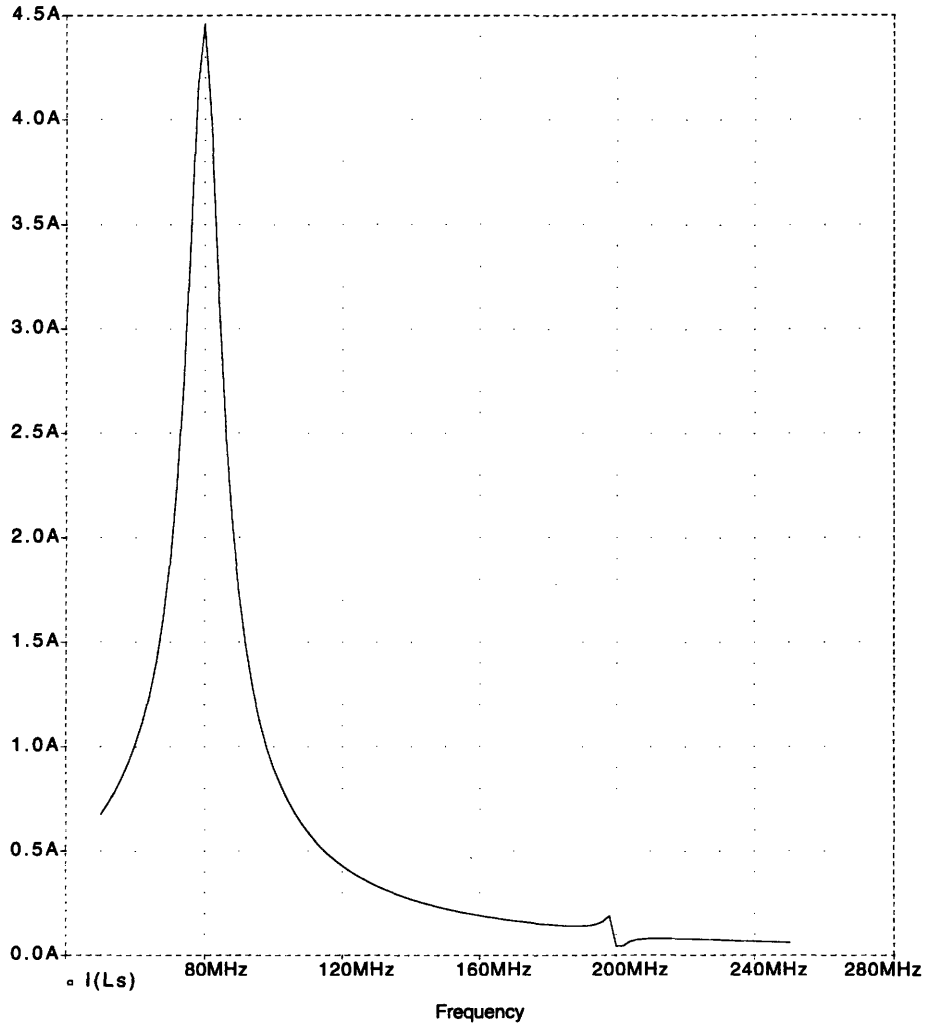

Figure 6-4: Simulating the response to a sinusoidal input voltage of frequencies in the range from 20 MHz to 250 MHz. The current through the sample coil is shown as a) the high frequency port is excited; and b) the low frequency port is excited for a sample resistance of 0.1 Ω

solid state experiments on protons. The two ports were tuned to the ^{1}H and ^{31}P frequencies respectively after the the coil was inserted into the base with the variable capacitors. The isolation between the two ports was 14.5 dB at 81 MHz and 30 dB at 200 MHz. The 90 degree pulses obtained at maximum power was 50 μs at both frequencies. All the experiments of chapter 4 were performed with this coil.

The ability to interchange coils of different designs and geometries with the same probe base demonstrates the success of this design.

Chapter 7

Summary and Conclusions

This thesis has explored the applicability of the solid state NMR technique of ADRF cross polarization to the study of calcium phosphates and bone mineral under conditions that are largely compatible with *in vivo* application. The development of true *in vivo* techniques to study bone mineral chemistry would contribute greatly to our understanding of mineral dynamics and could have significant clinical implications in the evaluation of treatments for metabolic bone diseases as well as the status of calcium phosphate cements and implants.

ADRF Cross Polarization

ADRF cross polarization between the protons and phosphorus occurs when thermal contact is initiated between the proton spin system, which is initially prepared in a state of dipolar order, and the phosphorus spin system, causing their temperatures to equilibrate. The reduction in the temperature of the phosphorus reservoir is then detected as an observable NMR signal. The polarization transfer is mediated by the heteronuclear dipolar coupling between the spins, being faster for strongly coupled spin systems and slower for weakly coupled systems. As the dipolar coupling is strongly dependent on the internuclear distance between the two spins, the rate of cross polarization is well correlated with the average internuclear distance between the two species in the sample, when the energy levels of the two spins are matched.

The application of the phosphorus rf initiating the polarization transfer results

in transient oscillations between the two systems at short times. These oscillations, which are produced by the rf modulation of the proton-phosphorus dipolar coupling Hamiltonian, occur approximately at the rotating frame effective Larmor frequency of the phosphorus spins. The asymptotic phosphorus signal observed depends on the relative magnitudes of the proton local field and the phosphorus rf field, the heat capacities of the two spin systems, and their spin-lattice relaxation times.

Applications to the calcium phosphates and bone mineral

^{1}H–^{31}P ADRF cross polarization with a surface coil was used to study powdered samples of synthetic hydroxyapatite and brushite, and a specimen of porcine. The cross polarization was observed to be faster in brushite than in hydroxyapatite. This is expected as as brushite contains monohydrogen phosphate groups while hydroxyapatite contains non-protonated phosphate groups. Optimal cross polarization occurred at a phosphorus B_1 field of ≈ 280 μT for brushite and ≈ 60 μT for hydroxyapatite. It was possible to suppress the hydroxyapatite and observe the brushite signal in a sample containing 90% hydroxyapatite and 10% brushite, by applying the optimal rf field for brushite (≈ 270 μT) and detecting the signal during a zero crossing of the transient oscillation. At early times the brushite cross polarization has grown significantly compared to the hydroxyapatite, due to its shorter cross polarization time. We then applied this procedure to the specimen of porcine bone and were able to suppress the dominant non-protonated phosphate in the mineral and directly observe the protonated phosphate using an rf field of ≈ 110 μT.

The observation of the signal at short cross polarization times helps us achieve spectral selectivity at the expense of signal strength. This loss of signal strength complicates the application of the technique *in vivo*. The spectral suppression of the non-protonated phosphate is also incomplete as only the transient component is nulled, while the growing cross polarization signal is still present, though it is small at short contact times.

Creation of dipolar order

The final temperature of the phosphorus system, and hence the magnitude of the fid, is dependent on the initial temperature of the proton dipolar system. In addition, the B_1 inhomogeneities of a surface coil result in spatially variant flip angles when pulse techniques are used and hence produce spatial variations in the proton dipolar state. We examined three ADRF techniques and the Jeener-Broekaert sequence to produce this dipolar ordered state in order to improve signal strength and to reduce the effect of the B_1 inhomogeneities.

The first ADRF method, used in the above cross polarization studies, used a 90 degree pulse followed by spin-locking and a linear ramp demagnetization of the amplitude of the rf. The second used an adiabatic frequency sweep onto resonance with a strong rf field to create a spin-locked state, and a linear ramped demagnetization of the amplitude of the field. The final ADRF technique used an adiabatic sweep onto resonance with an rf field whose magnitude is small compared to the local field of the protons. An exponential phase roll was used to create the frequency sweeps onto resonance. The four methods were studied in samples of hydroxyapatite and brushite, and their relative efficiencies compared.

The adiabatic sweep onto resonance with a weak rf field was the most efficient technique in the study of hydroxyapatite, while the 90 degree pulse followed by spin locking and ramp demagnetization in a time similar to the duration of the 90 degree pulse, in effect a Jeener-Broekaert sequence, was the most efficient method for brushite. The poor performance of the ADRF techniques in brushite is puzzling and might be due to thermal mixing between the dipolar and Zeeman reservoirs during the demagnetization, leading to an increase in the entropy of the system. Brushite contains two distinct classes of protons with different local fields and thermal mixing between these reservoirs could be the source of the irreversibility. The use of an adiabatic frequency sweep followed by a ramp demagnetization is the most sensitive to T_{1D} effects as it takes the longest time to complete. When applying long pulses at higher rf powers the output of our amplifiers drooped, leading to inconclusive results.

ADRF differential cross polarization

A differential cross polarization experiment was performed with the ADRF technique by shifting the phase of the ^{31}P rf by 180 degrees during the cross polarization process to invert the temperature of the spins. Differential cross polarization uses differences in the cross polarization times (T_{IS}) of spectrally overlapping species to selectively null one species and isolate the other. After the temperature inversion, the phase of the phosphorus may invert as it equilibrates again with the proton spin system. The time at which the zero crossing occurs, before the inversion of the phase of the observed signal, depends on T_{IS}. Thus by observing the signal at the zero crossing of a particular species, it should be possible to selectively eliminate it from the spectrum.

Experiments were performed on samples of hydroxyapatite, brushite and a specimen of porcine bone. It was possible to invert the phase of the observed phosphorus signal if the temperature inversion was performed before the two spins had equilibrated. However, the temperature inversion produced transient oscillations between the proton and phosphorus reservoirs, complicating the spectral selection. When the inversion was performed after temperature equilibration had taken place, the magnitude of the final signal was reduced significantly and did not invert, indicating that the heat capacities of the protons and phosphorus systems are comparable to each other. On inverting the temperature with an rf field much stronger than the local fields, there was no noticeable change in the phosphorus signal after the transient oscillations, indicating a break in the thermal contact between the two spin species.

It is possible to perform spin calorimetry experiments by changing the time at which the phosphorus temperature is inverted, and thus obtain the relative heat capacities of the two spin systems. Changing the amplitude of the phosphorus rf also changes the rate at which the two systems are able to equilibrate. Thus we should be able to study the behaviour of these spins across a wide range of conditions and probe their dipolar states.

Probe design

A two-port double resonance probe has been built for experiments in a 4.7 T 30 cm diameter horizontal bore magnet. The probe contains high-power variable capacitors for tuning and matching the two ports, with the high-frequency port configured in a series-tune, parallel-match arrangement, and the low-frequency port in a parallel-tune, series-match arrangement. Different coils may be plugged into this base using an Amphenol connector, allowing the same variable capacitors to be used with coils of different design, configurations, and even for the study of different nucleii. The probe can be used for small animal experiments and allows all the preparations to be made outside the magnet.

Two coils were built for this probe, a large 8.9 cm diameter surface coil using a novel circuit design and a cylindrical resonator. It was possible to tune and match both coils and aquire NMR spectra using the modular arrangement. The surface coil had 14 dB isolation between the two ports at 81 MHz and 21 dB at 200 MHz, while the resonator has 14.5 dB isolation at 81 MHz and 30 dB at 200 MHz. The 90 degree pulses for the surface coil were 425 μs at 81 MHz and 250 μs at 200 MHz, and 50 μs at both frequencies for the resonator. While the performance of the surface coil can probably be improved, it will be necessary to drive the coil with a more powerful amplifier in order to reduce the 90 degree pulses significantly.

Future work

This thesis has studied the application of the ADRF cross polarization technique to calcium phosphate samples and bone mineral. Improvements in signal strength and spectral selectivity were suggested in the studies of the creation of dipolar order and the development of an ADRF differential cross polarization technique. Further work is required in demonstrating the *in vivo* applicability of the technique.

The samples used so far in the ADRF-CP experiment have been small samples placed in a relatively uniform portion of the B_1 field of the surface coil. The effect of the B_1 inhomogeneities will be compounded when large samples are used, especially

if they extend out of the field of view of the coil. It is unlikely that we will observe a well resolved oscillation frequency in this case. The broad distribution of oscillation frequencies will appear as an oscillation at the central frequency but will damp rapidly. Thus it will not be possible to use a zero crossing of the oscillation to suppress the PO_4^{3-} signal, and other techniques will be neccesary to improve the spectral selectivity. The low signal strength is also a problem. We can use an adiabatic remagnetization of the phosphorus spins to improve the signal strength, but in doing so we allow all phosphate species to cross polarize efficiently and lose spectral selection. This total phosphorus signal could be used to measure bone mineral content as has been previously suggested. The extension to an imaging experiment could also allow measurement of bone mineral densities.

It is necessary to measure the actual rf power deposition in a lossy sample with the ADRF cross polarization technique and determine under what conditions—duration of pulses, recycle time, *et cetera*—the power levels used are safe for *in vivo* purposes. Quantitative comparisons of rf power deposition and signal strength need to be made between the ADRF-CP technique and conventional spin-lock CP techniques. It should then be possible to use the technique to study bone mineral in a small animal, such as a rabbit, and determine the signal strengths and spectral selectivity achievable.

The studies on the creation of dipolar order could be improved by using a coil with shorter 90 degree pulses and an amplifier capable of producing large spin-lock fields lasting a few milliseconds in duration. A comparison of the relative performances of the different techniques in a surface coil and a resonator or a solenoidal coil is necessary in order to measure the impact of using frequency sweeps.

No attempt was made in these experiments to optimize the shape of the demagnetization ramp or the type of frequency sweeps used. It may be possible to increase the signal strength further by optimizing these parameters as well. The Jeener-Broekaert sequence used was designed for a single spin species and needs to be modified if it is to be optimal for a system containing two spin species, though it becomes sample dependent in the process. As the relative efficiencies of each of these techniques varies with the particular sample used, the appropriate selection of a particular technique should

allow us to improve our spectral selectivity as well especially if these are tailored to the species present in bone mineral.

The oscillations in the differential cross polarization experiment present an obstacle to spectral selection. It will be interesting to observe the performance of the technique with larger samples where the B_1 inhomogeneities become important. However, the cross polarization time T_{IS} is also field dependent and so the zero crossing will not be unique. Other methods to damp out the oscillations need to be investigated.

A double-resonance probe with modular, interchangeable coils has been built, in which these animal experiments may be performed. The design constraints used may not have been optimal for coil performance. We could alternately have maximized the coil current at the two frequencies subject to a number of constraints, including isolating the two ports, setting the imaginary currents equal to zero and 50 Ω impedence matching. This is a maximization problem that can be solved relatively straightforwardly.

Adapting the probe for imaging experiments requires us to change the shielding to prevent eddy currents. We are investigating shielding grids created by two sets of parallel wires that are laid one on top of the other at right angles to each other, with a thin layer of insulation between them so that are electrically isolated from each other.

This thesis has demonstrated that it is possible to obtain biochemically important information under conditions compatible with *in vivo* application. Significant additional work needs to be done to allow its practical application in a clinical setting. A number of techniques have been proposed and investigated in order to acheive this goal. The results of this thesis suggest that that it will be very difficult to achieve true spectral selectivity in the *in vivo* situation. However, we should be able to use these techniques to produce contrast between the protonated and non-protonated phosphates. The ADRF cross polarization technique studied here can also be used to do non-destructive testing on macroscopic objects, where conventional solid-state techniques cannot be used.

Appendix A

Spin Hamiltonians

A.1 The Zeeman Hamiltonian

The magnetic moment operator of a system containing N spins of a single speciesis defined as

$$\vec{\mu} = \hbar\gamma_I \sum_{j=1}^{N_I} I_j. \tag{A.1}$$

The Zeeman Hamiltonian associated with an external magnetic field can then be written as

$$\mathcal{H}_Z = -\vec{\mu} \cdot \vec{B}. \tag{A.2}$$

In the usual NMR situation the magnetic field consists of a large static field and a smaller time-varying field, $\vec{B} = B_0\hat{z} + 2B_1\cos(\omega t)\hat{x}$, and the Zeeman Hamiltonian is given by

$$\mathcal{H}_Z = -\hbar\gamma_I \left[B_0 I_z + 2B_1 \cos(\omega t) I_x\right]. \tag{A.3}$$

We can transform this (x, y, z) coordinate representation into one rotating at frequency ω about the direction of the static Zeeman field $(x_r, y_r, z_r = z)$. This operation is represented by the unitary transformation

$$R_z(\omega t) = exp\{i\omega t I_z\}. \tag{A.4}$$

The resulting Hamiltonian in the rotating frame is

$$\mathcal{H}_Z^r = -\hbar\gamma_I \left\{ \left(B_0 - \frac{\omega}{\gamma} \right) I_z^r + B_1 I_x^r \right\}. \tag{A.5}$$

The effective field

$$\vec{B}_{\text{eff}} = \left(B_0 - \frac{\omega}{\gamma} \right) \hat{z}_r + B_1 \hat{x}_r \tag{A.6}$$

is oriented at an angle Θ with respect to $\hat{z}_r$, where

$$\tan\Theta = \frac{B_1}{B_0 - \omega/\gamma_I} \tag{A.7}$$

is the off-resonance angle. We then rotate the (x_r, y_r, z_r) system about y_r so that the z_r axis is aligned along the effective field. The unitary transformation corresponding to this rotation is

$$R_{y_r}(\Theta) = exp\{i\Theta I_{y_r}\}. \tag{A.8}$$

The corresponding Zeeman Hamiltonian in the tilted rotating frame is

$$\mathcal{H}_Z^\rho = -\hbar\gamma_I B_{\text{eff}} I_z^\rho. \tag{A.9}$$

This is identical in form to Equation (A.3), and represents a spin system in a static field of magnitude B_1 and no time-dependent fields.

A.2 The dipolar Hamiltonian

The direct dipolar Hamiltonian can be written as

$$\mathcal{H}_D = \sum_{j>} \sum_{k} \sum_{q=-2}^{+2} A_{jk}^{(q)} F_{jk}^{(q)} \tag{A.10}$$

where the $A_{jk}^{(q)}$ are spin-operators and $F_{jk}^{(q)}$ are geometrical functions dependent on the spatial coordinates of the spins. The spin operators are defined as follows

$$A_{jk}^{(0)} = \frac{1}{2}\gamma_j\gamma_k\hbar^2\left(3I_{jz}I_{kz} - \vec{I}_j\cdot\vec{I}_k\right) \quad (A.11)$$

$$A_{jk}^{(\pm1)} = -\frac{3}{2}\gamma_j\gamma_k\hbar^2\left(I_{jz}I_k^{\pm} + I_j^{\pm}I_{kz}\right) \quad (A.12)$$

$$A_{jk}^{(\pm2)} = -\frac{3}{4}\gamma_j\gamma_k\hbar^2 I_j^{\pm}I_k^{\pm} \quad (A.13)$$

where $A_{jk}^{(q)} = A_{kj}^{(q)}$. The functions $F_{jk}^{(q)}$ are expressed in terms of the spherical coordinates of the internuclear vector between the j and k spins $(r_{jk}, \theta_{jk}, \phi_{jk})$, with respect to the direction of B_0. They are

$$F_{jk}^{(0)} = r_{jk}^{-3}\left(1 - 3\cos^2\theta_{jk}\right) \quad (A.14)$$

$$F_{jk}^{(\pm1)} = r_{jk}^{-3}\sin\theta_{jk}\cos\theta_{jk}\exp(\pm i\phi_{jk}) \quad (A.15)$$

$$F_{jk}^{(\pm2)} = r_{jk}^{-3}\sin^2\theta_{jk}\exp(\pm 2i\phi_{jk}). \quad (A.16)$$

where $F_{jk}^{(q)} = F_{kj}^{(q)}$. If all spins are identical, the $q = 0$ term represents the secular dipolar Hamiltonian and the remaining terms the non-secular Hamiltonian. Transforming to the rotating frame as described in Equation (A.4) above, we get

$$\mathcal{H}_D^r = \sum_{j>}\sum_{k}\sum_{q=-2}^{+2} A_{jk}^{r\,(q)}F_{jk}^{(q)}exp(iq\omega t), \quad (A.17)$$

where the $A_{jk}^{r\,(q)}$ are formally identical to $A_{jk}^{(q)}$ with the components of $\vec{I}$ replaced by their corresponding rotating frame components $\vec{I}_r$. Thus only the secular component of the laboratory frame Hamiltonian ($q = 0$) is time-independent in the rotating frame, while the non secular components oscillate at frequencies ω and 2ω. Transforming into the tilted rotating frame and neglecting the time-varying terms, the dipolar Hamiltonian is given by

$$\mathcal{H}_D^{\rho} = \sum_{j>}\sum_{k}\sum_{p=-2}^{+2} A_{jk}^{\rho\,(p)}F_{jk}^{\rho\,(p)}, \quad (A.18)$$

where the operators $A_{jk}^{\rho\,(p)}$ are identical to their laboratory frame definitions, with the replacement of the components of $\vec{I}$ by the components of $\vec{I}_\rho$ in the tilted rotating frame. The geometrical functions $F_{jk}^{\rho\,(p)}$ are defined as follows

$$F_{jk}^{\rho\,(0)} = \left(\frac{3}{2}\cos^2\Theta - \frac{1}{2}\right) F_{jk}^{(0)} \tag{A.19}$$

$$F_{jk}^{\rho\,(\pm 1)} = \frac{1}{2}\cos\Theta\sin\Theta F_{jk}^{(0)} \tag{A.20}$$

$$F_{jk}^{\rho\,(\pm 2)} = -\frac{1}{2} sin^2\Theta F_{jk}^{(0)} \tag{A.21}$$

where Θ the off-resonance angle is defined in Equation (A.7). Thus Equation (A.18) is seen to be formally identical to the laboratory frame dipolar Hamiltonian in Equation (A.10). The $p = 0$ term in Equation (A.18) represents the secular contribution if all spins are identical.

Bibliography

[1] W. A. Peck. Office of medical applications of research, National Institutes of Health. Consensus conference on osteoporosis. *J. Am. Med. Assoc.*, 53:799–802, 1984.

[2] National Institute of Aging Workshop on Aging and Bone Quality. *Calcif. Tissue. Int.*, 53 Suppl 1:S1–S180, 1993.

[3] P. D. Miller, S. L. Bonnick, and C. J. Rosen. Consensus of an international panel on the clinical utility of bone mass measurement in the detection of low bone mass in the adult population. *Calcif. Tissue Int.*, 58:207–214, 1996.

[4] M. J. Glimcher, L. C. Bonar, M. D. Grynpas, W. J. Landis, and A. H. Roufosse. Recent studies of bone mineral: Is the amorphous calcium phosphate theory valid? *J. Crystal Growth*, 53:100–119, 1981.

[5] A. S. Posner, N. C. Blumenthal, and N. Betts. *Phosphate Minerals*, pages 330–350. Springer-Verlag, New York, 1984.

[6] H. A. Lowenstam and S. Weiner. *On Biomineralization.* Oxford University Press, Oxford, 1989.

[7] J. C. Elliot. *Structure and chemistry of the apatites and other calcium orthophosphates.* Elsevier, Amsterdam, 1994.

[8] W. F DeJong. La substance minérale dans les os. *Rec. Trav. Chim.*, 45:445–448, 1926.

[9] Walter E. Brown, James P. Smith, James R. Lehr, and A. William Frazier. Crystallographic and chemical relations between octacalcium phosphate and hydroxyapatite. *Nature*, 196:1050–1054, 1962.

[10] W. E. Brown, L. W. Schroeder, and J. S Ferris. Interlayering of crystalline octacalcium phosphate and hydroxylapatite. *J. Phys. Chem.*, 83:1385–1388, 1979.

[11] M. D. Grynpas, L. C. Bonar, and M. J. Glimcher. Failure to detect an amorphous calcium-phosphate solid phase in bone mineral: a radial distribution function study. *Calcif. Tissue Int.*, 36:291–301, 1984.

[12] A. Boyde. *The biochemistry and physiology of bone*, chapter Scanning electron microscope studies of bone. Academic Press, New York, 1972.

[13] A. Boyde, P. G. T. Howell, T. G. Bromage, J. C. Elliott, C. M. Riggs, L. S. Bell, M. Kneissel, S. A. Reid, J. A. P. Jayasinghe, and S. J. Jones. Applications of mineral quantitation of bone by histogram analysis of backscattered electron images. In Antonio Pecile and Benedetto de Barnard, editors, *Bone Regulation Factors: Morphology, Biochemistry, Physiology and Pharmacology.* Plenum Press, New York, 1990.

[14] John G. Skedros, Roy D. Bloebaum, Kent N. Bachus, Todd M. Boyce, and Brent Constantz. Influence of mineral content and composition on graylevels in backscattered electron images of bone. *J. Biomed. Mater. Res.*, 27:57–64, 1993.

[15] W. F. Neuman and M. W. Neuman. *The Chemical Dynamics of Bone Mineral.* University of Chicago Press, Chicago, 1958.

[16] J. D. Termine and A. S. Posner. Infrared analysis of rat bone: age dependency of amorphous and crystalline mineral fractions. *Science*, 153:1523–1525, 1966.

[17] C. Rey, J. Lian, M. Grynpas, F. Shapiro, L. Zylberberg, and M. J. Glimcher. Non-apatitic environments in bone mineral: FT-IR detection, biological properties and changes in several disease states. In *The Chemistry and Biology of Mineralized Tissues: Proceedings of the Third International Conference on the Chemistry and Biology of Mineralized Tissues Held in Chatham, Massachusetts on October 16-21, 1988*, pages 597–603, New York, 1989. Gordon and Breach, Science Publishers, Inc.

[18] C. Rey, M. Shimizu, B. Collins, and M. J. Glimcher. Resolution-enhanced Fourier transform infrared spectroscopy study of the environment of phosphate ion in the early deposits of a solid phase of calcium phosphate in bone and enamel and their evolution with age: I. Investigations in the ν_4-PO_4^{-3} domain. *Calcif. Tissue Int.*, 46:384–394, 1990.

[19] C. Rey, M. Shimizu, B. Collins, and M. J. Glimcher. Resolution-enhanced Fourier transform infrared spectroscopy study of the environment of phosphate ion in the early deposits of a solid phase of calcium phosphate in bone and enamel and their evolution with age: II. Investigations in the ν_3-PO_4^{-3} domain. *Calcif. Tissue Int.*, 49:383–388, 1991.

[20] C. Rey, K. Beshah, R. Griffin, and M. J. Glimcher. Structural studies of the mineral phase of calcifying cartilage. *J. Bone Miner. Res.*, 6:515–525, 1991.

[21] D. P. Swanson, H. M. Chilton, and J. H. Thrall. *Pharmaceuticals in Medical Imaging*, chapter Radiopharmaceuticals for bone and bone marrow imaging, pages 537–563. MacMillan, New York, 1990.

[22] W. A. Peck and W. L. Woods. *Osteoporosis: etiology, diagnosis and management*, chapter The cells of bone. Raven Press, New York, 1988.

[23] H. M. Frost. *Bone biodynamics*, chapter Dynamics of bone remodelling. Little, Brown and Co., Boston, 1964.

[24] Edward D. Eanes. Physico-chemical principles of biomineralization. In Antonio Pecile and Benedetto de Barnard, editors, *Bone Regulation Factors: Morphology, Biochemistry, Physiology and Pharmacology.* Plenum Press, New York, 1990.

[25] Ermanno Bonucci. The histology, histochemistry, and ultrastructure of bone. In Antonio Pecile and Benedetto de Barnard, editors, *Bone Regulation Factors: Morphology, Biochemistry, Physiology and Pharmacology.* Plenum Press, New York, 1990.

[26] E. D. Eanes and A. S. Posner. A note on the crystal growth of hydroxyapatite precipitated from aqueous solutions. *Mater. Res. Bull.*, 5:377–384, 1970.

[27] J. D. Termine and A. S. Posner. Amorphous/crystalline interrelationships in bone mineral. *Calc. Tiss. Res.*, 1:8–23, 1967.

[28] E. D. Eanes, J. D. Termine, and A. S. Posner. Amorphous calcium phosphate in skeletal tissues. *Clin. Orthoped.*, 53:223–235, 1967.

[29] A. H. Roufosse, W. J. Landis, W. K. Sabine, and M. J. Glimcher. Identification of brushite in newly deposited bone mineral from embryonic chicks. *J. Ultrastruct. Res.*, 68:235–255, 1979.

[30] Laurence C. Bonar, M. D. Grynpas, and Melvin J. Glimcher. Failure to detect crystalline brushite in embryonic chick and bovine bone by x-ray diffraction. *J. Ultrastructure Res.*, 86:93–99, 1984.

[31] E. D. Pellegrino and R. M. Blitz. Mineralization in the chick embryo. i. monohydrogen phosphate and carbonate relationships during maturation of the bone crystal complex. *Calcif. Tissue Res.*, 10:128–135, 1972.

[32] R. M. Blitz and E. D. Pellegrino. The nature of bone carbonate. *Clin. Orthop.*, 129:279–292, 1977.

[33] C. Rey and M. J. Glimcher. Short range organization of the Ca-P mineral phase in bone and enamel; changes with age and maturation. In H. Slavkin and P. Price, editors, *The Chemistry and Biology of Mineralized Tissues: Proceedings of the Fourth International Conference on the Chemistry and Biology of Mineralized Tissues Held in Coronado, California on February 5-9, 1992*, pages 153–162, Amsterdam, 1992. Elsevier Science Publishers B.V.

[34] W. P. Aue, A. H. Roufosse, M. J. Glimcher, and R. G. Griffin. Solid-state phosphorus-31 nuclear magnetic resonance studies of synthetic solid phases of calcium phosphate: potential models of bone mineral. *Biochemistry*, 23:6110–6114, 1984.

[35] A. H. Roufosse, W. P. Aue, J. E. Roberts, M. J. Glimcher, and R. G. Griffin. Investigation of the mineral phases of bone by solid-state phosphorus-31 magic angle sample spinning nuclear magnetic resonance. *Biochemistry*, 23:6115–6126, 1984.

[36] H. C. Anderson. *The biochemistry and physiology of bone*, chapter Matrix vesicles of cartilage and bone. Academic Press, New York, 2nd ed. edition, 1976.

[37] H. C. Anderson. Mineralization by matrix vesicles. *Scann. Electr. Micr.*, 2:953–964, 1984.

[38] Stephen Schmitz, Srdjan Djukic, and Harry K. Genant. The current status of bone densitometry. *Appl. Radiol.*, 19:20, 1990.

[39] J. W. Nieves, F. Cosman, C. Mars, and Lindsay R. Comparative assessment of bone mineral density of the forearm using single photon and dual x-ray absorptiometry. *Calcif. Tissue Int.*, 51:352–355, 1992.

[40] K. Engelke, S. Grampp, C. C. Glueer, and M. Jergas. Significance of QCT bone mineral density and its standard deviation as parameters to evaluate osteoporosis. *J. Comput. Assist. Tomogr.*, 19:111, 1995.

[41] B. H. Mitlak, D. Schoenfeld, and R. M. Neer. Accuracy, precision, and utility of spine and whole-skeleton mineral measurements by DXA in rats. *J. Bone Min. Res.*, 9:119–125, 1994.

[42] R. N. Pierson, J. Wang, J. C. Thornton, and D. P. Kotler. Bone mineral and body fat measurements by two absorptiometry systems: Comparisons with neutron activation analysis. *Calc. Tissue Int.*, 56:93, 1995.

[43] K. Aakesson, M. D. Grynpas, R. G. V. Hancock, and R. Odselius. Energy-dispersive x-ray microanalysis of the bone mineral content in human trabecular bone: A comparison with ICPES and neutron activation analysis. *Calc. Tissue Int.*, 55:236, 1994.

[44] O. Louis, P. Van Den Winkel, P. Covens, A. Schoutens, and M. Osteaux. Mineral content of vertebral trabecular bone: Accuracy of dual energy quantitative computed tomography evaluated against neutron activation analysis and flame atomic absorption spectrometry. *Bone*, 15:35–40, 1994.

[45] M. Moris, A. Peretz, R. Tjeka, N. Negaban, M. Wouters, and P. Bergmann. Quantitative ultrasound bone measurements: Normal values and comparison

with bone mineral density by dual x-ray absorptiometry. *Calcif. Tissue Int.*, 57:6, 1995.

[46] J. L. Cunningham, J. N. Fordham, T. A. Hewitt, and C. A. Speed. Ultrasound velocity and attenuation at different skeletal sites compared with bone mineral density measured using dual energy x-ray absorptiometry. *Br. J. Radiol.*, 69:25, 1996.

[47] Yaotang Wu, Jerome L. Ackerman, David A. Chesler, Jinxi Wang, and Melvin J. Glimcher. Quantitative measurement of 3D bone mineral density by solid state ^{31}P MRI. In *Proceedings of the Third Scientific Meeting of the Society of Magnetic Resonance, Nice, August 19–25*, 1995.

[48] M. A. Sabin, G. M. Blake, S. M. MacLaughlin-Black, and I. Fogelman. The accuracy of volumetric bone density measurements in dual x-ray absorptiometry. *Calcif. Tissue Int.*, 56:210–214, 1995.

[49] O. L. Svendensen, C. Hassager, V. Skodt, and C. Christiansen. Impact of soft tissue on in vivo accuracy of bone mineral measurements in the spine, hip, and forearm: a human cadaver study. *J. Bone Miner. Res.*, 10:868–873, 1995.

[50] Yaotang Wu, Melvin J. Glimcher, Christian Rey, and Jerome L. Ackerman. A unique protonated phosphate group in bone mineral not present in synthetic calcium phosphates. *J. Mol. Biol.*, 244:423–435, 1994.

[51] Susan J. Kohler, J. David Jr. Ellett, and Melvin P. Klein. ^{31}P NMR chemical shielding tensors of α-$Ca_2P_2O_7$. *J. Chem. Phys.*, 64:4451–4458, 1976.

[52] W. P. Rothwell, J. S. Waugh, and J. P. Yesinowski. High-resolution variable-temperature ^{31}P NMR of solid calcium phosphates. *J. Am. Chem. Soc.*, 102:2637–2643, 1980.

[53] J. Herzfeld, A. Roufosse, R. A. Haberkorn, R. G. Griffin, and M. J. Glimcher. Magic angle sample spinning in inhomogeneously broadened biological systems. *Phil. Trans. R. Soc. Lond.*, B 289:459–469, 1980.

[54] J. P. Yesinowski. High resolution NMR spectroscopy of solids and surface adsorbed species in colloidal suspension: ^{31}P NMR spectra of hydroxyapatite and diphosphonates. *J. Am. Chem. Soc.*, 103:6266–6267, 1981.

[55] Robin K. Harris, Peter Jackson, Philip J. Wilkes, and Peter S. Belton. Line narrowing in phosphorus-31 spectra of solids using a combination of high-power decoupling, cross-polarization, magic-angle spinning, and ^{31}P multiple-pulse operation. *J. Magn. Reson.*, 73:178–183, 1987.

[56] Charles Eric Brown, Joseph H. Battocletti, Srinivasan Ravi, James R. Allaway, Jeannine Moore, and Peter Sigmann. In vivo ^{31}P nuclear magnetic resonance spectroscopy of bone mineral for evaluation of osteoporosis. *Clin. Chem.*, 34:1431–1438, 1988.

[57] J. E. Roberts, L. C. Bonar, R. G. Griffin, and M. J. Glimcher. Characterization of very young mineral phases of bone by solid state ^{31}phosphorus magic angle sample spinning nuclear magnetic resonance and x-ray diffraction. *Calcif. Tissue Int.*, 50:42–48, 1992.

[58] J. L. Ackerman, L. Garrido, J. R. Moore, B. Pfleiderer, and Y. Wu. Fluid and solid state MRI of biological and nonbiological ceramics. In B. Blumich and W. Kuhn, editors, *Magnetic Resonance Microscopy: Methods and Application in Material Science, Agriculture and Biomedicine.* VCH Publishers, Weinheim, Germany, 1992.

[59] X. Marchandise, P. Belgrand, and A. P. Legrand. Solid state ^{31}P NMR spectroscopy of bone and bone substitutes. *Magn. Reson. Med.*, 28:1–8, 1992.

[60] J. P. Yesinowski and M. J. Mobley. ^{19}F MAS-NMR of fluoridated hydroxyapatite surfaces. *J. Am. Chem. Soc.*, 105:6191–6193, 1983.

[61] James P. Yesinowski and Helmut Eckert. Hydrogen environments in calcium phosphates: ^{1}H MAS NMR at high spinning speeds. *J. Am. Chem. Soc.*, 109:6274–6282, 1987.

[62] K. A. Smith and D. P. Barum. Application of fluorine-19 CRAMPS to the analysis of calcium fluoride/fluoroapatite mixtures. *J. Magn. Reson.*, 84:85–94, 1989.

[63] A. T. Kreinbrink, C. D. Sazavsky, J. W. Pyrz, D. G. A. Nelson, and R. S. Honkonen. Fast-magic-angle spinning ^{19}F NMR of inorganic fluorides and fluoridated apatitic surfaces. *J. Magn. Reson.*, 88:267–276, 1990.

[64] Liam B. Moran, Jeffery K. Berkowitz, and James P. Yesinowski. ^{19}F and ^{31}P magic-angle spinning nuclear magnetic resonance of antimony(III)-doped fluorapatite phosphors: Dopant sites and spin diffusion. *Phys. Rev. B*, 45:5347–5360, 1991.

[65] R. F. Code, R. L. Armstrong, R. S. Hallsworth, C. Lemaire, and P. T. Cheng. Concentration dependence of fluorine impurity spin-lattice relaxation rate in bone mineral. *Phys. Med. Biol.*, 37:211–221, 1992.

[66] G. Cho and J. P. Yesinowski. Multiple-quantum NMR dynamics in the quasi-one-dimensional distribution of protons in hydroxyapatite. *Chem. Phys. Lett.*, 205:1–5, 1993.

[67] Rodolfo A. Santos, Robert A. Wind, and Charles E. Bronnimann. ^{1}H CRAMPS and ^{1}H–^{31}P HetCor experiments on bone, bone mineral, and model calcium phosphate phases. *J. Magn. Reson. B*, 105:183–187, 1994.

[68] Yaotang Wu. *Solid state NMR study of bone mineral.* PhD thesis, Massachusetts Institute of Technology, 1992.

[69] M. Melchior. 22nd Annual Experimental NMR Conference, Asilomar, CA, Poster B-29, 1981.

[70] N Zumbulyadis. $^{1}H/^{29}Si$ cross-polarization dynamics in amorphous hydrogenated silicon. *J. Chem. Phys.*, 86:1162–1166, 1987.

[71] D. G. Cory and W. M. Ritchey. Inversion recovery cross-polarization NMR in solid semicrystalline polymers. *Macromol.*, 22:1611–1615, 1989.

[72] K. I. Dawson, I. E. Farnan, B. R. Constantz, and S. W. Young. Solid-state phosphorus-31 nuclear magnetic resonance differentiation of bone mineral and synthetic apatite used to fill bone defects. *Invest. Radiol.*, 26:946–950, 1991.

[73] J. L. Miquel, L. Facchini, A. P. Legrand, X. Marchandise, P. Lecouffe, M. Chanavaz, M. Donazzan, C. Rey, and J. Lemaitre. Characterization and conversion study into natural living bone of calcium phosphate bioceramics by solid state NMR spectroscopy. *Clin. Mater.*, 5:115–125, 1990.

[74] Charles Eric Brown, James R. Allaway, Kathy L. Brown, and Joseph H. Battocletti. Noninvasive evaluation of mineral content of bone without use of ionizing radiation. *Clin. Chem.*, 33:227–236, 1987.

[75] Charles Eric Brown, Ravi Srinivasan, Peter Sigmann, Joel B. Myklebust, and Joseph H. Battocletti. Comparison of the compression strength of human vertebral bodies with the mass and density of apatite: a study by ^{31}P NMR spectrscopy. *Clin. Chem.*, 34:2114–2117, 1988.

[76] Joseph H. Battocletti, Thomas J. Myers, Thomas A. Knox, Charles E. Brown, and Husain Kamal. Design of a low-field NMR spectrometer to measure bone mineral. *J. Clin. Eng.*, 15:479–487, 1990.

[77] M. Dolecki, D. Sashin, T. J. Mosher, J. H. Herndon, and M. B. Smith. A phosphorus NMR spectroscopy technique for measuring bone density. in vitro and in vivo studies. In *Abstracts. Ninth Annual Meeting, Society of Magnetic Resononance in Medicine, New York*, Berkeley, CA, 1990. The Society of Magnetic Resonance in Medicine.

[78] J. L. Ackerman, D. P. Raleigh, and M. J. Glimcher. Phosphorus-31 magnetic resonance imaging of hydroxyapatite: A model for bone imaging. *Magn. Reson. Med.*, 25:1–11, 1992.

[79] J. R. Moore, L. Garrido, and J. L. Ackerman. Solid state phosphorus-31 magnetic resonance imaging of bone mineral. *Magn. Reson. Med.*, 33:293–299, 1995.

[80] S. R. Hartmann and E. L. Hahn. Nuclear double resonance in the rotating frame. *Phys. Rev.*, 128:2042–2053, 1962.

[81] A. Pines, G. Gibby, and J. S. Waugh. Proton-enhanced nuclear induction spectroscopy. a method for high resolution NMR of dilute spins in solids. *J. Chem. Phys.*, 56:1776–1777, 1972.

[82] A. Pines, M. G. Gibby, and J. S. Waugh. Proton-enhanced NMR of dilute spins in solids. *J. Chem. Phys.*, 59:569–590, 1973.

[83] C. P. Slichter and William C. Holton. Adiabatic demagnetization in a rotating reference frame. *Phys. Rev.*, 122:1701–1708, 1961.

[84] A. G. Redfield. Nuclear magnetic resonance saturation and rotary saturation in solids. *Phys. Rev.*, 98:1787–1809, 1955.

[85] A. G. Anderson and S. R. Hartmann. Nuclear magnetic resonance in the demagnetized state. *Phys. Rev.*, 128:2023–2041, 1962.

[86] J. Jeener, H. Eisendrath, and R. Van Steewinkel. Thermodynamics of spin systems in solids. *Phys. Rev.*, 133:A478–A490, 1964.

[87] Hiroshi Hatanaka and Tsuneo Hashi. Irreversibility of adiabatic demagnetization in the rotating frame in double and single quantum NMR in solids. *J. Phys. Soc. Jpn.*, 64:1346–1355, 1995.

[88] J. Jeener and P. Broekaert. Nuclear magnetic resonance in solids: Thermodynamic effects of a pair of rf pulses. *Phys. Rev.*, 157:232–240, 1967.

[89] Fred M. Lurie and Charles P. Slichter. Spin temperature in nuclear double resonance. *Phys. Rev.*, 133:A1108–A1122, 1964.

[90] D. A. McArthur, E. L. Hahn, and R. E. Walstedt. Rotating-frame nuclear-double-resonance dynamics: Dipolar fluctuation spectrum in CaF_2. *Phys. Rev.*, 188:609–638, 1969.

[91] J. Jeener, R. Du Bois, and P. Broekaert. Zeeman and dipolar spin temperatures during a strong rf irradiation. *Phys. Rev.*, 139:A1959–A1961, 1965.

[92] R. L. Strombotne and E. L. Hahn. Longitudinal nuclear spin-spin relaxation. *Phys. Rev.*, 133:A1616–A1629, 1964.

[93] A. Abragam. *Principles of Nuclear Magnetism.* Clarendon Press, Oxford, 1961.

[94] N. Bloembergen and P. P. Sorokin. Nuclear magnetic resonance in the cesium halides. *Phys. Rev.*, 110:865–875, 1958.

[95] Dieter Wolf. *Spin-Temperature and Nuclear-Spin Relaxation in Matter: Basic Principles and Applications.* Clarendon Press, Oxford, 1979.

[96] M. Mehring. *High Resolution NMR Spectroscopy in Solids*, volume 11 of *NMR - Basic Principles and Progress.* Springer-Verlag, Berlin, 2nd edition, 1983.

[97] Jean Philippot. Spin-spin relaxation and spin temperatures. *Phys. Rev.*, 133:A471–A477, 1964.

[98] D. E. Demco, J. Tegenfeldt, and J. S. Waugh. Dynamics of cross relaxation in nuclear magnetic double resonance. *Phys. Rev. B*, 11:4133–4151, 1975.

[99] L. Müller, A. Kumar, T. Baumann, and R. R. Ernst. Transient oscillations in NMR cross-polarization experiments in solids. *Phys. Rev. Lett.*, 32:1402–1406, 1974.

[100] R. K. Hester, J. L. Ackerman, V. R. Cross, and J. S. Waugh. Resolved dipolar coupling spectra of dilute nuclear spins in solids. *Phys. Rev. Letters*, 34:993–995, 1975.

[101] W. Silberszyc, G. Marx, and J. S. Waugh. Dipolar couplings in calcium formate. *Acta Phys. Satyr.*, 11:1122–1133, 1970.

[102] X. Wu, S. Zhang, and X. Wu. Selective polarization inversion in solid state high-resolution CP MAS NMR. *J. Magn. Reson.*, 77:343–347, 1988.

[103] N Zumbulyadis. Selective carbon excitation and the detection of spatial heterogeneity in cross-polarization magic-angle-spinning NMR. *J. Magn. Reson.*, 53:486–494, 1983.

[104] V. R. Cross, R. K. Hester, and J. S. Waugh. Single coil probe with transmission-line tuning for nuclear magnetic double resonance. *Rev. Sci. Instrum.*, 47:1486–1488, 1976.

[105] M. E. Stoll, A. J. Vega, and R. W. Vaughan. Simple single-coil double resonance NMR probe for solid state studies. *Rev. Sci. Instrum.*, 48:800–803, 1977.

[106] S. Kan, M. Fan, and J. Courtieu. A single-coil triple resonance probe for NMR experiments. *Rev. Sci. Instrum.*, 51:887–890, 1980.

[107] F. David Doty, Ruth R. Inners, and Paul D. Ellis. A multinuclear double-tuned probe for applications with solids or liquids utilizing lumped tuning elements. *J. Magn. Reson.*, 43:399–416, 1981.

[108] Yi Jin Jiang, Ronald J. Pugmire, and David M. Grant. An efficient double-tuned $^{13}C/^{1}H$ probe circuit for CP/MAS NMR and its importance in linewidths. *J. Magn. Reson.*, 71:485–494, 1987.

[109] Anne Leroy-Willig, Jacques Bittoun, Siew Kan, and Patrick Gonord. A simplified double-tuned ^{31}P–^{1}H circuit for NMR *in vivo* spectroscopic experiments. *Rev. Sci. Instrum.*, 61:799–801, 1990.

[110] Elhadi Najim and Jean-Philippe Grivet. A double-tuned probe for metabolic NMR studies. *Magn. Reson. Med.*, 23:367–371, 1992.

[111] P. Van Hecke, C. Decanniere, and F. Vanstapel. Double-tuned resonator designs for NMR spectroscopy. *J. Magn. Reson.*, 84:170–176, 1989.